Pathology and Osteological Observations of Early Pliocene Rhinoceros, Teleoceras aepysoma (Perissodactyla, Rhinocerotidae) from Gray Fossil Site, Tennessee.

Thesis · April 2024

CITATIONS
0

READS
13

1 author:

Thomas Scaife
East Tennessee State University
3 PUBLICATIONS **2** CITATIONS

SEE PROFILE

Pathology and Osteological Observations of Early Pliocene Rhinoceros, *Teleoceras aepysoma* (Perissodactyla, Rhinocerotidae) from Gray Fossil Site, Tennessee.

A thesis

presented to

the faculty of the Department of Geosciences

East Tennessee State University

In partial fulfillment

of the requirements for the degree

Master of Science in Geosciences

---

by

Thomas W. Scaife

May 2024

Steven C. Wallace, Chair

Blaine Schubert

Josh Samuels

Keywords: pathology, *Teleoceras*, trauma, osteopathology, synovitis, rheumatoid arthritis, rhinoceros, Tennessee

ABSTRACT

Pathology and Osteological Observations of Early Pliocene Rhinoceros, *Teleoceras aepysoma* (Perissodactyla, Rhinocerotidae) from Gray Fossil Site, Tennessee.

by

Thomas W. Scaife

Rhinoceroses were an important part of North America's Paleogene and Neogene ecosystems, with *Teleoceras aepysoma* being one of the last representatives of this family. Specimens of *T. aepysoma* from the Gray Fossil Site (GFS) possess distinct/peculiar pathologies: including a pair of fused ribs and ankylosed phalanges. A qualitative description of the pathologies in the GFS *T. aepysoma*, including new material, was conducted to accurately identify pathologies and make interpretations about the life history of the GFS rhinos. Analysis suggests that rheumatoid arthritis is common in the lower limb bones of GFS rhinos. Additionally, the rib and toe pathologies are more severe than anticipated, with the ribs showing multiple stages of healing indicating repeated trauma, likely being the first direct evidence of agonistic behavior in *Teleoceras*. This study provides a glimpse of what pathological conditions rhinocerotids may have been vulnerable to through time, as well as a baseline for future studies.

ACKNOWLEDGEMENTS

Thanks to my committee chair, Steven C. Wallace, and committee members Josh Samuels and Blaine Schubert. Thanks to Chris Widga (former committee member) for assistance with micro-CT and 3D scanning. Thanks to Kurt Volle, Buffalo Zoo Veterinarian, for consultation due to his experience with pathology in captive animals. Thanks to George Corner for providing access to the UNSM collection and Morill Hall exhibition during my time in Nebraska. Thanks to Aunt Mary and Uncle David for hosting me while I conducted research in Nebraska. Thanks to the members of the GFS collections staff for assistance and providing a welcoming workspace in collections. Thanks to the volunteers who have put in countless hours collecting and prepping material at GFS. And thanks to my friends for advice, comradery, and support; and my family for loving and supporting me.

TABLE OF CONTENTS

LIST OF FIGURES

CHAPTER 1. INTRODUCTION

Pathology, the study of the effects of disease and injuries on organisms—as well as identification of their causes (Moodie 1923; Cook 2015; Waldron 2020), can be immensely informative, giving insights into an organism's environmental stresses, life history, and behavior (Kerly and Bass 1967; Rothschild and Tanke 1991; Garutt 1997; Hanna 2002; Rothschild and Martin 2006; Diedrich 2008; Griffin et al. 2016; Sazelová et al. 2020; Holmes et al. 2021; Diedrich 2023; Shpansky et al. 2023). In most medical applications, pathologies refer to only maladies caused by disease, but many in the field of paleontology studying pathology (referred to as paleopathology) also use the term to refer to traumatic injuries, such as fractures, punctures, etc. (Moodie 1923; Kerly and Bass 1967; Rothschild and Tanke 1991; Garutt 1997; Hanna 2002; Rothschild and Martin 2006; Cook 2015; Stilson et al. 2016; Sazelová et al. 2020; Waldron 2020).

Though specimens bearing pathologies are recognized as valuable in the modern paleontological paradigm, prior to the 20th century, such specimens were frequently overlooked in favor of those in better condition for descriptions, leading to a lag in understanding of how diseases affected prehistoric organisms (Moodie 1923; Cook 2015; Waldron 2020). Complicating paleopathology is the insular nature of medical terminology (in that medical terminology is dense and rarely taught outside of medical education), lack of certainty regarding diagnoses, and difficulty of implementing differential diagnosis (e.g. Kerley and Bass 1967; Bartosiewicz 2008; Stevanovic et al. 2015; Buikstra et al. 2017; Lawler 2017; K. Volle pers. comm. 2023). Regarding terminology and diagnoses in the field of paleopathology, consistency on these fronts has been an issue troubling the discipline, and there have been continued efforts to standardize terminology and diagnoses since the late 90s (Lovell 1997; Rothschild 2002;

Wilczak and Jones 2011; and Buikstra et al. 2017). Identifying the cause of pathologies in fossils can be further complicated by the lack of soft tissue evidence often used in diagnoses (Arnett et al. 1988; Feger et al. 2023), and the fact that bone can only react in a limited number of ways to multiple pathogenic factors (Moodie 1923; Bartosiewicz 2008; Waldron 2020). Modern technologies such as computed tomography (CT) and micro-CT have opened a new, non-destructive, avenue of analysis by allowing direct observation of the changes to internal bone structures, which are often diagnostic of pathology (Cook 2015; Sazelová et al. 2020).

Regarding pathology as applied to modern rhinos, most papers are written with a heavy focus on foot pathologies in captive specimens involved in conservation programs (e.g. Galateanu et al. 2013; Regnault et al. 2013; Von Houwald 2016; Panagiotopoulou et al. 2019). Silberman and Fulton (1979) provide a brief overview of disease and medical issues in captive rhinos, including some osteopathology (e.g., actinomycosis, arthritis). Other modern studies have explored the use of CT-scanning in diagnosis in rhino and other animals (e.g. Regnault et al. 2013; Hullot and Antoine 2022). The aforementioned focus on foot pathologies in recent publications is partially because rhinos (and other graviportal megafauna such as elephants) are vulnerable to infection/disease propagating throughout the foot (Regnault et al. 2013; 2017), as these animals possess a ‘glove’ of tissue around the bones of the feet to help bind the bones together; with little-to-no compartmentalization to prevent the circulation of foreign bodies (Luikart and Stover 2005). Such ‘gloved’ foot tissue allows for what would otherwise be only minor damage limited to the hoof or foot pad to propagate throughout the foot and/or worsen into a more prominent injury (Luikart and Stover 2005).

Galateanu et al. (2013) pioneered using CT-scanning to search for osteopathology in modern rhinos diagnosed with chronic foot disease, scanning 8 limbs from 3 cadavers (2

Ceratotherium, 1 *Rhinoceros*). Contrary to previous understanding, which posited that pathology was limited to the soft tissue of the foot, Galateanu et al. (2013) identified instances in the bones associated with chronic foot disease. Furthermore, osteopathology in the feet of *Ceratotherium* had not been diagnosed prior to Galateanu et al. (2013). Regnault et al. (2013) examined a larger sample of rhino cadavers and osteological specimens consisting of all 5 modern species: *Diceros bicornis, Ceratotherium simum, Rhinoceros unicornis, R. sondaicus,* and *Dicerorhinus sumatrensis* Regnault et al. (2013) documented and categorized pathologies using a mix of CT-scanning (cadavers) and visual examination (osteological specimens). These methods identified pathologies not previously recorded in rhinos (e.g. enthesophyte formation, pathologic remodeling), though such pathologies have been previously identified in elephants (Fowler and Mikota, 2006). Though aspects such as easy access and detailed record keeping make captive specimens a popular choice for research (e.g. Haynes 1983; Willey and Snyder 1989; Marean and Spencer 1991; Pickering and Wallis 1997; Njau and Blumenschine 2005; D'Amore and Blumenschine 2009; Drumheller 2012; Schachner et al. 2013; Drumheller and Brochu 2014, Radeke-Auer 2023), it is well documented that they can differ wildly to their wild counterparts (Drumheller et al. 2016). This includes differences in morphology (e.g. Hard et al. 2000; McPhee 2004b; Zuccarelli 2004; O'Regan and Kitchener 2005; Guay and Iwaniuk 2008; Drumheller et al. 2016), behaviour (e.g. Fleming et al. 1996; Geiser and Ferguson 2001; McPhee 2004a), and frequency and type of pathologies (Fitch and Fagan 1982; Munson et al. 2005; Drumheller et al. 2016).

While publications on modern rhinos have a narrow scope, the study of fossil rhino pathology is broader in scope. Several rhino paleopathology studies have been written on rhinocerotids and relatives, including Pleistocene Eurasian taxa (e.g. Garutt 1997; Diedrich 2008;

Böhmer and Rössner 2018; Stefaniak et al. 2023), North American taxa (e.g. Stecher 1962; Rothschild 2016; Stilson et al. 2016), Oligocene rhinocerotoids (e.g. Schellhorn 2021), and on arthropathy (joint pathology) trends in North American perissodactyls (e.g. Rothschild et al. 2001). Concerning the findings of the North American overview studies (e.g. Rothschild et al. 2001; Stilson et al. 2016), Rothchild et al. (2001) surveyed North American perissodactyls, with *Teleoceras* being one of the 11 rhinocerotids included, for spondyloarthropathy, or erosive arthritis. High frequencies of spondyloarthropathy were found in brontotheres and chalicotheres, and at increasing frequency through time in rhinocerotids and equids (Rothschild et al. 2001). An investigation into whether patterns of pathology through time exist within Rhinocerotidae found older taxa, which had yet to evolve large size, scored lower, and that larger, more derived taxa scored higher (Stilson et al. 2016). The authors concluded that the increased occurrence of pathology, particularly osteoarthritis in the distal limb bones, was likely associated with the increase of mass (Stilson et al. 2016). However, Rothschild et al. (2001) argued against size correlation, citing the distinct lack of increasing spondyloarthropathy rates in primates, which underwent a similar size increase. Such comparison is questionable given the differences between cursorial to medioportal perissodactyls (Stilson et al. 2016; Panagiotopoulou et al. 2019), and arboreal to scansorial primates. As a means of rationalizing the trend of increasing spondyloarthropathy presence in perissodactyls, Rothschild et al. (2001) suggested that spondyloarthropathy might instead provide some short-term selective benefit in rhinos and horses. Despite the aforementioned dissent, increasing size, while maintaining cursoriality, seems to be the most accepted explanation for the trend of increasing occurrence of pathologies in rhinos (Stilson et al. 2016; Panagiotopoulou et al. 2019). However, the increased occurrence of osteopathology in more recent extinct taxa described in the above studies could be a result of

the ‘pull of the recent’, where more and better-quality remains are found of younger taxa than older taxa (Sahney and Benton 2017; Pimiento and Benton 2020; Womack et al. 2020).

Regarding traumatic pathology, Garutt (1997, Table 1) noted that injuries in large extant herbivores are localized to areas open to being struck during intraspecific combat. For example, traumatic damage is typically localized to the crania and forelimbs in elephantids, the metapodials in equids, and the crania in derived two-horned rhinos (e.g. *Coelodonta antiquitatis*, *Diceros bicornis*, and *Ceratotherium simum*) (Garutt 1997). Studies of modern feral horse samples (Grogan and McDonnell 2005; Knubben et al. 2008) and observations of fossil *Equus* material (Van Kolfschoten et al. 2015) note damage to the ribs caused by kicks during fights between individuals. *Rhinoceros unicornis*, unlike *Diceros bicornis* or *Ceratotherium simum*, does not use its horn as its primary weapon when engaged in agonistic behavior, but instead uses its well-developed, blade-like lower incisors (Glover 1956; Garutt 1997; Mihlbachler 2001, 2003, 2007; Hazarika and Zaikia 2010). Instead, *R. unicornis* uses its horn in a supporting role, pulling the opponent’s skin taut, then gouging the opponent with the lower incisors (Glover 1956). Note, the lower incisors are henceforth referred to as tusks. Garutt (1997) further describes the usage of tusks in agonistic combat by *R. unicornis* as an “archaic behavior”, characteristic of more basal rhinos that had yet to develop the iconic horns seen in taxa such as *Coelodonta antiquitatis*, *Diceros bicornis*, and *Ceratotherium simum*. Additionally, *R. unicornis* and basal rhinocerotids (e.g., *Trigonias*, *Subhyracodon*) possess dermal armor on regions of the face vulnerable to being lacerated by tusks (Hieronymus 2009), thereby limiting damage to these areas. Given the similarity in cranial anatomy of *Teleoceras* and *R. unicornis* (notably the enlarged, blade-like lower incisors), such dents and osteomas on the crania as described in

Coelodonta antiquitatis (Garutt 1997) are unlikely to be prominent in *Teleoceras*. Instead, evidence of flank injuries is more likely to be encountered in *Teleoceras*.

Teleoceras has several described species from across North America (Harrison and Manning 1983; MacFadden 1998; Milhbachler 2003; Prothero 2005; Stilson et al. 2016; Short 2019). Among these species, *Teleoceras aepysoma* is distinctive for having less exaggerated proportions, including longer legs and less rotund torsos (Short 2013; Short et al. 2019). As of time of writing, *T. aepysoma* is only known from Gray Fossil Site (GFS) (Short 2013; Short et al. 2019). There are suggestions that the *Teleoceras* of the Palmetto Fauna, in Florida, represent another sample of *T. aepysoma* but this requires further study (Short 2013). The GFS rhinos are also notable for being found in a highland forest environment (Shunk et al. 2006; Ochoa et al. 2012). This environment is atypical for *Teleoceras* (Short 2013), which is more typically found in lowland savannahs and floodplains (Osborn 1898; MacFadden 1998; Mead 2000; Prothero 1998, 2005; Stilson et al. 2016; Wang and Secord 2020). Though several studies have noted the presence of pathology in *Teleoceras* during the 130 years since the description of the genus by Hatcher in 1894 (e.g. Webb 1969; Mead 2000; Tucker et al. 2014, Short et al. 2019), there has only been a single previous in-depth study of paleopathology on *Teleoceras* (Mead 1999), which identified enamel hypoplasia in several *Teleoceras* (*T. medicornutum*, *T. major*, and *T. fossiger*) specimens from Nebraska. The identification of enamel hypoplasia occurrence on the dp4, a tooth still in development prior to birth, suggests the mother was under physiological stress during gestation (Mead 1999). The lack of focus on pathologies specific to *Teleoceras* can be attributed to most research either only analyzing *Teleoceras* down to genus level as a representative sample amongst other genera (e.g., Rothschild et al. 2001), or only analyzing for a single type of pathology (e.g., Mead 1999; Stilson et al. 2016). No previous study has followed

multiple lines of evidence to investigate the presence of pathology in an entire species of *Teleoceras*.

Rhinos were once an abundant group in North America during the Paleogene and Neogene (Prothero et al. 1989; Prothero 1998, 2005; Tedford et al. 2004). The extinction of Rhinocerotidae in North America, specifically *Aphelops* and *Teleoceras*, has been used to help define the end of the Hemphillian North America Land Mammal Age (NALMA) (Prothero et al. 1989; Prothero 1998, 2005; Tedford et al. 2004). Though rare records of rhinos have been reported from the Blancan (Madden and Dalquest 1990; Farlowe et al. 2001; Gustafson 2012), these consist of isolated and fragmentary material that has the potential to have been reworked (Prothero 2005; Short et al. 2019). GFS has most recently been assigned to around the latest-Hemphillian/earliest-Blancan NALMA via biochronology (Samuels et al. 2018; Samuels and Schap 2021), which makes the GFS *T. aepysoma* potentially one of the youngest occurrences of rhinos in North America (Short 2013; Short et al. 2019).

Teleoceras aepysoma was formally described and identified as a new species in Short et al. (2019). The morphology and a few pathological features were noted Short et al. (2019). Five potential pathologies were noted in Short's thesis and subsequent publication (Short 2013; Short et al. 2019). The purpose of this thesis will be a comprehensive review of all pathologies of the GFS *T. aepysoma*, including material initially examined in Short et al. (2019), GFS material accessioned from the University of Tennessee Knoxville (UTK), and new material recovered since 2019. I will also be reviewing taphonomic, individual, and ontogenetic features to differentiate from pathology. The age of the GFS *T. aepysoma*, the presence of new material, and the general lack of similar studies on the genus warrant a detailed description of pathology in the GFS *T. aepysoma*.

CHAPTER 2. MATERIALS AND METHODS

Unless otherwise stated, all descriptions are based on specimens from the Gray Fossil Site (GFS). Fossils are part of the ETMNH (East Tennessee State University Museum of Natural History) collection, which is housed at the [ETSU] Gray Fossil Site & Museum. Of note, some of the material described here was recovered during initial work done at GFS by the University of Tennessee Knoxville (UTK). This material was prepared and stored in the McClung Museum of Natural History and Culture until recently (transferred to ETMNH 12/15/2021). This study only covers material that has been prepared prior to August 17, 2022 (see Table 1 in Appendix, as well as *included specimens* in Chapter 3). The minimum number of individuals (MNI) from GFS is 8 as of that date. Interpretation of relative bone condition is made via references to literature and comparisons between specimens. Reference to modern rhino material (ETMNH-Z 7216, *Rhinoceros unicornis*), another *Teleoceras* species (*T. major*, Ashfall Fossil Beds (AFB)), and material described in Stilson et al. (2016) is also made here. Of note, many AFB specimens were left in jackets or in taphonomic pose limiting observation, as the joint surfaces in particular were obscured.

An important aspect to note about GFS specimens is that most are recovered as crushed and are reconstructed during lab preparation whenever possible. Briefly, ETMNH specimens have been largely reconstructed using Butvar-98 (a reversible, clear plastic adhesive which is easily differentiated from bone) using methods developed by Haugrud and Compton (2008). ETMNH 609, being the first fully reconstructed *T. aepysoma* specimen, is the exception and was instead reconstructed using a two-part epoxy as the primary adhesive. This is primarily due to ETMNH 609 being reconstructed to allow detailed molds to be made without damaging ETMNH

609. Notably for this study, the epoxy was colored to resemble the fossils from Gray, making the distinction between original bone and epoxy unclear in places.

Lawler (2017) was referenced for methodology and differential diagnosis sources. Brooks (1996), Lovell (1997), Wilczak and Jones (2011), and Buikstra et al. (2017) were referenced for consistent and useful terminology for pathology. For consistency, basic anatomical terminology follows that of Short et al. (2013), unless stated otherwise. The term spondyloarthropathy is used herein to acknowledge that arthritis itself is not a specific disease, but a condition caused by a variety of environmental, genetic, and behavioral factors (Rothschild et al. 2001; Stilson et al. 2016). Additionally, arthropathy is used to reference defects to joints (Stilson et al. 2016). Differences between in-life osteolysis and taphonomic features are poorly explored in the literature. Therefore, in this study taphonomic features are identified as fractures that retain angular borders, or have been worn smooth, with visible delineation of cortical and cancellous bone (Fig. 1). Osteolysis is identified as porous lesions without a clearly delineated boundary between cortical and cancellous bone (Fig. 1).

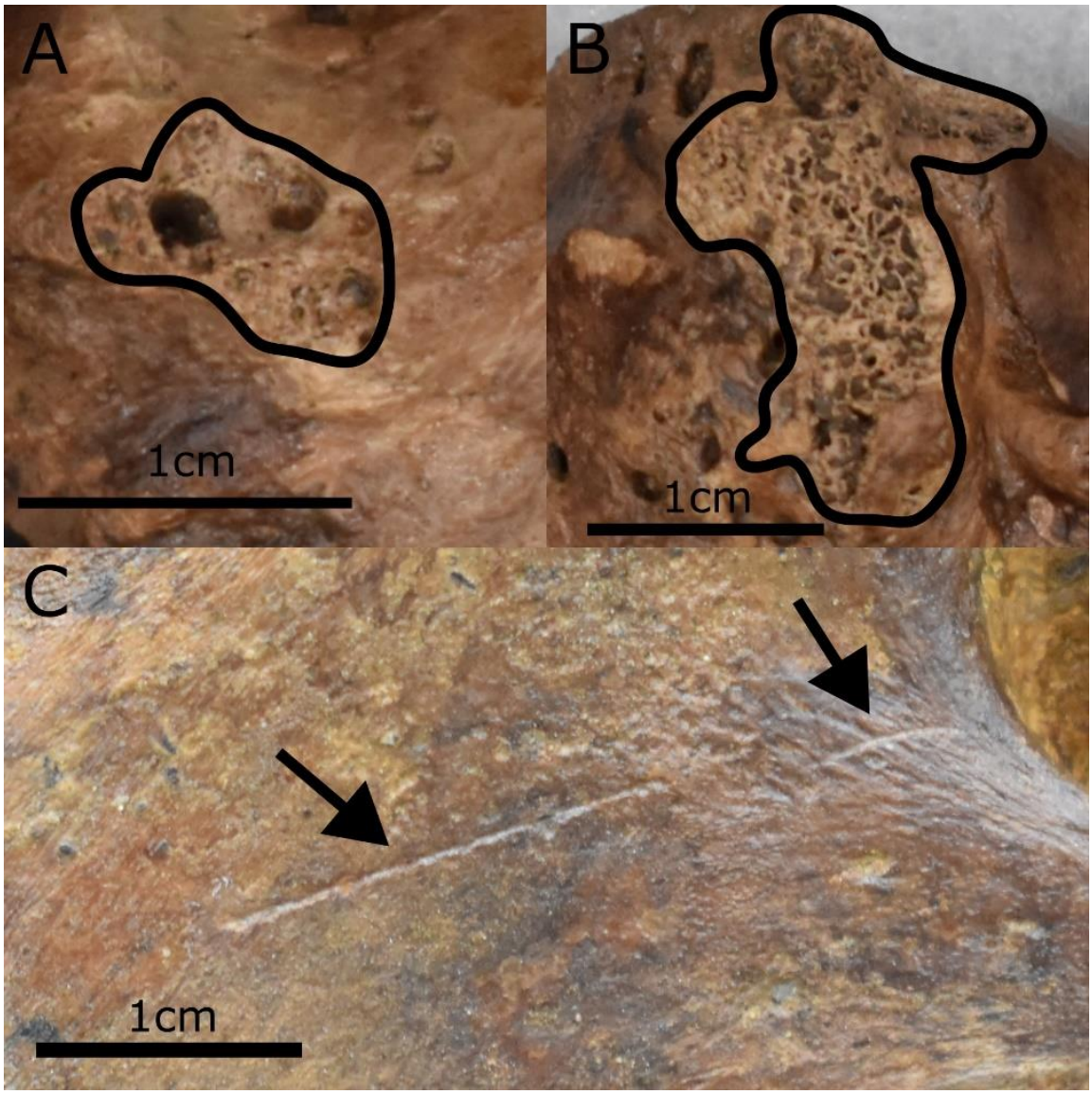

Fig. 1 Examples from GFS of osteolysis (**A**), and trabecular bone revealed by taphonomic weathering (**B**), both outlined in black; and trowel marks (**C**), indicated by arrows. Note on **A** the consistently round pore shape in conjunction with variable pore size, while on **B** the size of trabeculae is uniform and angular in shape. The impact of a trowel on a bone creates a long, straight indentation, as seen on **C**

Measurements of pathological features reported here were taken with a World Precision Instruments Digital Caliper 150mm/6in. CTs were generated using the Skyscan model 1273 X-

ray computed tomography scanner at ETSU to investigate changes in trabecular bone structure. High resolution scans were analyzed in ORS Dragonfly. 3D surface scanning was performed using an Artec Space Spider 3D scanner, and processed in Artec Studio version 15, to highlight fine surface detail, eliminate biases from color/gloss, and make figures.

Marginal lipping is described using the categories and scoring system of Buikstra and Ubelake (1994) as described by the Osteoware Software Manual Volume II: Pathology Module (Wilczak and Jones 2011). In an effort to be more concise, the modified labeled categories from Osteoware (Wilczak and Jones 2011) described here will be abbreviated as follows:

1. **Barely discernable (CAT1):** identification requiring visual aids, usually less than 1 mm in height.
2. **Rounded ridge lipping (CAT2):** lipping presents round profile in cross section, is easily palpated, and is easily observed without visual aids. It is usually greater than 1 mm in height.
3. **Sharp ridge sometimes with curled spicules (CAT3):** lipping that is sharp in cross section and greater than 1 mm in height. Irregularity of the lipping sometimes includes bony spicules, both curled or uncurled.
4. **Initial and full joint fusion (CAT4):** initial joint fusion requires evidence for incipient ankylosis around or across joint space. Full joint fusion is defined by partial or full joint immobility.

Abbreviations – Terminology Modified from Short (2013)

AAF – Anterior articular facet

AH – articular head

ALP – anterolateral processes

AP – anconeal process

ARR – articular rugosity for radius

ASA – articular surface for astragalus

ASC – articular surface for cuneiform

ASCap – articular surface for capitulum

ASCb – articular surface for the cuboid

ASCb2 – second articular surface for the cuboid (on the navicular)

ASCL – articular surface for calcaneus

ASDP – articular surface for distal phalanx

ASEc – articular surface for the ectocuneiform

ASEn – articular surface for entocuneiform

ASL – articular articular surface for lunar

ASM – articular surface for magnum

ASMC2 – articular surface for metacarpal 2

ASMC3 – articular surface for metacarpal 3

ASMC4 – articular surface for metacarpal 4

ASMC5 – articular surface for metacarpal 5

ASMe – articular surface for mesocuneiform

ASMP – articular surface for the medial phalanx

ASMT2 – articular surface for metatarsal 2

ASMT3 – articular surface for metatarsal 3

ASMT4 – articular surface for metatarsal 4

ASN – articular surface for the navicular

ASP – articular surface for pisiform

ASPP – articular surface for proximal phalanx

ASR – articular surface for radius

ASS – articular surface for scaphoid

ASSD1-2 – articular surfaces for sesamoids (1 = lateral, 2 = medial)

AST – articular surface for the trapezoid

ASTm – articular surface for trapezium

ASTr – articular surface for trochlea

ASUL – articular surface for ulna

ASUn – articular surface for unciform

Cap – capitulum

CB – cranial border

Abbreviations – Terminology Modified from Short (2013) continued

CTb – calcaneal tuber

DR – dorsal ridge

DT – deltoid tuberosity

EcC – epicondylar crest

GT – greater tuberosity

Gr2 – second groove (humerus)

ImT – intermediate tubercle (humerus)

LP – lunar process

LAP – lateral articular process

M – upper molar

m – lower molar

MASC – medial articular surface for calcaneum

MC2 – metacarpal 2

MC3 – metacarpal 3

MC4 – metacarpal 4

MC5 – metacarpal 5

MEc – medial epicondyle

MT2 – metatarsal 2

MT3 – metatarsal 3

MT4 – metatarsal 4

NK – radial neck

OF – olecranon fossa

OP – olecranon process

P – upper premolar

p – lower premolar

PP – posterior-process (scaphoid)

PR – posterior ridge (metacarpal)

Tr – trochlea

UnP – unciform process

VB – vertebral border

Institutional Acronyms – Ashfall Fossil Beds – **AFB**, East Tennessee State University Museum of Natural History – **ETMNH**, East Tennessee State University Museum of Natural History Zoological collection – **ETMNH-Z**, East Tennessee State University – **ETSU**; Florida Museum of Natural History – **FLMNH**, Gray Fossil Site – **GFS**, University of Nebraska State Museum – **UNSM**, University of Tennessee Knoxville – **UTK**

CHAPTER 3. DESCRIPTION

Crania

Included specimens: ETMNH 601, 609, 12175, 13914.

Two nearly complete crania of *Teleoceras aepysoma* (Short, 2013; Short et al., 2019) are available from the Gray Fossil Site. These being from the paratype, ETMNH 601, and the holotype, ETMNH 609. Short et al. (2019) determined the ages of ETMNH 601 and ETMNH 609 via dental wear, following age classes developed by Hitchins (1978) on *Diceros bicornis*. Short et al. (2019) determined that ETMNH 601 was a fully mature adult within age class XII-XIII, which corresponds to around 11-18 years of age in *Diceros bicornis* (Hitchins, 1978). ETMNH 609 was determined to be a younger adult by Short et al. (2019), within age class X-XI, corresponding to roughly 8-12 years of age in *Diceros bicornis* (Hitchins 1978). Both specimens were found lying on their right side, resulting in both accumulating taphonomic weathering on the exposed left side (Short 2013; Short et al. 2019). This weathering manifests as a lighter reddish-orange-brown, instead of the dark brown typical of fossils found at Gray Fossil Site (Fig. 2). Except for a few porous lesions around molar alveoli (described below), both complete crania show few overall antemortem defects. In addition to these specimens, a partial nasal (ETMNH 12175) and an isolated right maxilla fragment (ETMNH 13914) are present.

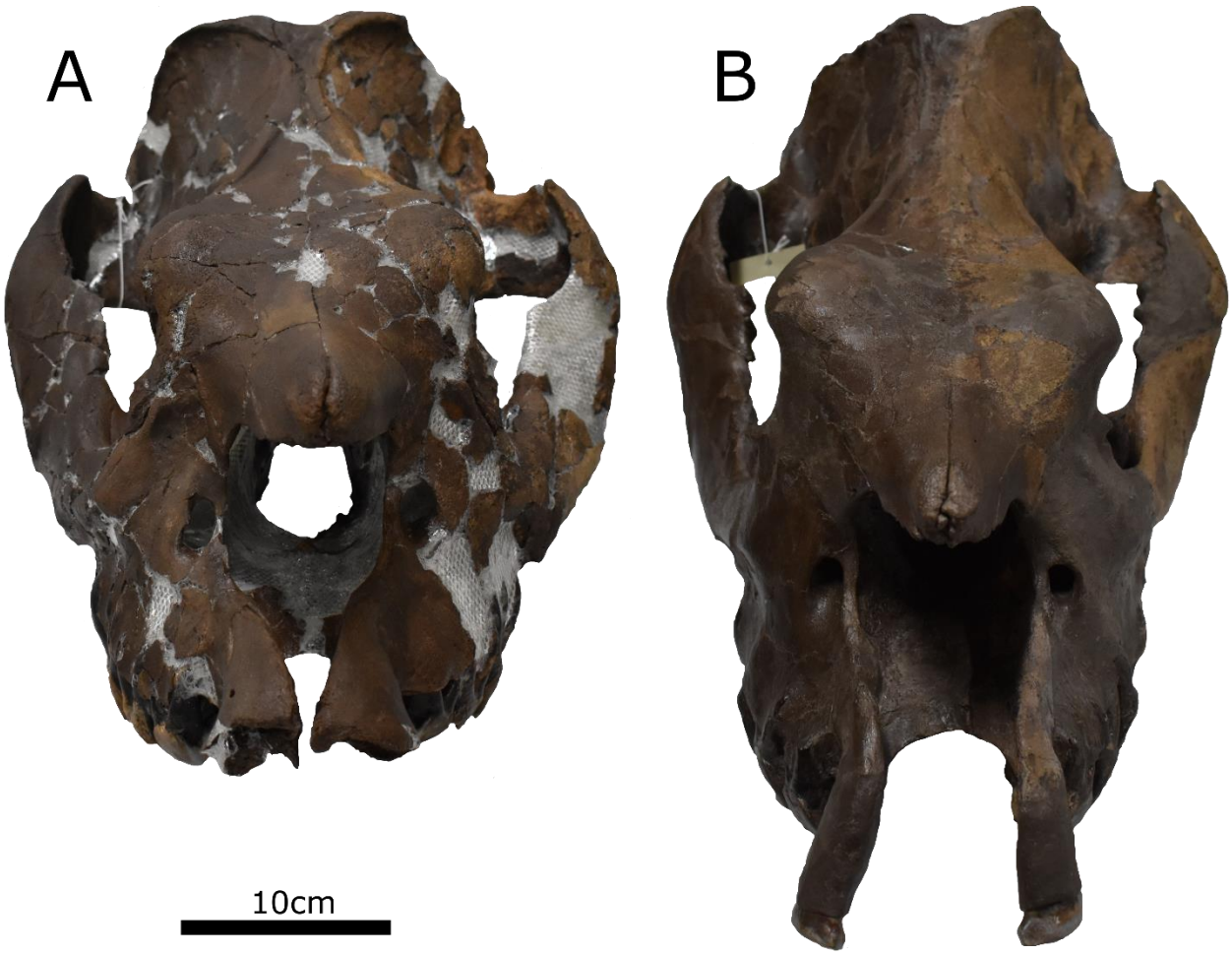

Fig. 2 Crania of ETMNH 601 (**A**) and ETMNH 609 (**B**) (both *Teleoceras aepysoma* from Gray Fossil Site, Washington C., Tennessee), with **A** in anterior view and **B** in antero-dorsal view. Note lighter coloring of both specimens' left surfaces, as well as differing reconstruction materials with **A** using Butvar-76 (a plastic adhesive) and **B** using Magic-Sculpt (a two-part epoxy). Also, the premaxillae on **B** were erroneously reconstructed based on simple vertical occlusion between the incisors

Mild rugose texturing is present on the nasals of ETMNH 601, ETMNH 609, and ETMNH 12175 (Fig. 3 and Fig. 4). ETMNH 12175 also preserves some unique features, with the left and right nasal bone being more completely fused than on either of the complete specimens, as noted in Short (2013). In addition, ETMNH 12175 preserves a distinct rostral

point absent from either ETMNH 601 or ETMNH 609 (Fig. 4). This rostral point has a concave surface on the left and convex surface on the right (Fig. 4).

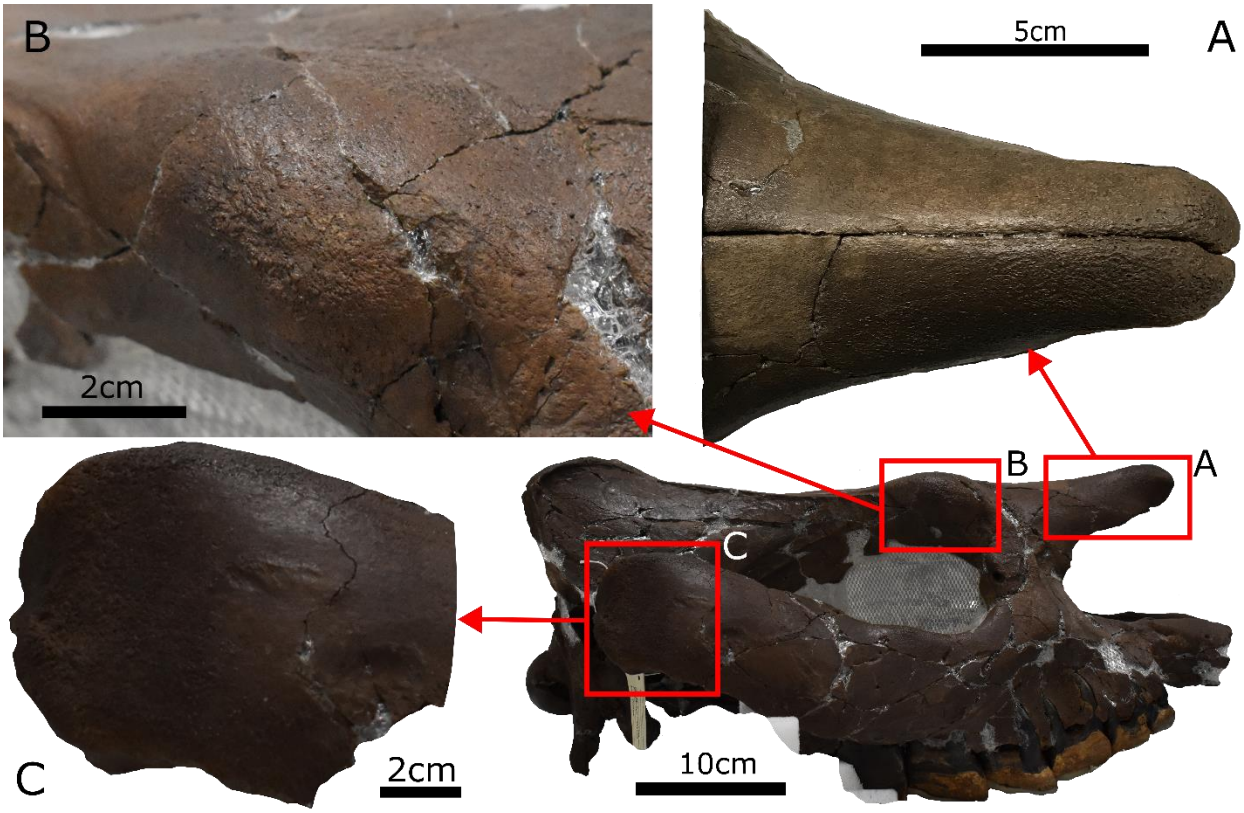

Fig. 3 Cranium of ETMNH 601 (*Teleoceras aepysoma* from Gray Fossil Site, Washington Co., Tennessee) in right lateral view. Insets (**A-C**) detailing regions with similar rugosities; **A**) nasal rugosity, **B**) dorsal orbital knob rugosity, and **C**) squamosal rugosity. Note that the distribution would be more consistent with areas of dermal armor, rather than horn attachments. Red squares on whole skull locate closeups (**A-C**).

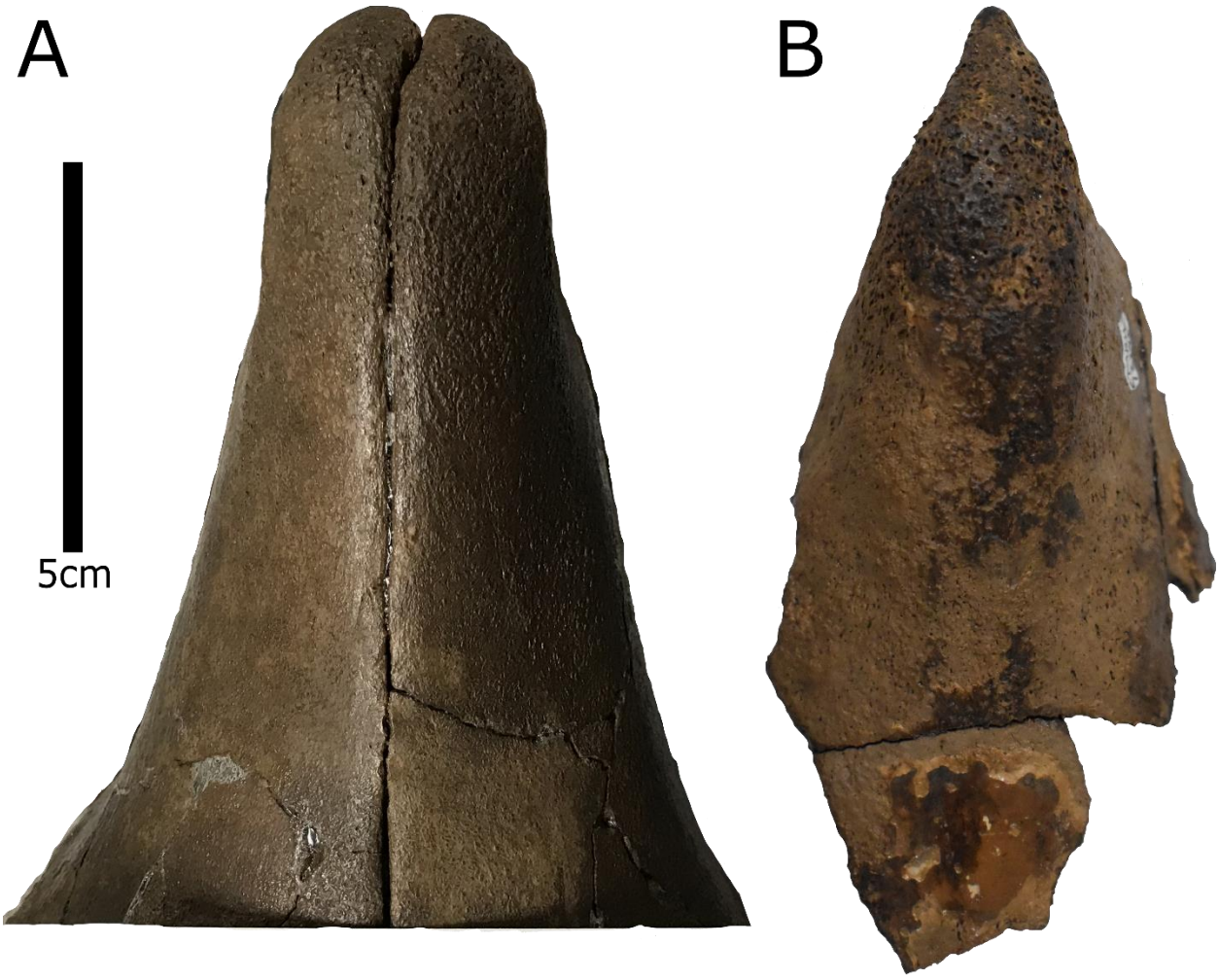

Fig. 4 Dorsal view of the nasals of ETMNH 601 and ETMNH 12175 (both *Teleoceras aepysoma* from Gray Fossil Site, Washington Co., Tennessee). Note that ETMNH 601 (**A**) has a rounded rostral end and remains unfused, while ETMNH 12175 (**B**) has pointed rostral end and is completely fused

On the parietals, neither specimen's temporal crests merge to form a sagittal crest, with the crests of ETMNH 601 being closer together than those of ETMNH 609. The separation of temporal crests observed in ETMNH 601 and ETMNH 609 is different than in *T. major* from AFB/UNSM, where the temporal crests meet to form a low sagittal crest. The separated temporal crests condition is consistent with *T. fossiger* and other late occurring *Teleoceras* species (S.

Tucker pers. comm. 2022). Between the temporal crests on both specimens is a small ridge extending posteriorly to the supraoccipital. The lambdoid crest on ETMNH 601 displays a broad lip/ledge, along the posterior margin, that is likely for muscle attachments. The lambdoid crests appear to be distinctly less developed on ETMNH 609, especially posterolaterally. Comparing the overall shape of two specimens' lambdoid crests, the apices on the crests of ETMNH 601 are low, wide, and likely were symmetrical in life, discounting the lateral breakage on the left crest. On ETMNH 609, the lambdoid crests are asymmetrical (Short et al. 2019), with the left side being longer and flaring less than the right side.

Premaxillae converge and meet anteriorly in ETMNH 601 (Fig. 3), as is the normal condition in *Teleoceras* (Fig. 34). Conversely in ETMNH 609, the premaxillae are not reconstructed as meeting proximally as in other *Teleoceras*, but as diverging distally (Fig. 3). The unique morphology of the premaxillae of ETMNH 609 is an artifact of reconstruction, as these bones were not preserved on ETMNH 609 and preparators erroneously based their reconstruction on the most likely occlusion of the upper incisors given the configuration of occluding wear surfaces of the lower incisors. The morphology should follow closer to that of ETMNH 601 (Fig. 3), even if the premaxillae of ETMNH 609 truly are wider spaced than those of ETMNH 601 (as suggested in Short et al. 2019).

Maxillae, lacrimals, and jugals appear largely free of irregularities on ETMNH 601, ETMNH 609, and ETMNH 13914. The right infraorbital foramen of ETMNH 601 has a small (~2 mm) pointed osteophyte halfway down its lateral rim, pointing medially.

Orbitals of ETMNH 601 and ETMNH 609 are not well-preserved, with those of ETMNH 601 being essentially absent. On ETMNH 609, the ventral interior of the right orbit has an irregular shape, likely due to taphonomic weathering or crushing.

As mentioned above, mild rugose texturing is visible on the lateral surface of the right squamosal of ETMNH 601 (Fig. 3); the left squamosal is significantly weathered, and so cannot be evaluated. Similar texturing is also present on the lateral surface of both squamosals of ETMNH 609, though the full extent is unclear due to these bones being partially reconstructed.

Occipitals of ETMNH 601 and ETMNH 609 have notable reconstruction, leaving little material for description.

Ventral portions of the paraoccipital processes are missing on ETMNH 609, likely due to postmortem breakage.

Other than some postmortem breakage, both pterygoid processes of ETMNH 601 appear to be in good condition. Conversely on ETMNH 609 the pterygoids are entirely missing, with the left pterygoid having been reconstructed.

Mandible

Included specimens: ETMNH 601, 609, 17351, 17352, 17353, 19280, 21659.

More mandibular material is represented at GFS than cranial, though ETMNH 601 and ETMNH 609 remain the two specimens in best condition. Mandibles of ETMNH 601 and ETMNH 609 were crushed, like the crania, but large pieces and minimal flaking afforded more complete assembly. As with the crania, weathering is observed on the left dentaries of both ETMNH 601 and ETMNH 609, whereas the right dentaries are nearly unaffected. In addition to the two complete specimens are ETMNH 19280 and ETMNH 21659, partial specimens that preserve portions of the dentary with ETMNH 21659 in particular preserving a notable inflamed region on the lingual side, and fragmentary material (ETMNH 17351, ETMNH 17352, and ETMNH 17353).

On the dentary, ETMNH 601 preserves porous lesions between the roots of the left p3, anterior and posterior to the caudal root of the left m1, and surrounding the roots of the right m1. These periodontal lesions average around 10 mm in diameter with 0.5-3 mm pores. The lesions have approximately 1.2 pores per mm^2 extending about 12 mm down the mandible. Smaller pores are circular, while the larger pores are more oblong and irregular. Corresponding areas on ETMNH 609 involve a greater degree weathering and reconstruction than on ETMNH 601, therefore it is not possible to determine the presence or absence of porous lesions. The pores' shape is uniformly round on ETMNH 609, unlike on ETMNH 601. ETMNH 21659 has an inflamed, rugose, roughly egg-shaped exostosis on the lingual side of the left dentary below the m3 (Fig. 5; ~107 mm anterior-posterior (ant-post), ~55 mm dorsal-ventral (dors-vent), and ~18 mm medial-lateral (med-lat)), and a porous lesion between p4 and m1, about 20 mm dorsoventral and 40 mm anteroposterior. Pores are about twice as dense as on ETMNH 601 and 1.5 mm or less in size. Another porous lesion is found nestled between the roots of p3 on ETMNH 21659, extending about 10 mm down. Pores are less dense than between p4 and m1 but more uniform in size, at around ~1 mm in diameter.

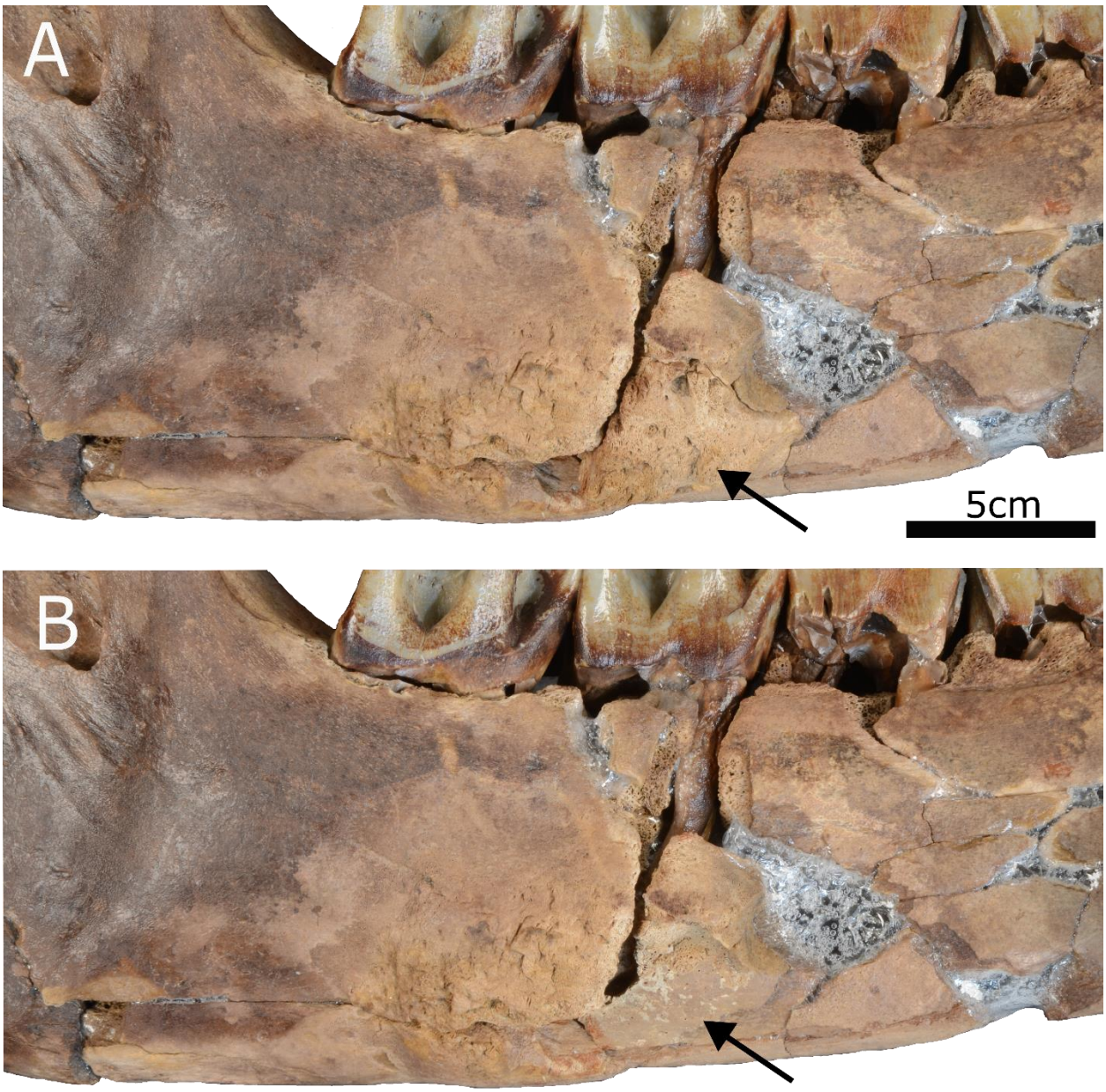

Fig. 5 Left mandible of ETMNH 21659 (*Teleoceras aepysoma* from Gray Fossil Site, Washington Co., Tennessee) in lingual view. Arrows highlight **A**) in-life condition of the pathology and **B**) the unaffected underlying bone

On ETMNH 601 the anterodorsal edge of the right coronoid process is relatively flat and broad, forming medial and lateral ridges. Evidence for this is also present on the left coronoid process, despite being heavily weathered. ETMNH 609 has a similar phenomenon displayed as

well, though only on the medial ridge of the right coronoid process, as the left was reconstructed. ETMNH 17353, representing an isolated coronoid process fragment, lacks the medial or lateral ridges present in ETMNH 601 and ETMNH 609.

ETMNH 601 has small medial postmortem fractures in both articular condyles and lateral postmortem breakage on the left articular condyle. Both of the articular condyles of ETMNH 601 have 3 anteroposterior grooves starting at the midpoint of the condyle and spaced variously 6-14 mm apart, laterally. Only one such groove is preserved laterally on the right condyle of ETMNH 609. On ETMNH 601, the left articular condyle is rotated anteriorly, so that it and the right condyle are nearly parallel on the transverse plane.

Angles of ETMNH 601 have rugose texturing consistent with the attachment of jaw musculature, with ETMNH 609's angles being markedly less rugose than those of ETMNH 601.

Though the mandible of ETMNH 33000 has yet to be prepared at time of writing, the tusks are available for description. The left tusk of ETMNH 33000 has narrow, shallow, curved marks (~14.5-18.9 mm across) on the exposed labial surface (the anterior surface of the tusk). Furthermore, these marks cross over each other at shallow angles.

Vertebrae

Cervical Vertebrae

Included specimens: ETMNH 601, 609.

Cervical vertebrae are only present for ETMNH 601 and ETMNH 609, with both preserving the atlas, axis, and cervical vertebrae 3-7 (Short, 2013; Short et al., 2019). Like the cranial elements described above, the left sides of the specimens show taphonomic weathering. Increased weathering on the left side is especially visible on the atlantes of both ETMNH 601 and ETMNH 609, and the axis of ETMNH 609. Remaining cervical vertebrae of ETMNH 601

and ETMNH 609 are in somewhat worse condition, missing parts of various processes with more severe damage to the left side. Taphonomic weathering has worn the articular surface of most of the cervical. Three of the cervical vertebrae of ETMNH 601 are fixed together by concretion, preventing observation of the zygopophyses.

Axes are in somewhat better condition than the atlases. The axis of ETMNH 601 is weathered at multiple points and has postmortem breakage on the anterior of the odontoid process, the lateral pre-zygopophyses, and the posterior of the transverse processes. The axis of ETMNH 609 has general taphonomic weathering across all surfaces, most notably on the left side. The dorsal process is shortened anteriorly compared to ETMNH 601. Both specimens' axes have asymmetrical dorsal rugosities, with the left being broader and more bulbous than the right on ETMNH 601, and the right taller and left broader on ETMNH 609.

Of the remaining cervical vertebrae (3-7), the last three (the 5th, 6th, and 7th) are concreted together in ETMNH 601 with only the 3rd and 4th cervical vertebrae being detached. The anterior surface of the centra have no defects, whereas the posterior surface of the centrum is in significantly worse condition on the last (7th) cervical of the concreted sequence on ETMNH 601. Transverse processes are missing, leaving the transverse foramina laterally open. 3rd cervical of ETMNH has a bone fold on the anterior portion of the left prezygapophysis (Fig. 6; ~11.57 mm ant-post). The right half of the posterior centrum has an uneven surface, rough edges, and some postmortem breakage (Fig. 7). In addition to this, the left and right halves of the posterior centrum have different coloration, with the left being a richer brown, the right a more grayish brown, with a dark red boundary between. The discoloration is attributable to taphonomic staining left over from concretion. Most of the missing material of the 3rd cervical is posterior right, including to the centrum (Fig. 7). The 4th cervical vertebra of ETMNH 601 has

bumps on the right of its anterior centrum, potentially corresponding to the posterior surface of the 3rd cervical vertebra (Fig. 7).

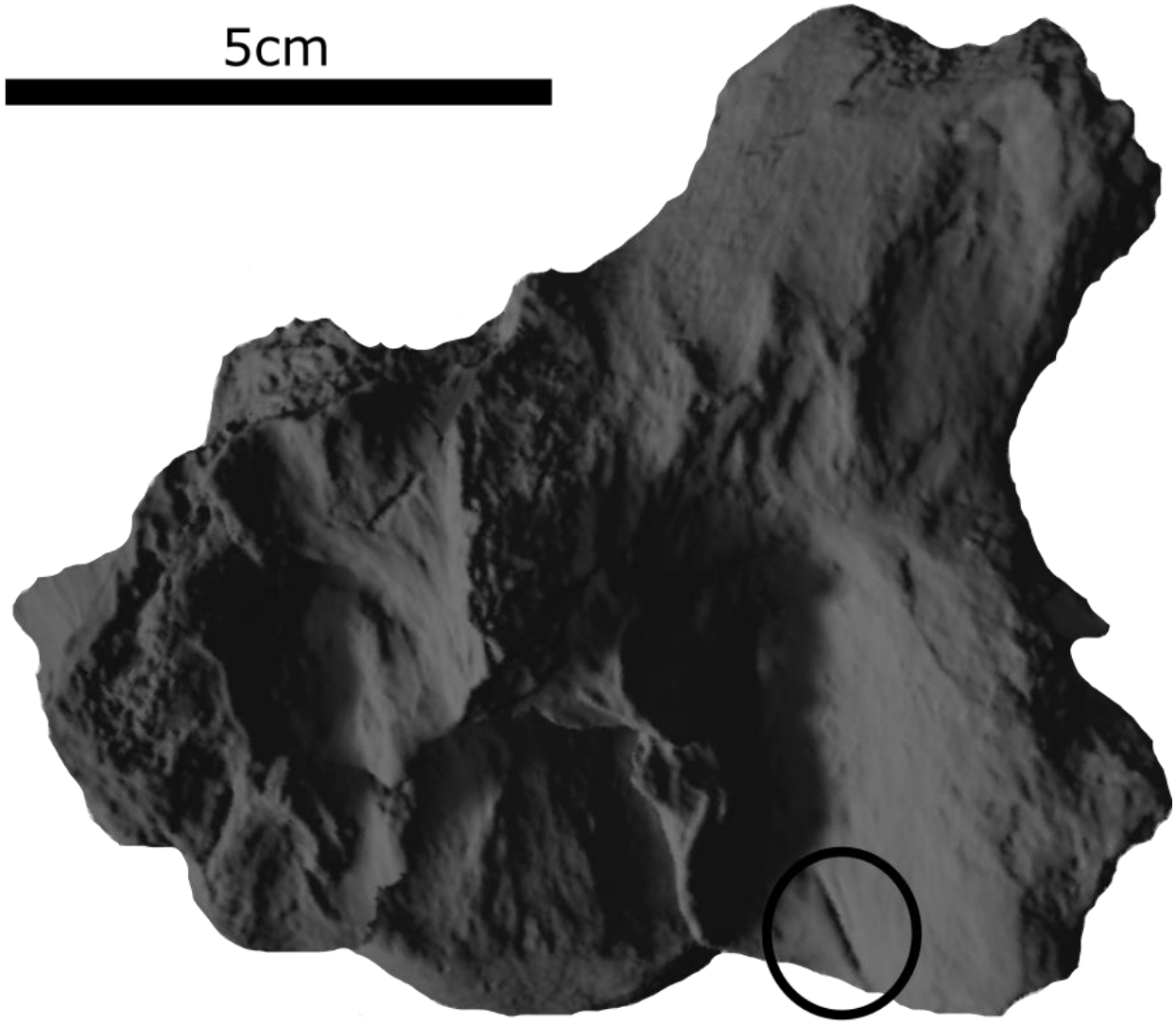

Fig. 6 Scan of partial 3rd cervical vertebra of ETMNH 601 (*Teleoceras aepysoma* from Gray Fossil Site, Washington Co., Tennessee) in dorsal view. Note the linear bone fold (circled) on the left prezygapophysis

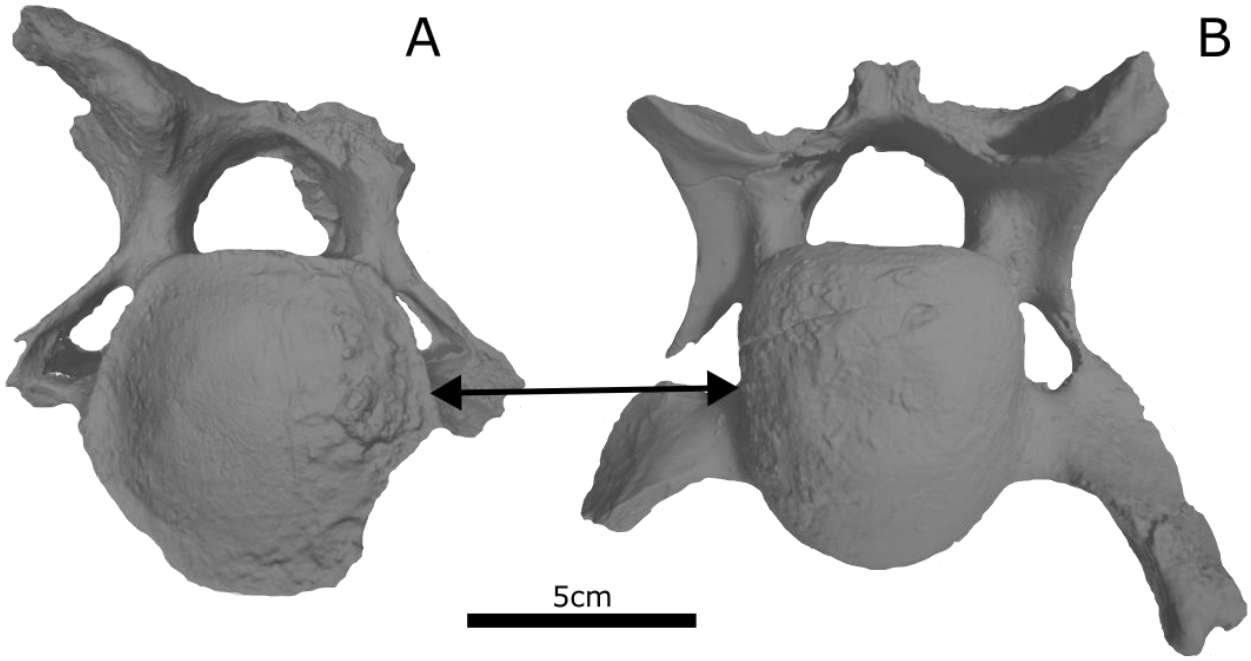

Fig. 7 Surface scans of cervical vertebrae from ETMNH 601 (*Teleoceras aepysoma* from Gray Fossil Site, Washington Co., Tennessee). **A**) 3rd cervical vertebra in posterior view with lesion/osteolysis on the right ventral portion of the centrum (lefts side of arrow). **B**) 4th cervical vertebra in anterior view with small bumps/tubercles on the corresponding left ventral portion of its centrum (right arrow). These texture changes on the centra are also associated with color differences

All the cervical vertebrae of ETMNH 609 are accessible. The anterior surface of the centra of all cervical vertebrae is in good condition. As with the concreted cervical sequence of ETMNH 601 described above, the posterior surface of the 3rd and 4th cervical vertebrae of ETMNH 609 are in worse condition than the anterior surface. Taphonomic effects to the 5th, 6th, and 7th cervical vertebrae of ETMNH 609 are limited to small fractures.

Thoracic Vertebrae

Included specimens: ETMNH 601, 609, 3752, 12175.

Thoracic vertebrae are primarily represented by ETMNH 609, as well as partial vertebrae from ETMNH 3752 and ETMNH 12175. As described in Short et al. (2019), only 10 of the thoracic vertebrae from ETMNH 601 are preserved; being mostly partial elements and associated fragments, or in concretion. Since that study, 4 thoracic vertebrae have been mostly reassembled, displaying significant taphonomic weathering. On ETMNH 609, the vertebrae are in relatively good condition, largely lacking the noticeable differential weathering present on other elements. Many are missing their posterior epiphyseal plates, either being concreted to the subsequent vertebra or missing entirely. ETMNH 3752 has a largely intact centrum and neural spine, with the broken neural arch having been reassembled. Centrum of ETMNH 12175 is intact, with the other portions having yet to be reassembled. No pathologic defects were identified amongst the thoracic vertebrae.

Lumbar Vertebrae

Included specimens: ETMNH 609.

Lumbar vertebrae are represented solely by ETMNH 609, which preserves all 3 in generally good condition (Short 2013; Short et al. 2019). The first lumbar vertebra's anterior epiphyseal plate is missing, and the second's left transverse process has been reconstructed. All three display taphonomic weathering on their distal left portions, leaving no conclusive evidence for pathology.

Sacrum

Included specimens: ETMNH 601, 609.

Only the sacrum of ETMNH 609 is preserved in good condition, though fragments from ETMNH 601 are present (Short 2013; Short et al. 2019). Sacrum of ETMNH 609 suffered from

prominent taphonomic weathering, as well as having notable reconstruction on the left side. Beyond weathering, the sacrum has no immediately identifiable defects.

Caudal Vertebrae

Included specimens: ETMNH 559, 573, 601, 609.

Caudal vertebrae are represented by two complete series in ETMNH 601 and ETMNH 609 and two isolated vertebrae from ETMNH 559 and ETMNH 573 (Short 2013; Short et al. 2019). All are in good condition, with broken elements reconstructed/reassembled. Two anomalous examples are caudal vertebrae 18-19 and 20-21 from ETMNH 609, which display epiphyseal fusion (Short 2013; Short et al. 2019). Both are smoothly fused with no reactive bone growth or exostoses. Vertebra 18-19 are misaligned, while 20-21 are straight. Additionally, evidence of a postmortem break on the posterior vertebra 19 and anterior of vertebra 20 suggests caudal vertebrae 18-21 were a single fused sequence in life.

Other Axial Elements

Sternebrae

Included specimens: ETMNH 609, 19280.

Sternebrae are preserved as ossified elements in ETMNH 609 and ETMNH 19280. Sternebrae of ETMNH 609 consist of three intact segments, decreasing in size posteriorly. In ETMNH 19280, only the partial manubrium is preserved, missing the anterior half of the element.

Ribs

Included specimens: ETMNH 601, 609, 3747, 3752, 3754, 4286, 6037, 6649, 6749, 7291, 7294, 8271, 10959, 12242, 14174, 14710, 14894, 17355, 17356, 19280, 20419, 20424, 21297, 21299, 21659, 27500, 27777, 28178, 33000.

Ribs have been preserved from numerous specimens, though the vast majority are broken segments (Short 2013; Short et al. 2019). Most of the complete ribs are associated with ETMNH 601 and ETMNH 609, though ETMNH 3754 has at least 5 partial ribs with numerous additional fragments. Most of the ribs are in good condition excluding taphonomic weathering and fracturing. ETMNH 601 possesses several antemortem healed injuries (Fig. 8 and 9), while ETMNH 609 is unafflicted. The lack of distinct pathologies on the ribs of ETMNH 609 could be the result of preservation bias. Although the majority of the ribs of ETMNH 609 have intact shafts which do not preserve pathologies, many of the ribs have had their proximal ends reconstructed. Therefore, the possibility of pathologies on the heads at one time, as seen on ETMNH 601 (Fig. 9), cannot be ruled out.

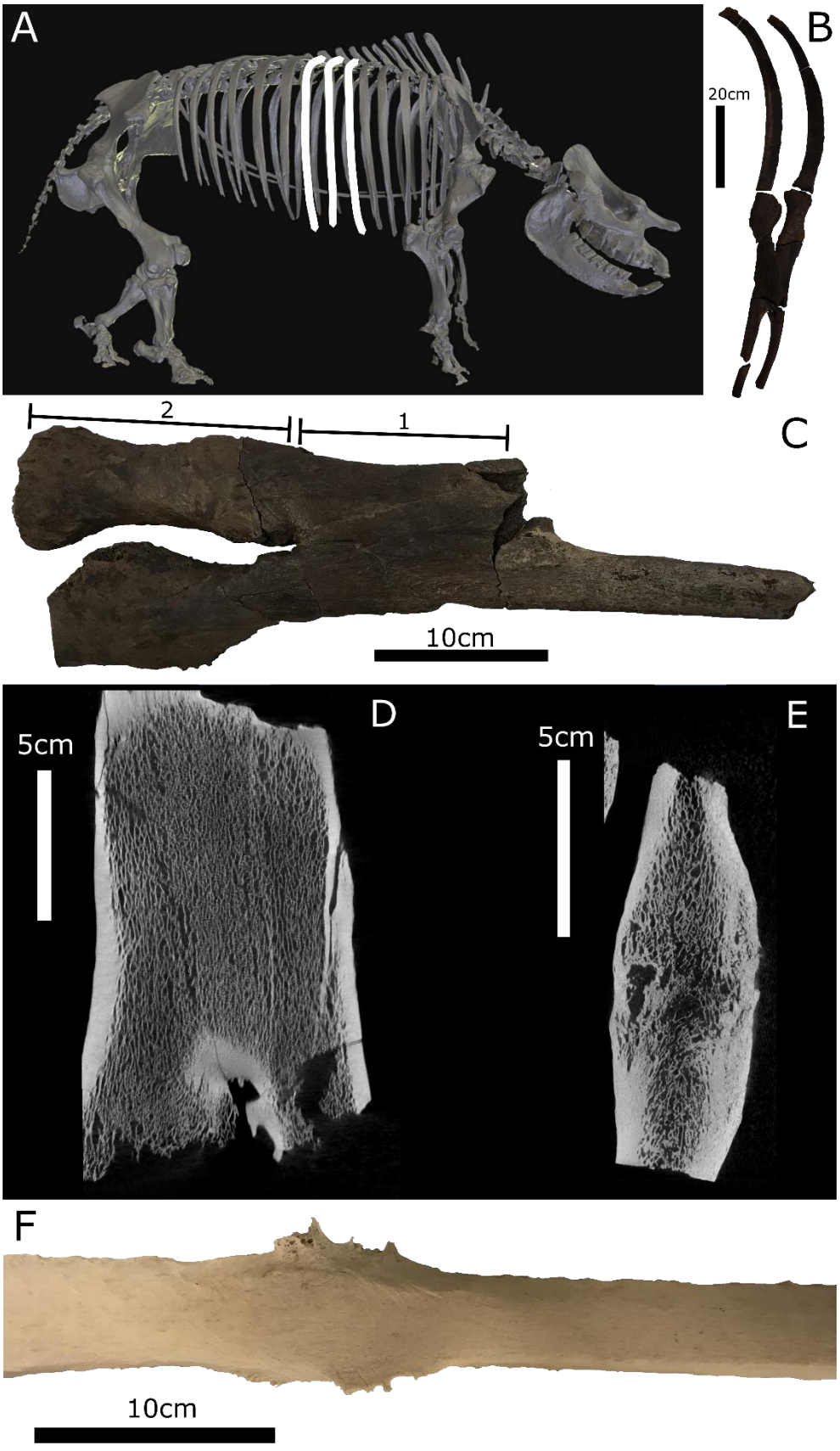
A
B
20cm
2
1
C
10cm
5cm
D
5cm
E
F
10cm

Fig. 8 **A**) Mount of ETMNH 609 (*Teleoceras aepysoma* from Gray Fossil Site, Washington Co., Tennessee) in right lateral view, with white denoting the approximate location of the fused right rib fragments of ETMNH 601. **B**) ETMNH 601 rib callus with associated fragments in medial view. **C**) Callus in medial view, positioned as in life showing external differences between the smooth older break (**1**) and the swollen, rugose newer breaks (**2**). **D**) micro-CT of **1** in medial view, and **E**) micro-CT of **2** in anterior view. Note the fully reorganized trabeculae in **D** compared to the less organized trabeculae of **E**. The different stages of healing between **D** and **E** indicate that ETMNH 601 broke its ribs on multiple occasions, suggesting a repeated behavior such as agonistic combat. **F**) ETMNH-Z 7216 (*Rhinoceros unicornis* from Buffalo Zoo) rib in medial view with a healed fracture sustained after falling on his side while mounting a female. Note the difference of severity between the fractures on ETMNH 601 and ETMNH-Z 7216 (which was similar in mass to and somewhat taller than ETMNH 601 in life)

The ribs of ETMNH 601 are broken, with several irregularities focused primarily in two adjacent ribs on the right side (ribs 9 and 10 or 10 and 11; L.G. Emmert pers. comm., 2023). A large, smooth plate of fused bone connects ribs 6 and 7 distally (Fig. 8). Fusion between the ribs extends ~150 mm proximodistally and is between ~88-97 mm anteroposterior. Proximal to the plate are 2-3 irregular swollen knobs (anterior: ~82 mm proximal-distal (prox-dist), ~76 mm ant-post, and ~45 mm med-lat; posterior: ~45 mm prox-dist (partial), ~75 mm ant-post, and ~36 mm med-lat). ETMNH 601 also has a proximal right rib fragment, which appears most similar to ribs 15-17 on ETMNH 609, with a posterior proximal articular surface that has been significantly widened with lipping and has an irregular surface with pits and bumps (Fig. 9).

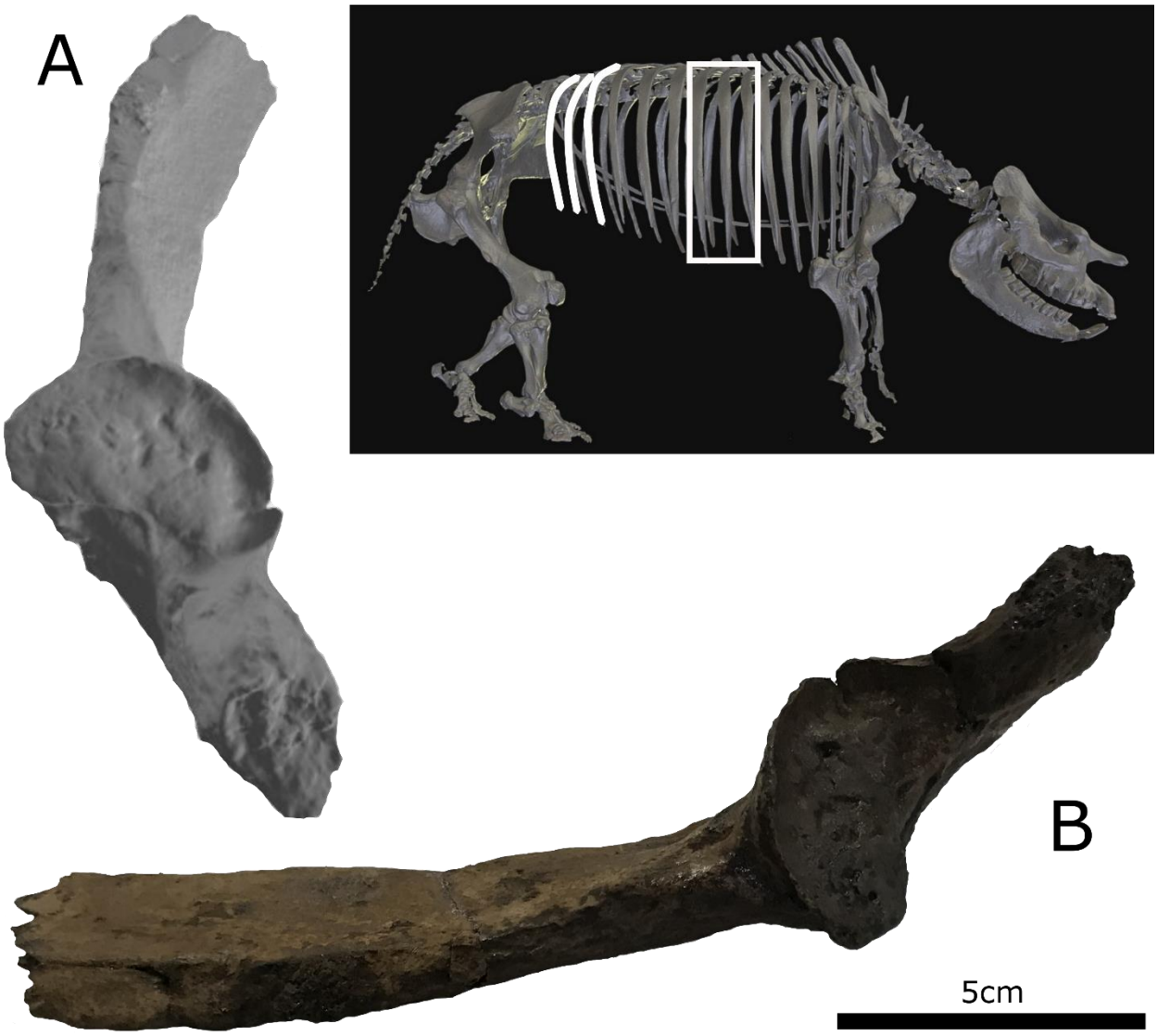

Fig. 9 Proximal right-side rib fragment from ETMNH 601 (*Teleoceras aepysoma* from Gray Fossil Site, Washington Co., Tennessee) with flared and pitted proximal articular facet. Inset showing approximate location of the proximal rib fragment (highlighted in white) relative to the callus (box). **A**) 3D scan in oblique proximomedial view highlighting surface features, and **B**) photo in medial view

Forelimbs

Scapula

Included specimens: ETMNH 601, 609, 29000.

Three specimens preserved scapulae, including both type specimens (ETMNH 601 and ETMNH 609) as well as ETMNH 29000. On ETMNH 601, the scapulae are mostly complete and have been reassembled as much as possible. Scapulae of ETMNH 609 are notably more intact, especially the right, allowing descriptions of the medial surfaces (Short 2013; Short et al. 2019), though the widespread reconstruction on ETMNH 609 may give false interpretations of surface texture in some areas. Both complete specimens display differential taphonomic weathering between their left and right scapulae, with the left side being the more afflicted of the two. ETMNH 29000 consists of a ventral scapula fragment (including the glenoid) with taphonomic breaks and weathering.

Proximal growth plates on ETMNH 601 appear to be intact on the CB and VB. More rugose texturing is present on the proximal end of the left scapula; likely representing muscle scarring. The distal articular surface of the right scapula has posterior lipping, though the equivalent area on left scapula is too weathered to identify the presence or absence of lipping.

On ETMNH 609, the growth plate is partial on the right scapula's CB and VB and missing entirely from the left scapula CB. Left and right scapula possess rugose texture on the proximal end, similar to the left scapula of ETMNH 601. The distal articular surface has some small posterior fractures attributed to postmortem breakage. Small fractures to the edges are more prominent on the right than the left scapula. Due to the more intact nature of ETMNH 609, analysis of the medial surfaces is possible. Medial surface has small fragments of concretion left behind from preparation, dotting its surface, along with some rugose texturing toward the proximal end, likely the result of taphonomic weathering.

Humerus

Included specimens: ETMNH 601, 609, 5057, 6648, 19280; UTK 1.01, 1.02, 1.03 (all from GFS and part of the ETMNH collection).

The humeri of ETMNH 601 and ETMNH 609 are the most complete, with only small fragments missing. Remaining material is incomplete, with ETMNH 5057 being a left subadult epiphyseal plate with no obvious defects; ETMNH 6648 being a partial right proximal end mostly reassembled, though only the AH is in good condition; and UTK 1.01, UTK 1.02, and UTK 1.03 being proximal epiphysis, proximal diaphysis, and distal epiphysis fragments, respectively. Former UTK specimens above are probably associated pieces of a single humerus and are likely referable to ETMNH 19280. ETMNH 601 and ETMNH 609 have suffered notable taphonomic breakage across the diaphysis, with ETMNH 609 having markedly more intact epiphyses (Short 2013; Short et al. 2019). On ETMNH 601, material for the epiphyses is present but have yet to be fully reassembled due to crushing deformation (discussed below).

Anterior humeral heads of ETMNH 601 have yet to be fully reassembled. The right humeral GT is in poorer condition due to crushing and concretion postmortem, preventing reassembly efforts without damaging the specimen. The anterior of the Gr2 and ImT of the left humerus has bone loss to their distal portion. This area also has a curved incision approximately 11 mm long, 2 mm wide, and 2 mm deep. The right humeri of both ETMNH 609 and ETMNH 6648 have incipient CAT2 posterior lipping on AH with a visible shelf (~3-4 mm for ETMNH 609 and ~2-3 mm for ETMNH 6648).

DT of the left humerus of ETMNH 601 is not fully intact. In ETMNH 609, the left humerus's diaphysis is rugose due to weathering. Conversely, this weathering has resulted in muscle scarring on the distal EcC becoming smoother than on the right humerus. Right EcC of

ETMNH 601 shows potential scarring in the form of semi-depressed rugose surface at the lateral/distal end (Fig. 10). The left humerus has similar scarring, to a lesser degree (Fig. 10). On ETMNH 609, MEc of both humeri are mildly rugose due to weathering from exposure.

Fig. 10 Posterior view of both humeri epicondylar crests (EcC) from ETMNH 601 (*Teleoceras aepysoma* from Gray Fossil Site, Washington Co., Tennessee). **A)** depression/scarring on right EcC in posterior view with an arrow pointing to it, and **B)** left EcC which lacks the aforementioned feature/with less prominent depression

On ETMNH 601, the capitulum of the left humerus has a mild lip with minimal shelf and contrasting bone loss including a ~4 mm cavity located laterally on the posterior Tr. In addition to these is a channel on the distal Tr, approximately 2 mm wide mediolateral, 15 mm long anteroposterior, and 1 mm deep. OF has a lip with a small shelf (~4 mm) on the posterior edge of the distal articular surface. Meanwhile, the presence or absence of pathology unable to be

determined on the Cap or Tr of the left humerus of ETMNH 609 due to postmortem breakage and reconstruction. Though numerous toolmarks from prep are visible on the Cap.

Ulna

Included specimens: ETMNH 502 (includes UTK 9.01), 601, 609, 8762; UTK 8.02 (all from GFS and part of the ETMNH collection).

Ulnae are represented by the two complete *T. aepysoma* (ETMNH 601 and ETMNH 609), a right ulna proximal end from ETMNH 502 (and distal end from the associated UTK 9.01), and a left ulna fragment, preserving part of ASR1, from ETMNH 8762 (Short 2013; Short et al. 2019). In addition to these specimens are left proximal and distal fragments, UTK 8.02 and UTK 9.01, the latter having been found to be the distal end of ETMNH 502. ETMNH 8762 will be excluded for the purposes of this study as it is too incomplete to assess. The OP of ETMNH 502 was broken proximally past the proximal articular surfaces, along with most of the distal diaphysis, though one fragment of the diaphysis has been reattached, while the distal end (UTK 9.01) has not. Both ETMNH 601 and ETMNH 609 have been entirely reassembled minus a few small fragments from ETMNH 601. Other differences between the two specimens are most probably age related, with ETMNH 601 having more developed rugosities and muscle scars than ETMNH 609. Other elements of ETMNH 601 and ETMNH 609 have similar differential taphonomic weathering between left and right elements, with the left elements consistently showing more weathering. Otherwise, the two specimens' ulnae look to have been in good health. ETMNH 502 (UTK 9.01) and UTK 8.02 have much paler, orange to white, coloration rather than the typical brown of most GFS fossils. This discoloration is potentially due to increased exposure to weathering, as evidenced by the smooth, rounded edges of postmortem

breaks on these specimens. ETMNH 502 (UTK 9.01) and UTK 8.02 are otherwise mostly unremarkable, though distal ETMNH 502 (UTK 9.01) shows some arthritic indicators (Fig. 11).

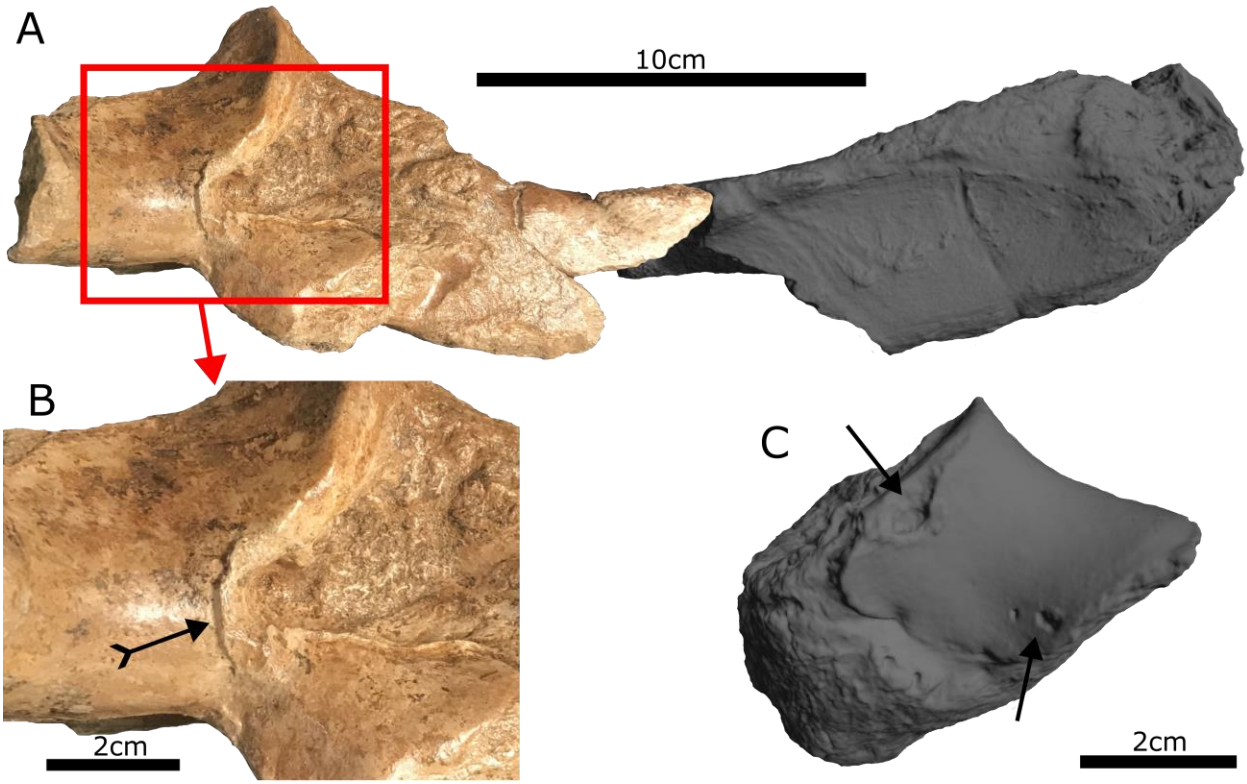

Fig. 11 **A**) associated right ulna proximal and distal ends of ETMNH 502 (proximal) and surface scan of UTK 9.01 (distal), both *Teleoceras aepysoma* from Gray Fossil Site, Washington Co., Tennessee, in anterior view. **B**) deformed trochlear notch with visible step, indicated by feathered arrow. **C**) distal view of UTK 9.01 with osteolysis on the articular surface for the cuneiform (ASC), denoted by arrows. Red square on proximal ulna locates closeup (**B**)

The AP of the right ulna distal end of ETMNH 502 has proximal postmortem breakage and weathering in addition to the loss of the proximal OP. Both the right and the left ulna APs of ETMNH 601 have lateral postmortem breakage. Right ulna of ETMNH 609 has marginal lipping with an associated shelf on the AP, while the left's proximal AP has evidence of small postmortem fractures and weathering. Distal portion of the trochlear notch (TN) of ETMNH 502

is deformed along the edge of the radial notch (RN), with a raised shelf of bone appearing to have been pressed proximally into the TN (Fig. 11; ~1.5 mm high, ~18.4 mm med-lat, and ~6.7-7.7 mm prox-dist/deep). The compression/wear feature (in addition to a pair of likely wear facets) on the TN/RN of ETMNH 502's right ulna appears to have been the result of in-life activity, though the surface has some small uneven postmortem fractures and weathering as well. LAP of ETMNH 502 has lateral taphonomic weathering, with a cavity exposing cancellous bone at the center of this weathering (~6.5 mm prox-dist, ~3.8 mm ant-post, and ~1.2 mm deep). Left ulna of ETMNH 609 has significant postmortem breakage and weathering to the lateral portion of the LAP, with the articular surface having been reduced/eroded laterally and posteriorly (Fig. 12). The LAP of UTK 8.02 also suffers notable postmortem breakage and weathering. The right ulnae of ETMNH 502, ETMNH 601, and ETMNH 609 have internal lipping on ASR1. ASR1 and distal MAP of ETMNH 601 and ETMNH 609 show probable CAT1 lipping around the radial notch. Both ulnae of ETMNH 601 have a notable tubercle structure on the anterior of the proximal ARR that is mirrored on radii (Fig. 13). These tubercle structures are not present on either ulnae of ETMNH 609. The ASC of the right ulna of ETMNH 601 has a sigmoidal posterior edge. On the medial side of the ASC, ETMNH 502 (UTK 9.01) has two erosive pits in the posterior articular surface, the most medial being 3 mm diameter and the most lateral 1 mm diameter, as well as round edge lipping, the extent of which is obscured by taphonomic weathering. There appears to be similar lipping on the lateral anterior ASC. Proximal ASR2 and the boundary with the ASC possess a mix of postmortem weathering and fracture, and potential arthritic bone loss (as supported by 'frothy' bone around the anterior end of the medial cavity). Short et al. (2019) notes that ETMNH 601 has an additional distal articular surface for the pisiform. The distal pisiform articular surface is absent in ETMNH 502 (UTK 9.01).

Fig. 12 Proximal ulnae of ETMNH 601 and ETMNH 609 (both *Teleoceras aepysoma* from Gray Fossil Site, Washington Co., Tennessee) in anterior view with lateral articular processes (LAP) indicated by arrows. **A**) reduced LAP on ETMNH 609's left ulna, and **B**) the normal condition on ETMNH 601's right ulna

Fig. 13 Right radius (**A**) and ulna (**B**) of ETMNH 601 (*Teleoceras aepysoma* from Gray Fossil Site, Washington Co., Tennessee) with corresponding muscle scar tubercles indicated by arrows. The tubercles are also present on the left radius and ulna of ETMNH 601, but absent from the radii and ulnae of ETMNH 609

Radius

Included specimens: ETMNH 601, 609; UTK 8.01 (all from GFS and part of the ETMNH collection).

Radii are represented by ETMNH 601, ETMNH 609 and UTK 8.01. Only the left radius of ETMNH 601 is unbroken (Short 2013; Short et al. 2019). All the remaining radii are crushed to some degree, especially around the NK, though all have been reassembled as much as possible. Only UTK 8.01 is incomplete, with most of the anterior diaphysis and proximal portion of the distal epiphysis missing. ETMNH 601 and ETMNH 609 both display differential weathering with the left side more weathered, this difference being starker on ETMNH 609.

Other differences between the two specimens can be attributed to age, with ETMNH 601 possessing more pronounced muscle scarring than ETMNH 609.

The right radius of ETMNH 601 has incipient (CAT1) lipping on the anterior ASTr and ASCap, with some lateral small postmortem fractures. The left radius of ETMNH 601 has CAT1 lipping on posterior ASTr and ASUL1, and taphonomic weathering on anterior ASTr. The right radius of ETMNH 609 has CAT1 lipping on proximal portions of the lateral and medial edges of ASUL1, with some postmortem breakage to the anteromedial edge of ASTr. Both left and right radii of ETMNH 601 have a semi-circular fin/tubercle on posterior surface of diaphysis distal to the NK and parallel to a nutritive foramen (Fig. 13), with the right being taller and more blade-like and the left lower and thicker. These tubercle structures are likely counterparts to the tubercles mentioned previously on ulnae, being probable ossified ligaments/tendons. CAT1-2 lipping around ASUL2 and medial edge of the ASS of ETMNH 601. CAT1 lipping is observed on proximal ASUL2, around the ASL, and anterior ASS of the right radius of ETMNH 609. ASS and ASL have an erosive cavity between them, ~14 mm long, ~1.5-5 mm wide, and ~1.5 mm deep. The left radius of ETMNH 601 has potential CAT1 lipping on ASS medial edge, and folded, arthritic bone on ASS/ASL boundary.

Carpals

Scaphoid

Included specimens: ETMNH 601, 609, 32999, 33000.

Scaphoid is represented by four individuals, ETMNH 601, ETMNH 609, ETMNH 32999, and ETMNH 33000. ETMNH 601 and ETMNH 609 are paired, coming from complete skeletons, while ETMNH 32999 and ETMNH 33000 are represented by a left and right scaphoid, respectively. All except ETMNH 32999 are in good condition, with only the right scaphoid of

ETMNH 601 showing postmortem breakage on the lateral portion. ETMNH 609 has some superficial weathering, while ETMNH 32999 shows more severe random weathering. Short et al. (2019) notes the presence of foramina on all non-articular surfaces. These foramina are also noted on the new material in this study.

Both scaphoids from ETMNH 601 have lipping on the posterior ASR adjacent to the PP, with the right being greater with sharp CAT3 marginal lipping and left lesser CAT2 marginal lipping. The right scaphoid also has CAT1 lipping on medial ASR, potential early CAT2 lipping on ASL1-3, supported by presence of a shelf on ASL2, and a postmortem fracture through ASL3 and the AST. The left scaphoid of ETMNH 601 has CAT1 lipping laterally on ASL3 and AST, and medial on the ASM.

The right scaphoid of ETMNH 609 has superficial weathering three quarters of the way across medially, potentially obscuring evidence for marginal lipping. The left scaphoid of ETMNH 609 has probable CAT1 lipping on ASR and ASL1-3, though weathering makes this observation uncertain. The left's ASM of ETMNH 609 also has likely CAT1 marginal lipping medial.

Scaphoid of ETMNH 32999 has taphonomic features on the anterior of the ASR and ASM, a combination of small postmortem fractures and weathering. ASL2 and ASL3 on ETMNH 32999 show weathering on the articular surfaces, as well as shelves that suggest the once presence of lipping. The ASL2 has CAT2 lipping supported by the presence of a shelf, and an osteophyte on the distal ASL3.

Scaphoid of ETMNH 33000 has CAT1-CAT2 lipping on the ASR supported by shelves. The ASM of ETMNH 33000 has small, irregular pores anterolaterally and CAT2-CAT3 lipping on posterior margin, adjacent to the PP. The anterior ASM and AST on ETMNH 33000 are

separated by a sharp ridge which widens anteriorly into non-articular rugose texturing. The AST has small, uneven pits on the lateral articular surface on ETMNH 33000.

Lunar

Included specimens: ETMNH 601, 609, 33000; UTK 6 (all from GFS and part of the ETMNH collection).

Lunars from GFS consist of those from ETMNH 601 and ETMNH 609, as well as a right lunar from ETMNH 33000 and a left lunar from UTK 6. All are in good condition, with some limited reassembly and reconstruction of ETMNH 601 and ETMNH 609 (Short 2013; Short et al. 2019). LP seems to have been the most susceptible part to postmortem breakage on these specimens. Both lunar processes of ETMNH 601 were reassembled, with only a small fragment absent from the proximal side of the postmortem break on the right, and the posterior surface absent and a small fragment from the distal part of the postmortem break on the left. The LP of the left lunar of ETMNH 609 has been reconstructed. ETMNH 33000 and UTK 6 are fully intact with no significant perceivable taphonomic weathering or fractures. Articular facets of ETMNH 601 appear to have been subject to significant modification in life, and alongside ETMNH 33000, show evidence of lesions.

Both lunars of ETMNH 601 shows significant modification of the ASR, ASS1 and ASS2, forming continuous surface (Fig. 14). Though the connection between ASR and ASS1 is less well developed on the left lunar. The ASR of the right lunar has CAT2 marginal lipping on its anterior and posterior edges. The posterior edge of the left lunar's ASR has a small osteophyte, about 1.5 mm high. The ASS1 of both lunars of ETMNH 601 have CAT1 lipping on its' posterior edge, as evidenced by a shelf and the beginning of a ridge. The proximal end of the boundary of the ASS3 and ASM of the right lunar has a semicircular incision ~4 mm deep and

~6 mm in diameter with two pits within it (~1 mm and ~1.5 mm diameters). ASS3 and ASM boundary on the left lunar has a smaller divot than on the right lunar, with it being half the length (~3 mm) and less than 0.5 mm deep. Both lunars have CAT1 marginal lipping on the posterior end of the ASM. Right lunar has CAT1 lipping on the anterior end of ASUn, and the proximal end of ASS3. Right lunar of ETMNH 601 has probable CAT1 lipping between the ASC1 and ASC2.

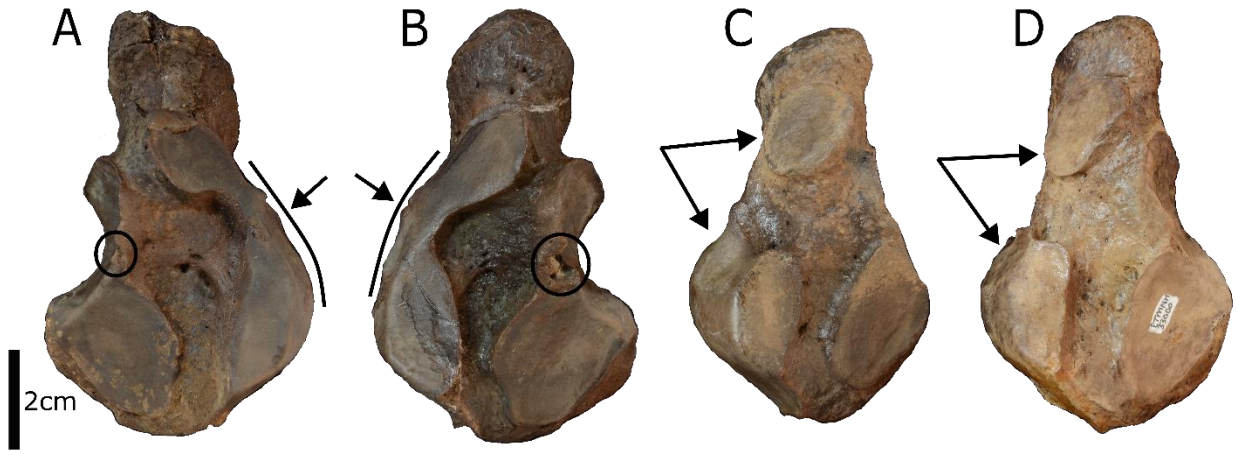

Fig. 14 Lunars of ETMNH 601, 609, and 33000 (all *Teleoceras aepysoma* from Gray Fossil Site, Washington Co., Tennessee) in medial view. Modified articular surface for radius (ASR), 1st articular surface for the scaphoid (ASS)1 and ASS2 surface of the right (**A**) and left (**B**) lunars of ETMNH 601 (denoted by arrows and lines). Unmodified right lunars of ETMNH 609 (**C**) and ETMNH 33000 (**D**) for comparison, with doubled arrows denoting the unconnected ASR and ASS1. Note the osteolytic lesions between the articular surface for the magnum and the ASS3 on the left and right lunars of ETMNH 601 (circles)

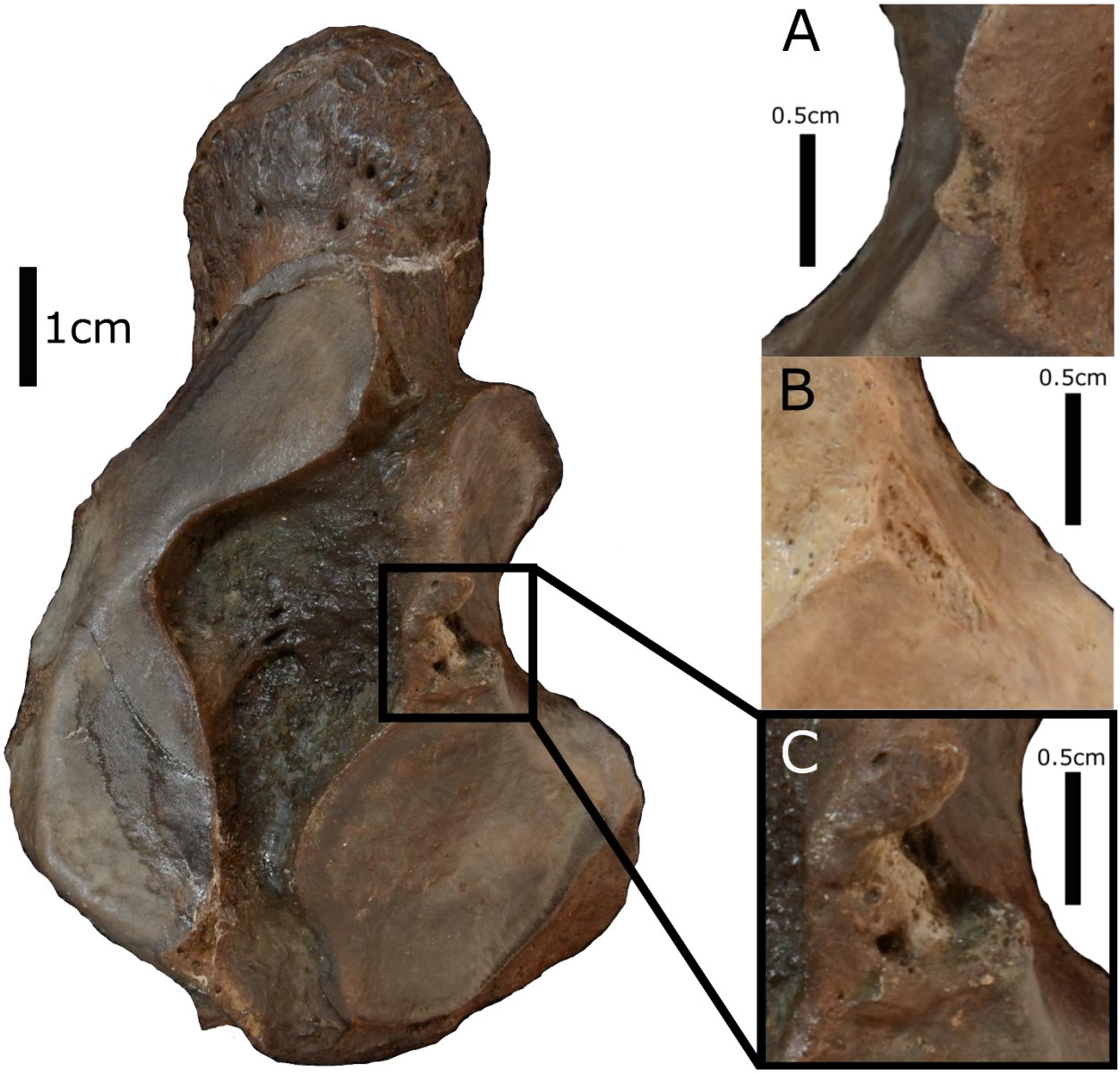

Fig. 15 Left lunar of ETMNH 601 in medial view, with insets showing the articular surface for magnum (ASM)/articular surface for scaphoid 3 (ASS3) boundary of the right lunar of ETMNH 601 (**A**), left lunar of ETMNH 33000 (**B**), and left lunar of ETMNH 601 (**C**) also in medial view (all *Teleoceras aepysoma* from Gray Fossil Site, Washington Co., Tennessee). Insets **A-C** compare varying degrees of osteolysis present on the ASM/ASS3 of ETMNH 601 and ETMNH 33000

In ETMNH 609, the right lunar's ASR and ASS2 form continuous surface with ASS1 being distinct from this, unlike the condition in ETMNH 601 (Fig. 14). Left lunar of ETMNH 609 has more taphonomic weathering than the right, though similarly lacks the connection of ASR/ASS2 to ASS1. Identification of the presence or absence of lipping is potentially skewed by taphonomic weathering. The left lunar's posterior ASR has small postmortem fractures, and its ASS1 is especially worn down anteriorly. ASS3 and ASM of both lunars lack any trace of the divots present in ETMNH 601. On the right lunar of ETMNH 609, the LP is entirely intact, as opposed to the condition in 601. Feature has been repaired/covered on the left lunar during reconstruction.

On ETMNH 33000, the lunar has a somewhat rugose mediolateral ridge across center of proximal ASR (Fig. 16). Small amount of bone loss on distal ASS3 (Fig. 15). Anteroproximally on the ASM is either taphonomic weathering or a similar divot as on the right lunar of ETMNH 601, though broader and shallower (9 mm long, 5.5 mm wide, and 3 mm deep). Some rugose bone texture on distal boundary with the ASUn. Some anterior osteolysis/loss of surface of ASC2.

Fig. 16 Right lunar of ETMNH 33000 (*Teleoceras aepysoma* from Gray Fossil Site, Washington Co., Tennessee) in proximal view. Arrow indicates a lesion on the right lunar's articular surface for the radius on ETMNH 33000, with a low uneven ridge extending laterally then anteriorly, highlighted by line

UTK 6 has CAT1 lipping on ASC2 and a ridge/CAT2 lipping on the medial half of the ASM/ASS3 boundary.

Cuneiform

Included specimens: ETMNH 601, 609, 8271, 33000; UTK 1.06, 5 (all from GFS and part of the ETMNH collection).

Cuneiforms are represented by paired elements from ETMNH 601 and ETMNH 609, right cuneiforms from ETMNH 8271 and ETMNH 33000, and left cuneiforms from UTK 1.06 and UTK 5. All are intact, except for ETMNH 8271 and UTK 1.06, the former was broken in half postmortem, ETMNH 8271 has since been reassembled, and the latter is partial, with the posterior and some distal portions missing. Left elements of ETMNH 601 and ETMNH 609

display taphonomic weathering, consistent with the other elements of these specimens. Like the scaphoids, Short (et al., 2019) notes rugosities and foramina on the non-articular surfaces of the cuneiforms, features also noted on the new material presented here.

On ETMNH 601, the left cuneiform of ETMNH 601 was exposed to more taphonomic weathering, especially anterior side. Both cuneiforms' ASUL have a distally retracted lateral edge. The right cuneiform's ASUL has probable CAT1 anteromedial and posterolateral lipping. Left has CAT1 anterior and posterior lipping on ASUL. The right cuneiform of ETMNH 601 has CAT1 internal lipping between ASL1 and 2, and CAT1 internal lipping on the left's ASL1. CAT1 lipping in present around the ASUn of the right cuneiform, as well as a shallow disc of taphonomic bone loss on anteromedial portion (7.5-8.5 mm diameter, <0.5 mm deep). The right cuneiform has CAT1 lipping around the distal edge of the ASP of, while the left cuneiform has incipient CAT2 lipping around distal edge of ASP. A notable tuberosity is visible between ASL1 and ASP on the right element that is less pronounced on the left. The right cuneiform has a small tuberosity on the proximal end of the ASUL/ASP boundary, not present on the left.

ASUL and ASUn are much less concave on ETMNH 609 than on ETMNH 601, and the tuberosity between ASL1 and ASP is much less pronounced. Both cuneiforms have potential CAT1 anterior lipping on the ASUL. The left cuneiform of ETMNH 609 appears to have been more exposed to weathering, similar to the condition in ETMNH 601. Left cuneiform's ASP appears to have CAT1 lipping on the medial edge, though this is somewhat obfuscated by taphonomic weathering.

On ETMNH 8271, the ASUL has CAT1 anterior lipping, while the posterior edge was worn down postmortem. ASL1 has mild internal lipping, while the ASUn has moderate anterior and posterior lipping. ASP is oddly shaped, being proximal-distal elongated and narrow, with the

boundary between it and the ASUL being less distinct. Tuberosity between ASP and ASL1 is also absent/underdeveloped on ETMNH 8271.

On ETMNH 33000, the cuneiform has an osteophyte on posterior boundary of ASUL/ASL1 (5.7 mm diameter and 1.5 mm relief) and some rugose texturing on anterior end. Anterior ASUL has a small amount of bone loss adjacent to an osteophyte. The ASUL has CAT1 lipping on the anteromedial and distal edges and around the ASP. ASL1 and ASP have a very shallow tuberosity between them, similar to that seen on ETMNH 601 and ETMNH 609.

On UTK 1.06, the ASUL has a small mediolateral incision, with a deep pit at the center, on the center surface (Fig. 17; 5.8 mm wide and 1.3 mm long).

The cuneiform of UTK 5 possesses the tuberosity between the ASL1 and ASP present in ETMNH 601, ETMNH 609, and ETMNH 33000.

Fig. 17 Distal view of UTK 1.06/ETMNH 19280 (*Teleoceras aepysoma* from Gray Fossil Site, Washington Co., Tennessee) cuneiform. Note the mediolateral incision at the center of the articular surface for the ulna, potentially the result of damage to the articular cartilage

Pisiform

Included specimens: ETMNH 601, 609, 8271, 33000.

Pisiforms have been recovered from four individuals, ETMNH 601 and ETMNH 609 preserve both, while ETMNH 8271 and ETMNH 33000 both preserve only the right pisiform. Both ETMNH 601 and ETMNH 609 are in good condition, while the other two show more weathering, particularly ETMNH 8271, where the articular facets are not fully intact.

Pisiforms are more robust and rounded on ETMNH 601 than ETMNH 609 (Fig. 18). The pisiforms of ETMNH 601 and ETMNH 609 have a structure buttressing the ASC dorsally which matches to the ASL1/ASUL tuberosity on the cuneiform. Like the tuberosities, these 'buttresses' are significantly more robust on ETMNH 601 than ETMNH 609. ASC is larger and more complexly shaped on ETMNH 601 than ETMNH 609. Of particular note is a medial hook-shaped osteophyte flush with the articular surface, on the ventral portion of the articular surface. Also, the articular surface has a facet for the ulna in addition to the one for the cuneiform, though the ASUL is still relatively smaller than the condition in the GFS *Tapirus polkensis*. On the right pisiform of ETMNH 601, the ASUL is proportionally smaller than on the left pisiform. ASC/ASUL boundary on the right pisiform has a robust, conical osteophyte on the lateral edge. The left pisiform has a similar, less pronounced, osteophyte. Advance CAT1 lipping, verging on CAT2, on the ventral edge of ASC potentially associated with the lateral osteophyte. Left pisiform 'buttress' is less pronounced than the structure found on the right pisiform. The degree of ventral lipping on the left pisiform is obfuscated by postmortem fractures, though adjacent lipping is roughly CAT1.

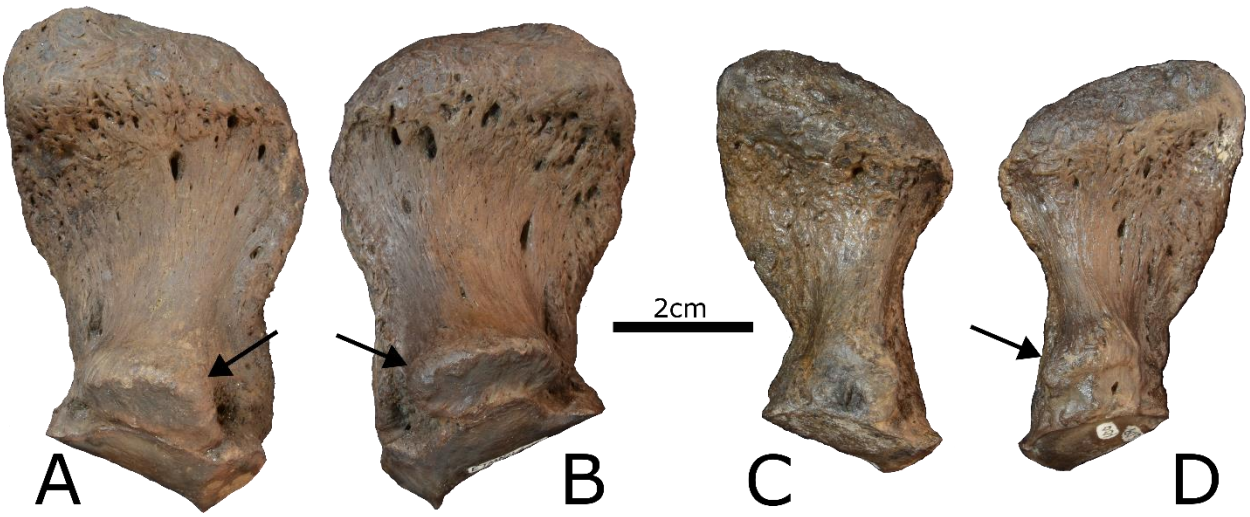

Fig. 18 Pisiforms from ETMNH 601 and ETMNH 609 (both *Teleoceras aepysoma* from Gray Fossil Site, Washington Co., Tennessee) in dorsal view. Note the robust left (**A**) and right (**B**) pisiforms of ETMNH 601, and the more gracile left (**C**) and right (**D**) pisiforms of ETMNH 609. Also visible on ETMNH 601 pisiforms are the 'buttresses' (arrows) adjacent to the articular surface, the beginnings of which is visible on the right pisiform of ETMNH 609 (arrow)

The pisiforms of ETMNH 609 are more gracile and angular, the ASULs less widened, and 'buttresses' less developed than on 601. Right-left pattern on ETMNH 609 follows from ETMNH 601, with the left pisiform having a larger ASUL and right pisiform having a larger 'buttress'. Osteophytes adjacent to ASC/ASUL boundary on the pisiforms of ETMNH 601 are absent from both ETMNH 609 pisiforms. Both pisiforms from ETMNH 609 have CAT1 lipping on the ventrolateral corner of the ASC.

The right pisiform of ETMNH 8271 suffers from postmortem breakage and weathering around the articular surfaces, potentially including broken osteophytes, but is otherwise mostly intact. Overall, it is less angular than ETMNH 609, but less robust than ETMNH 601. ASUL of ETMNH 8271 is proportionally the largest, with it being the same size as the same structure on the larger ETMNH 601's right pisiform. The dorsal 'buttress' is absent in ETMNH 8271,

mirroring the condition of the ASL1/ASP tuberosity on the cuneiform, though a small structure appears to have been in the process of protruding forward from the midpoint of the 'pinch' of the pisiform (sensu Short et al. 2019).

The pisiform of ETMNH 33000 is intermediate in form between ETMNH 601 and ETMNH 609, though the 'buttress' is less well-developed than either. ASUL/ASC boundary has low, rounded osteophytes on the dorsal end with a possible additional osteophyte developing on the ventral end, as on ETMNH 601.

Trapezium

Included specimens: ETMNH 601, 609, 8271, 13236, 33000.

Trapeziums are present in five specimens with ETMNH 601 and ETMNH 609 having both, and ETMNH 8271, ETMNH 13236, and ETMNH 33000 having only one. Sidedness of ETMNH 8271 is uncertain, though likely left given ill fit to the right trapezoid. ETMNH 13236 sidedness cannot be determined due to being isolated and misshapen. ETMNH 33000 is identified as a left. All are intact.

AST on the right trapezium of ETMNH 601 has CAT2-3 lipping with a ventral projection creating a contact with MC2. Left trapezium's AST has only CAT2 lipping and lacks the ventral projection present on the right trapezium. A divot on the opposite side of the right trapezium's AST corresponds to a region of osteolysis on the trapezoid. The distal rugosity on the right trapezium of ETMNH 601 is more 'U'-shaped than in ETMNH 609. The ventral portion of the left trapezium's distal rugosity has a more pronounced ventral point than the right.

The right trapezium of ETMNH 609 has early CAT2 lipping on the AST and its' distal rugosity is 'V'-shaped, as described by Short et al. (2019). Left trapezium's AST also has early

CAT2 lipping and, in addition, has developed an oblique articular surface with MC2. The distal rugosity of the left is more ‘U’-shaped than the right and has a less pronounced ventral point.

The trapezium of ETMNH 8271 has a narrower AST than the previously described specimens, has late CAT1 lipping, and has developed an oblique contact with MC2, as on the left trapezium of ETMNH 609. Trapezium’s distal rugosity is more bulbous and less symmetrical than in ETMNH 601 and ETMNH 609.

In ETMNH 13236, the AST is an underdeveloped circular surface skewed to the right of the bone, with CAT2 lipping. Trapezium’s distal rugosity is notably asymmetrical compared to ETMNH 601 and ETMNH 609 (Fig. 19).

On ETMNH 33000, the posterior portion of the trapezium has an extended process that corresponds to the irregular surface on the left trapezoid. Also, the ventral surface of the rugosity has a large concave depression/cavity (~12 mm ant-post, ~7 mm med-lat, and ~2.5 mm deep).

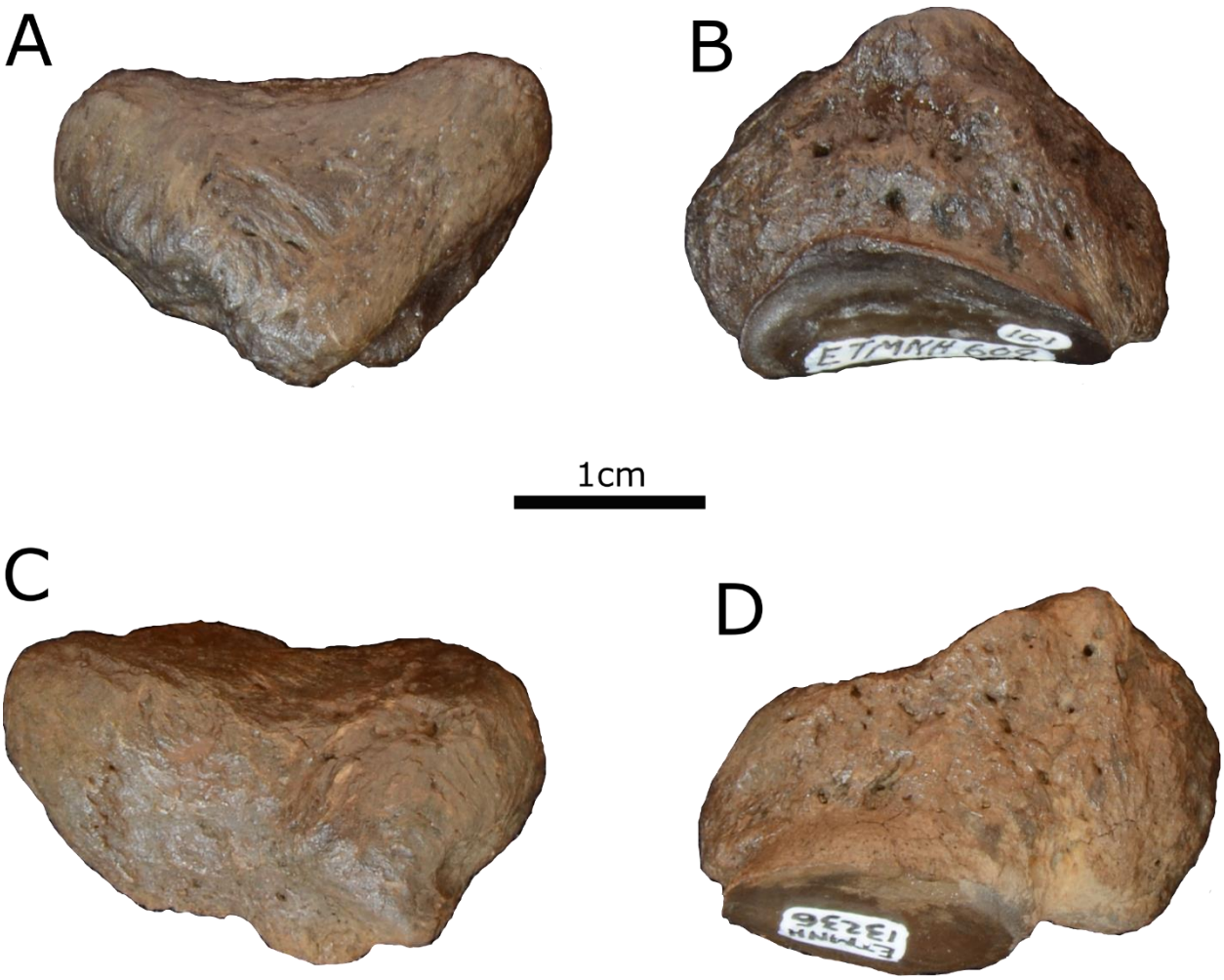

Fig. 19 Right trapeziums of ETMNH 13236 and ETMNH 609 (*Teleoceras aepysoma* from Gray Fossil Site, Washington Co., Tennessee). Note the ETMNH 609's right trapezium in medial (**A**) and distal view (**B**), in comparison to the lopsided, irregularly shaped ETMNH 13236 in medial (**C**) and distal view (**D**)

Trapezoid

Included specimens: ETMNH 601, 609, 8271, 33000.

Trapezoids are represented by four specimens: ETMNH 601, ETMNH 609, ETMNH 8271, and ETMNH 33000. All specimens, except ETMNH 8271, preserve both left and right elements. All are in at least relatively good condition, having sustained only limited postmortem

defects, with ETMNH 601 having had a small fragment fracture postmortem and been reattached in prep.

On ETMNH 601, the right trapezoid's ASS is notably bowl-shaped with anterior and posterior CAT1 lipping, as well as bone loss between it and the ASTm, being 10 mm long ant-post and 2.5 mm deep. Left trapezoid of ETMNH 601 has a less dramatically bowl-shaped ASS than the right, anterior and posterior CAT1 lipping, and distinct separation from ASTm. In addition to the divot/cavity on the right trapezoid, the ASTm has CAT1 anterior and posterior lipping on the right trapezoid. The left trapezoid's ASTm is distinctly teardrop-shaped, with the apex pointing anteriorly and somewhat distally, and with anterior, posterior, and proximal CAT2 lipping with a visible shelf. ASMC2 on both trapezoids have CAT2 (evidenced by shelf) anterior lipping and the right CAT1 posterior lipping. ASMC2/ASM boundary on the left trapezoid has a small osteophyte on the posterior edge. The right trapezoid's ASM has a small posterior osteophyte and CAT2 anterior lipping on the right trapezoid, while the left trapezoid has only CAT1 anterior lipping.

ASS of the right trapezoid of ETMNH 609 is less bowl-shaped than the condition in ETMNH 601. Left trapezoid's ASS has potential CAT1 anterior lipping and CAT2 posterior lipping, forming a distinctly sigmoidal edge, and with distinct separation from ASTm. ASTm is ovoid in shape on the right trapezoid with CAT1 posterior lipping. On the left trapezoid, the ASTm is teardrop-shaped, as on ETMNH 601's left trapezoid, with potential CAT1 proximal lipping. The right trapezoid's ASMC2 has CAT1 anterior lipping and potential beginnings for an osteophyte, similar to that on the left of ETMNH 601, posteriorly near the lateral connection to the ASM. The ASMC2 of the left has CAT1 anterior and posterior lipping near the lateral

connection with ASM, as on the R. trapezoid. Both ETMNH 609 trapezoid's ASM have CAT1 anterior lipping, and the right trapezoid has CAT1 posterior lipping.

ASS of the trapezoid of ETMNH 8271 has CAT1 anterior and posterior lipping with small postmortem fractures and an irregular ridge between it and the ASTm. ASTm has CAT2-3 lipping with an extensive shelf. The ASMC2 has CAT1 anterior lipping, as well as a series of parallel lateral striations inconsistent with scratches caused by tools in fossil preparation. ASM has CAT1 anterior lipping and the beginnings of a small posterior projection/osteophyte, similar to the right trapezoid of ETMNH 601.

Right trapezoid of ETMNH 33000 has a developing spur on posterolateral ASS (advanced CAT2 lipping). Left trapezoid has extensive CAT2 lipping around the ASS, osteophyte mirrored from the right trapezoid. Right's ASTm has CAT2 lipping with visible shelves. Both trapezoids have irregular bone loss of rugose bone posterior to ASTm. The right trapezoid has a stretched connection between ASMC2 and ASTm with a tactile shelf (~3 mm dors-vent) due to marginal lipping (CAT2), distinctly different from the bone loss on right ETMNH 601. The left trapezoid also has a stretched connection of AST and ASMC2, suggesting at least CAT1 lipping. The left trapezoid's ASMC2 has a small anterolateral osteophyte, and CAT1 anterior lipping on the ASM of the same bone.

Magnum

Included specimens: ETMNH 601, 609, 8271, 8516, 28178, 33000; UTK 4.01, 10 (all from GFS and part of the ETMNH collection)

Magnums are represented by material from eight specimens, with most being intact except for ETMNH 8271 which is heavily eroded, only preserving the ASS, ASL, and part of the AST. Only ETMNH 601 and ETMNH 609 are paired (Short 2013; Short et al. 2019). ETMNH

8516 is a different color from the rest, being orange, suggesting different depositional sediments or exposure.

ASS of the right magnum of ETMNH 601 has CAT1 anterior lipping and folds/creases medially between the main surface and raised portion. The left magnum of ETMNH 601 has more extensive folds/creases between the horizontal and vertical proximal surfaces that exacerbates laterally (Fig. 20). The right magnum's ASL has CAT1 lipping posteriorly and laterally, while the left magnum's ASL has CAT1 lipping lateral and a spherical pit (~1 mm diameter) on lateral edge. The AST of the right magnum has CAT1/2 lipping posteriorly, including a small projection/spur corresponding to the one on the trapezoid. Left magnum's AST has CAT2 lipping posterior, with the beginnings of spurs. On the posterior portion of the boundary between the AST and ASMC2 of the right magnum is a small, roughly rectangular excrescence/osteophyte (~8.5 mm ant-post, ~5.75 mm prox-dist). The right magnum's ASMC2 has CAT1 anterior and posterior lipping. ASMC2 of the left magnum has probable CAT1 lipping anterior and posterior, with some CAT2 lipping and an uncurled spicule on the posterior AST/ASMC2 junction. In addition to this, the left magnum has a small developing osteophyte on the posterior edge between ASMC2/ASMC3. Articular surface for metacarpal 3 (ASMC3) on the right has CAT1 posterior lipping and has a much more oblique lateral portion than on ETMNH 609, with a large lateral cross-section/footprint. The left magnum has a similar but less extreme condition to that of the right magnum. ASMC3 has CAT1/2 lipping anterior and posterior, and an osteophyte on the posterior portion of the ASUn/ASMC3 (~2.85 mm across). The posterior portion of this surface projects down much further than on ETMNH 609. The right magnum's ASUn has a small, fractured corner on the anterior portion of the ASUn/ASMC3 boundary, most

likely postmortem. The ASUn of the left magnum has probable bone loss on antero-proximal edge, perforated with numerous small, less than 1 mm, pits.

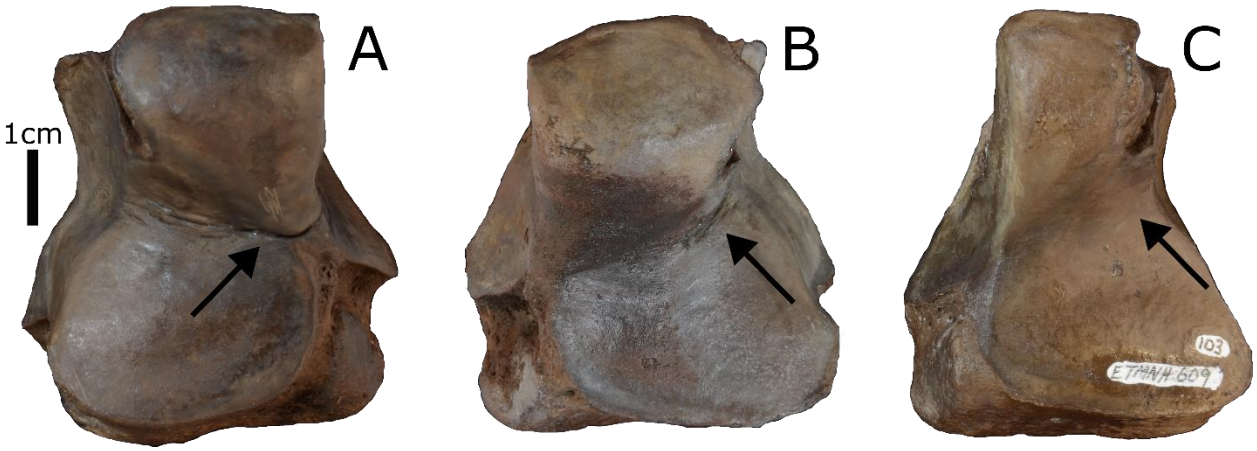

Fig. 20 Magnums of ETMNH 601 and ETMNH 609 (*Teleoceras aepysoma* from Gray Fossil Site, Washington Co., Tennessee) in proximal view. **A**) left and **B**) right ETMNH 601 with crease/fold on transition between horizontal and vertical portion of the articular surface for scaphoid (ASS), denoted by arrows. **C**) unmodified ETMNH 609 right lacking the previously noted crease

ASS of the right magnum of ETMNH 609 is unmodified. The ASL has CAT1/2 lipping laterally. AST has potential CAT1 lipping posterior. ASMC3 has CAT1/2 lipping anterior and posterior. Left magnum's AST and ASMC2 have CAT2 lipping posterior, and the ASMC3 has CAT1 lipping anterior and posterior.

ETMNH 8271 has early CAT2 lipping on the medial portion of the ASL.

The left magnum of ETMNH 8516 was heavily weathered postmortem and has multiple small fractures, with all articular surfaces showing some evidence of lipping, either CAT1 or 2, with prominent spurs being identifiable on the anterior portion of the ASMC2.

Left magnum of ETMNH 28178 has mild folds on the bend in the ASS, similar to the condition on the right magnum of ETMNH 601, though they are more severe laterally on

ETMNH 28178. Adjacent to this on the ASUn are some small perforations (less than 1 mm), probably postmortem given the crisp edges. ASL has CAT2 lipping medial. The AST and ASMC2 have CAT2 lipping posterior with a visible shelf. Rather deep bone loss on the medial ASS and anterior AST (~2.9 mm long, ~3.4-6 mm wide). ASMC3 has CAT1 lipping on anterior and posterior edges, and the ASUn has potential CAT1 lipping anteriorly. The posterior portion of the ASUn exhibits some bone loss (~7.3 mm prox-dist, ~2.5 mm ant-post).

Left magnum of ETMNH 33000 has little to no folding on the ASS, though has a cavity instead (~3 mm across, likely taphonomic), as well as some anterolateral bone loss. ASL has an osteophyte on the posterolateral edge, and the AST has CAT2 lipping posterior with a visible shelf. ASMC2/ASMC3 boundary has moderate bone loss, and the ASMC3 has CAT1 lipping anterior and posterior. ASUn has some limited bone loss posteriorly, and CAT1 lipping on anterior edge.

The left magnum of UTK 10 has bone loss on the posterior of the ASL, between the dorsal and ventral portions of the ASU, and on the posterior of the dorsal ASU. ASS bend has mild wrinkling/folds, and the ASMC3 has posterior CAT1 lipping.

Right magnum of UTK 4.01 has bone loss on the anterolateral portion of the ASS (~6.5 mm long, ~2.8 mm deep) and a small amount on the anteromedial portion (~3.75 mm, ~2.25 mm). ASL has CAT2-1 lipping posterior-medially, while the AST has advanced CAT1/early CAT2 posterior lipping. AST and ASMC2 have some bone loss between their posterior edge, and the anterior portion of the ASMC2/ASMC3 boundary has an irregular, raised, porous feature (~3 mm across), likely some combination of osteophyte and osteolysis. ASMC3/ASU boundary has postmortem breakage on the posterior (~7.4 mm ant-post, ~3.75 mm prox-dist).

Unciform

Included specimens: ETMNH 601, 609, 8271, 21296, 33000; UTK 4 (all from GFS and part of the ETMNH collection)

GFS unciform sample consists of examples from six specimens, three paired: ETMNH 601, ETMNH 609, and ETMNH 8271, and three individual left elements: ETMNH 21296, ETMNH 33000, and (UTK “4”). Most are intact with only three needing reassembling, the UnP of the right unciforms of ETMNH 601 and ETMNH 8271, and the main body of the right unciform of ETMNH 609 having been split postmortem. Lefts of both ETMNH 601 and ETMNH 609 display lateral weathering. The drastically different coloration of ETMNH 21296 and UTK “4” (orange and white, respectively) from other specimens is the result of differing preservation and weathering; with mentioned elements having been recovered after the early road work in oxidized sediment and being exposed to recent weathering.

On ETMNH 601, the right unciform’s UnP has been reassembled from postmortem breakage, with at least two fragments still missing; while the left unciform of ETMNH 601 is intact, though the lateral portion has some weathering. The unciforms have a lateral tuberosity on the anterior portion, which is more pronounced on ETMNH 601 than on ETMNH 609, especially on the left unciform. The left unciform has small spurs on the anteromedial edge of ASC (~5 mm). The ASL has CAT1 anterior and posterior lipping, early CAT2 anterior lipping on ASM, CAT1 posteromedial lipping on the ASMC4, and early CAT2 lateral/proximal lipping on the ASMC5 of the right unciform. The left unciform’s ASM has CAT1 anterior lipping. The left unciform has an exostosis located toward the anterior end of the ASC/ASL boundary (previously mentioned osteophytes), and on the posterior ASMC3/ASMC4 wear boundary (~1.5 mm med-lat and ~2.3 mm ant-post). The left unciform’s ASMC5 has CAT1 lateral lipping.

On ETMNH 609, the right unciform's anterior lateral rugosity is equal to that of the left unciform's. The right unciform's ASC/ASL boundary has a raised bone ridge along the anterior half. The left unciform's ASC has probable CAT1 anterior and lateral lipping. The right unciform has CAT1 posterior lipping on the ASM. The right unciform's ASMC3 has CAT1 posterior lipping. The right unciform has CAT1 anterior and CAT2 posterior and lateral lipping with visible shelf on ASMC4. On the left unciform ASMC4 has CAT1 anterior and lateral lipping.

The right unciform of ETMNH 8271 has developing osteophytes on the anterior and posterior ends on the ASC/ASL boundary. The right unciform has early CAT2 lipping on the ASC. The left unciform has early CAT2 shelf on the ASC's anterior edge. Both unciforms have CAT1-2 lateral lipping on ASMC4. The left unciform has less developed osteophytes on ASC/ASL boundary than on right.

The left unciform of ETMNH 21296 exhibits little taphonomic weathering and fractures. Its anterior lateral tuberosity is roughly equivalent to the right unciform of ETMNH 601. The ASL and ASM have CAT1-2 posterior lipping, and the ASM is eroded around its midpoint. ASMC3 has early CAT2 lipping posterior. ASMC4 has CAT1-2 lipping. The anterior end of the ASMC3/ASMC4 boundary has circular osteophyte (Fig. 21; ~6 mm ant-post, ~3.75 mm med-lat) with a pit in the middle (~1.6 mm diameter).

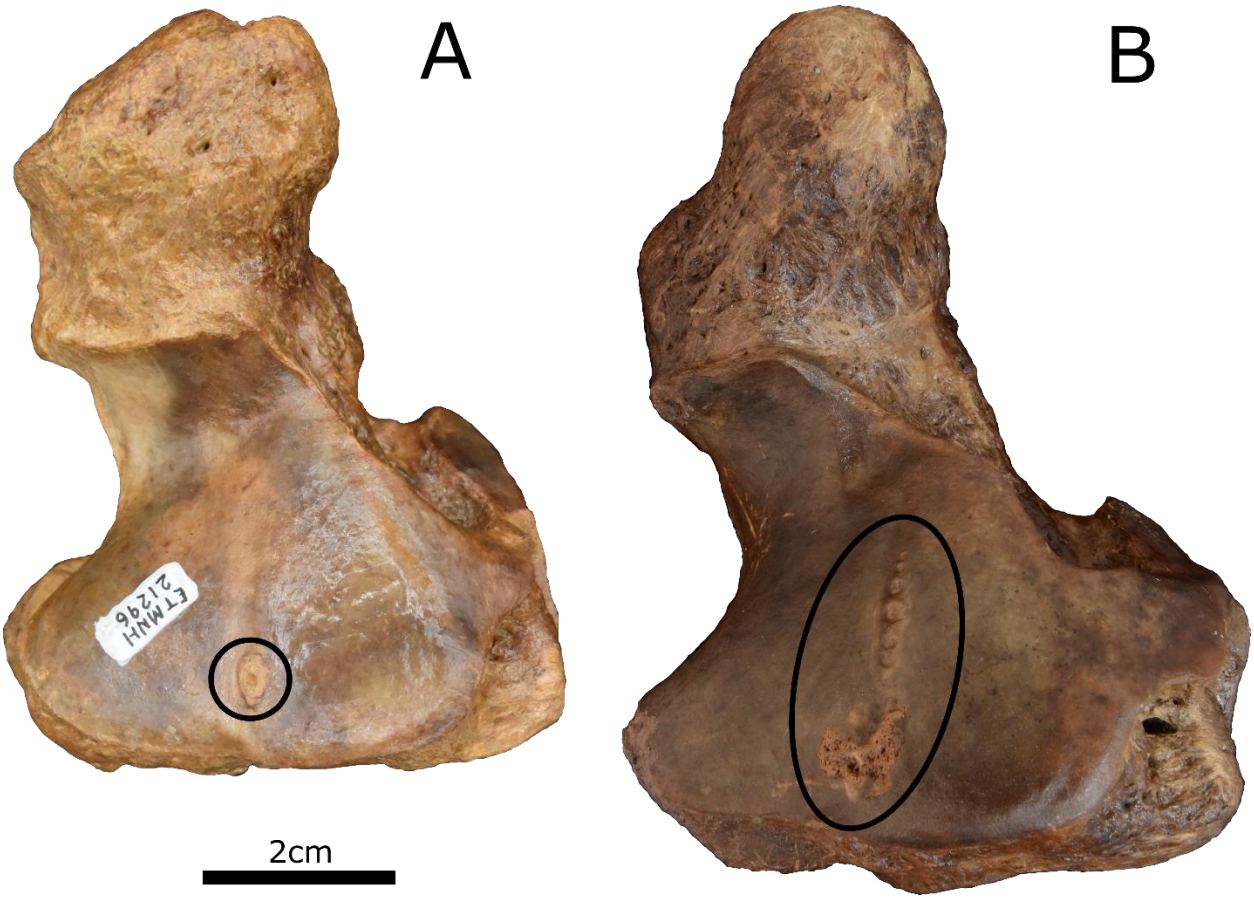

Fig. 21 Unciforms of ETMNH 21296 (**A**) and ETMNH 33000 (**B**) (both *Teleoceras aepysoma* from Gray Fossil Site, Washington Co., Tennessee) in distal view. Note the lesions/osteophytes (circled) on the boundary of the articular surfaces for the 3rd and 4th metacarpals of both

On ETMNH 33000, the left unciform has small osteophytes on the anterior portion of ASC/ASL boundary. The ASC has CAT2 posterior lipping with shelf. The ASMC3 has CAT2 posterior lipping. The ASMC3/ASMC4 boundary has a patch of foamy, irregular bone on the anterior portion (Fig. 21; ~8 mm med-lat, ~6.75 mm ant-post). Posterior to this in a line of 6 regular circular pits (~13 mm long), with the first two being equal sized (~1.7 mm), the third being the largest (~2.1 mm), fourth next largest (~1.9 mm), and last two being the smallest (~0.95 mm; Fig. 21). The ASMC4 has probable CAT1 anterior and posterior lipping, and bone

loss of anterolateral (~14 mm wide, ~5.3 mm deep) and posterolateral (~6.5 mm med-lat, ~4.6mm ant-post) edges.

On the unciform of UTK 4, the anterior ASC has 4-5 slight fragments taken out of the surface, with these fractures probably being preparation related. The unciform has a small, likely taphonomic, fracture on the posterior end of the ASC/ASL. The anterior edge of the ASM has an additional taphonomic fracture. The unciform has CAT1-2 lipping around the ASMC4, and CAT2 lipping on lateral edge.

Metacarpals

Included specimens: ETMNH 601, 609, 8271, 20412, 32999, 33000; UTK 8.03, 8.04 (all from GFS and part of the ETMNH collection).

ETMNH 601 has a complete set of metacarpals, with the right MC3 having been broken and reassembled. As previously mentioned, the elements of ETMNH 601 display a more robust and modified appearance than ETMNH 609, suggestive of a more advanced age. Additionally, ETMNH 601 stands out as the only specimen recovered thus far from GFS to possess unfused 5th metacarpals, accordance with Short's findings (Short 2013; Short et al. 2019). Like ETMNH 601, ETMNH 609 has a complete set of metacarpals, being largely intact—barring some small postmortem fractures on the postero-proximal portions. ETMNH 609 shows differential weathering, with anterior of the left metacarpals and right MC2, and the medial half of MC3 displaying more weathering than the rest of the bones' surface, in accordance with previously mentioned weathering phenomena. ETMNH 8271 has both MC4s, though only right MC2 and MC3, which was broken and reassembled. ETMNH 20412 is represented by a partial MC4 that is in poor condition and heavily weathered, with the distal end being the most broken, and missing some fragments. ETMNH 20412 in too poor a condition to make any meaningful

observations and therefore will be excluded. As of time of writing, ETMNH 32999 has both MC2s and MC3s, while MC4s have yet to be prepped. ETMNH 32999 is quite weathered and has separated distal epiphysial plates. The latter's condition suggests ETMNH 32999 represents an immature individual, as the growth plates have not completely fused, a marker of maturity. ETMNH 33000 has only the left MC4. The metacarpals will be discussed as separate elements going forward, referenced as Metacarpal 2, Metacarpal 3, and Metacarpal 4, respectively.

Metacarpal 2

Included specimens: ETMNH 601, 609, 8271, 32999; UTK 8.03, 8.04 (all from GFS and part of the ETMNH collection).

On ETMNH 601, the AST of the right MC2 has an anteromedial osteophyte, which was broken postmortem, and CAT1 posterior lipping. The left MC2's AST has potential anterior and posterior CAT1 lipping. The intermediate relief between AST and ASM is pronounced on both right and left MC2s, with it forming a sharp ridge on the left element. The right MC2's ASM has CAT1 posterior lipping. Both right and left's ASM/ASMC3 boundary shows wear with visible porosity (<1 mm). ASMC3 has moderate anterior lipping and mild distal and posterior lipping on the right MC2. The left MC2's ASMC3 has advanced anterodistal CAT1 lipping. ETMNH 601 has a robust, rounded, and rugose proximodistal PR, distinctly more so than the condition seen in ETMNH 609 (Short 2013; Short et al. 2019). This is more notable of the right MC2 than the left MC2. The ASPP2 on the right MC2 has early CAT2 lipping on proximal edge, with a visible shelf. The left MC2 only has ASPP2 has probable CAT1 lipping on proximal edge. On both MC2s, ASSD1 and 2 have clear wear facets indicating their positions in life, with ASS2 showing more wear (numerous small perforations/pores).

The MC2s of ETMNH 609 are less broad than those of ETMNH 601. The lateral posterior portion of the right MC2's AST exhibits postmortem breakage and weathering, obfuscating identification of the presence or absence of lipping there. The left MC2's AST has CAT1 anterolateral and posterolateral lipping. Intermediate relief between AST and ASM of both ETMNH 609 MC2s is less pronounced than on ETMNH 601. The left MC2's ASMC3 has probable CAT1 anterior and posterior lipping. The PR is much less pronounced and more blade-like on both of the MC2s from ETMNH 609, the right more so than the left, than compared to the condition of ETMNH 601 (Short 2013; Short et al. 2019). The ASPP2 of the right MC2 shows a worn proximodistal surface, likely from prep. work.

On ETMNH 8271, the right MC2's AST has CAT1 marginal lipping, verging on CAT2 posteromedially. A small extension for articulation with trapezium is also present (see above mentioned modification of right trapezium). The condition of the AST and ASM intermediate relief of ETMNH 8271 is intermediate between that of ETMNH 601 and ETMNH 609. The ASM has a likely developing osteophyte on its anteromedial corner. The ASM/ASMC3 boundary has probable postmortem bone loss anteriorly, and the posterior portion of the ASM and ASMC3 suffer from postmortem breakage. The ASMC3 has CAT2 lipping along the distal edge, and CAT1 lipping on the anterior edge. As with other features on ETMNH 8271, the PR's condition is intermediate between that of ETMNH 601 and ETMNH 609. It is more robust and rounded than ETMNH 609, though not as pronounced or rugose as ETMNH 601. The proximal portion of ASPP2 has early CAT2 lipping. The ASSD1-2 wear facets are less distinct on ETMNH 8271's MC2, than the condition of the same on ETMNH 601.

Both MC2s from ETMNH 32999 are missing the distal epiphysis and the proximal epiphysis suffers from postmortem breakage and weathering, especially around the

posteromedial AST and the ASM on the right, and with the ASM and ASMC3 broken off on the left. Both elements' AST have potential CAT1 anterior lipping, though this diagnosis is uncertain due to significant taphonomic weathering.

The UTK specimen is significantly weathered, so the presence of some features may be obfuscated. The PR is more developed than on ETMNH 8271, but less robust than that of ETMNH 601. The ASS2 has a posteriorly concave depression on anterior edge/boundary, suggested to be an indicator of the in-life extent of the cartilage pad by Wallace (S.C. pers. comm., 2023), a feature also noted in the articular surfaces of the GFS *Tapirus polkensis* population.

Metacarpal 3

Included specimens: ETMNH 601, 609, 8271, 32999.

On ETMNH 601, the right MC3 was broken but has since been reassembled (some small fragments are still missing), while the left MC3 is intact. The ASMC2 of both the right and left MC3 have probable early CAT2 lipping, given the presence of a visible shelf. The right's ASM has CAT1-2 anterior lipping and CAT1 posterior lipping. The left's ASM has CAT1 anterior lipping, though increases to CAT2 laterally and lateral posterior edge approaches CAT1 lipping. The CAT2 anterior lipping of the left's ASM is associated with bone loss. The ASMC4 on the right has probable CAT1 anterodistal lipping, while the left's ASMC4 has probable CAT2 lipping. Both MC3s have proximal CAT2 lipping on the ASPP3. The right MC3 has notable uniform perforations (<1 mm) on the apices of the ASSD1-2 wear facets, probably from preparation.

The right MC3 of ETMNH 609 has CAT2 lipping on its' ASMC2. ASMC2 of the left MC3 has CAT1 anterior and posterior lipping and CAT2 distal lipping. The ASM of the right

MC3 has CAT1 anterior and posterolateral lipping, and the left's ASM has CAT1 anteromedial lipping. ASU and ASMC4 suffer from posterior postmortem breakage on the right MC3, with nearly half the ASMC4's surface missing. The left's ASMC4 has a small divot (~4 mm across) adjacent to the boundary with ASU near the posterior end (Fig. 22). Whether this is pre- or postmortem is uncertain. The right's ASPP3 has CAT2 proximal lipping, while the left's ASPP3 has little to no lipping.

On the right MC3 of ETMNH 8271, the ASMC2 has early CAT2 distal lipping. The ASU has CAT2 anterior lipping and small osteophytes (ridge ~8 mm long) on the boundary with ASMC4. The ASMC4 has CAT1 lipping, and the ASPP3 has CAT2 proximal lipping.

As on the MC2s of ETMNH 32999, the MC3s distal epiphyses are detached. Both MC3s have potential CAT1 lipping around intact articular surfaces, though weathering obscures this somewhat.

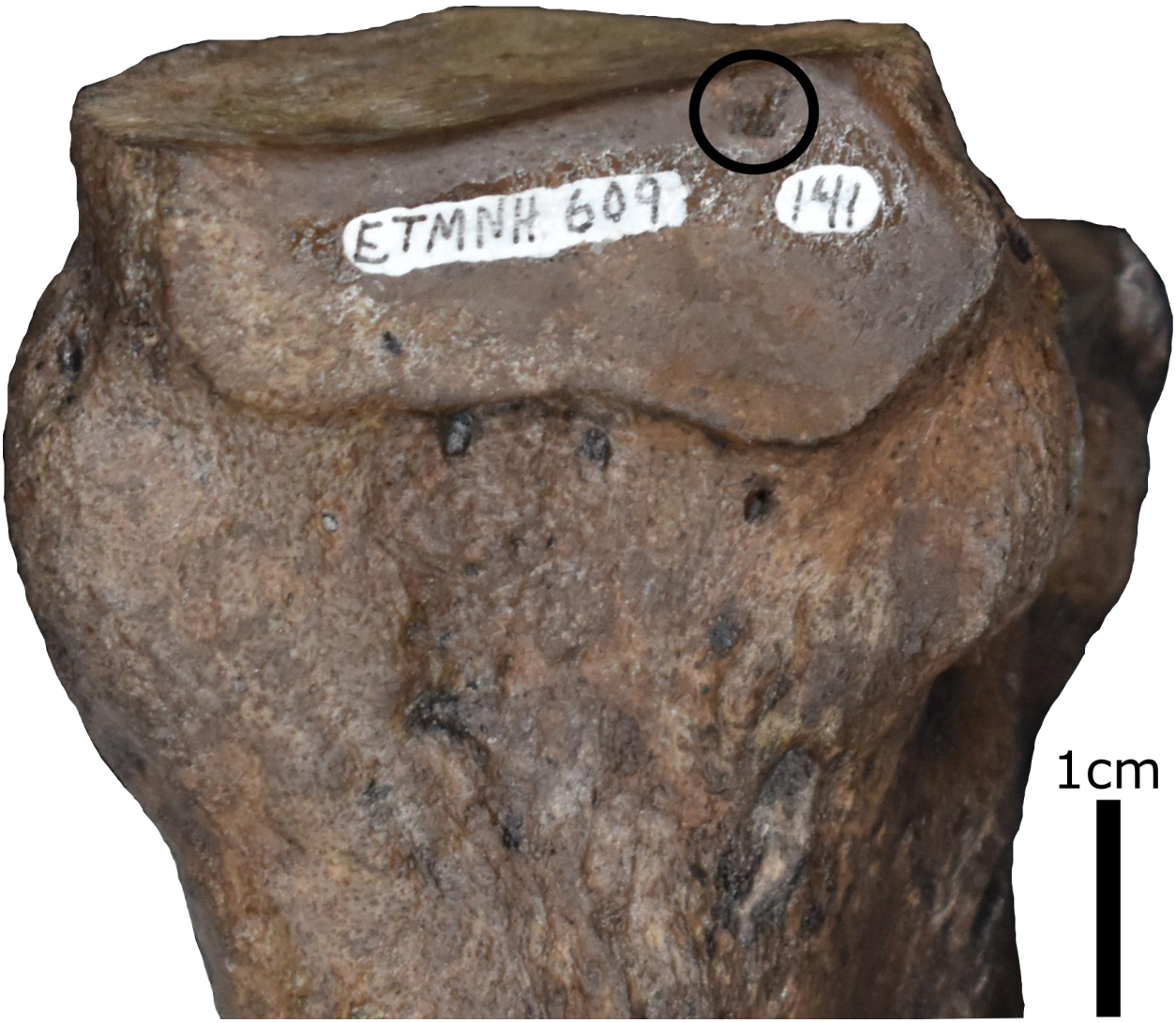

Fig. 22 Lateral view of left metacarpal 3 of ETMNH 609 (*Teleoceras aepysoma* from Gray Fossil Site, Washington Co., Tennessee). Note the defect in the articular surface for metacarpal 4 (circled)

Metacarpal 4

Included specimens: ETMNH 601, 609, 8271, 20412, 33000.

Both MC4s from ETMNH 601 have CAT1 lipping on the ASMC3 and visible sesamoid wear facets.

The right MC4 ASUn has medial postmortem breakage on ETMNH 609. The ASMC3 of the right MC4 has CAT1 lipping. Both elements' have a patch of porous surface on the distal-medial ASPP4 (~15 mm across, pores <1 mm) and visible sesamoid wear facets as on the MC4s of 601.

On ETMNH 8271, the right MC4 has CAT1 lipping around both the ASUn and ASMC3, potentially verging on CAT2 in some places. The left MC4 has CAT1 lipping on ASMC3. The right MC4 has CAT2 lipping on proximal edge of ASPP4. Potential CAT2 lipping on the proximal ASPP4 on the left MC4 is bolstered by presence of a shelf.

The left MC4 of ETMNH 33000 has CAT1 lipping around the posterior of the ASUn and ASMC3, as supported by a notable osteophyte (~0.8 mm) on the posterior edge of the ASU/ASM boundary, and the distal ASMC3. The MC4 has CAT2 lipping on proximal ASPP4.

Manual Phalanges

Included specimens: ETMNH 564, 601, 609, 743, 769, 3755, 5233, 8271, 17357, 19280, 32999; UTK 2.02, 14.xx, 15.xx (all from GFS and part of the ETMNH collection).

Phalanges have been recovered from 15 specimens, some represented by full sets (ETMNH 601 and ETMNH 609), while others are only isolated elements (ETMNH 564 and ETMNH 769). Preservation is generally good with only a handful displaying any significant taphonomic defects, weathering or otherwise (ETMNH 769 broken into halves, and ETMNH 33000 showing notable weathering). The descriptions will be sectioned into proximal, medial, and distal phalanges.

Proximal Phalanges

Included specimens: ETMNH 601, 609, 769, 3755, 8271, 17357, 32999; UTK 2.02, 14.xx, 15.xx (all from GFS and part of the ETMNH collection)

On ETMNH 601, the right digit II proximal phalanx suffers from small postmortem fractures on the anterior edge of ASMC2, potentially to a developing lip (potentially CAT1 verging on CAT2, shelf present around medial, anterior, and lateral edges). The distal surface has two distinct lobes of similar size with less medial tapering than on ETMNH 609. The ASMP2 has pinched bone on the posterior, between the two lobes. This feature is more defined and accented by early CAT2 lipping on the left digit II phalanx. The left also has some perforations under anterior edge of ASMC2. The right digit III proximal phalanx of ETMNH 601 has a large bone loss cavity (~12.9 mm wide, ~5.9 mm ant-post, ~5.25 mm deep) under the central AAF with notable perforation, biased medially. A smaller cavity is medially adjacent to the large cavity, under a lateral rugosity (~4 mm wide, ~4.2 mm ant-post, ~2 mm deep). Similar perforations are on the ventral surface of the left digit III phalanx (Fig. 23), though it is more extensive with there being two cavities, one lateral leaning (~13 mm wide, ~5 mm ant-post, ~3.7 mm deep) and one medial leaning (~15.3 mm wide, ~6.6 mm ant-post, ~4.7 mm deep), with notable bone loss. The right digit IV proximal phalanx of ETMNH 601 has fractured anterior to marginal lipping on the ASMC4, with cancellous bone visible. The fracture is likely due to taphonomic weathering. The left digit IV phalanx has some bone loss anterior on ASMC4, with cancellous bone visible. Both elements have an anterior pit with a porous surface proximal to AAF (Right: (~16 mm med-lat, ~7.8-11.6 mm prox-dist, and ~5.8 mm deep), Left: (~12.2 mm med-lat, ~8.3-13.7 mm prox-dist, and ~4.8 mm deep)). Pores are better preserved on the right due largely to weathering on left, all pores being mostly circular on both elements, but differing sizes from 3 mm to <1 mm.

Fig. 23 Distal view of ETMNH 601 (*Teleoceras aepysoma* from Gray Fossil Site, Washington Co., Tennessee) digit III proximal phalanx. Note the porous osteolytic pits anterior to the articular surface, indicated by arrows

On ETMNH 609, the right digit II proximal phalanx has shallow bone loss on the anterior of ASMP2, with a few subsurface pits visible, also present on the left digit II phalanx. The left digit II phalanx also has defects to the lateral posterior edge of ASMC2, most probably being taphonomic. The lateral lobe of the ASMP2 has additional bone loss to the left phalanx (~2.8 mm across). The right digit III proximal phalanx of ETMNH 609 has similar bone loss cavities to that of ETMNH 601, with a larger cavity under AAF (~8.5 mm med-lat, ~4.7 mm ant-post, ~4.1 mm deep), and a smaller cavity between the AAF and medial rugosity (~9.9 mm med-lat, ~4 mm ant-post, and 0.7 mm deep). A similar, much less developed, cavity is medial on the left digit III phalanx (~9.9 mm, ~4.1 mm, and ~1.5 mm deep). The anterior of ASMC4 on both right and left digit IV phalanges of ETMNH 609 appears to have been weathered postmortem, with

the bone loss on the right being broad and superficial (~1.5 mm med-lat) while the left's is focused on the medial side and deeper (~6.7 mm across, and ~0.8 mm deep). The AAF absent on left element due to postmortem breakage/weathering.

ETMNH 769 consists of a partial 'left' half, making ID difficult, but it is likely the lateral portion of the left digit IV proximal phalanx. The anterior proximal articular surface has been exposed to taphonomic weathering.

ETMNH 3755 has notable postmortem breakage to the anterior of the left digit IV proximal phalanx, especially distally including parts of the ASMP4. The proximal surface has a dish shaped anterior edge, and some probable osteolysis of the posterolateral ASMC4. A small fold/erosive incision is visible in the posterior of ASMP4 between the lobes (~4.2 mm ant-post), probable arthritic indicator.

On ETMNH 8271, the right digit II proximal phalanx has probable CAT2 lipping on ASMC2, evidenced by visible shelf marking for surface boundary. The ASMC2 has increased porosity anterolaterally and posterolaterally adjacent to its edge, as well as small taphonomic fractures on the posterolateral surface. The left digit III proximal phalanx has taphonomic weathering/bone loss anterior to the ASMC3, as well as bone loss on the anterior surface of the bone, including a broad, porous depression proximal to the AAF (~10.6 mm med-lat, ~2.2 mm prox-dist, and ~1.9 mm deep). The posterior ASMP3 is eroded with adjacent perforations (scar: ~18.5 mm med-lat, ~4.2 mm prox-dist, and ~2.5 mm deep). Both digit IV proximal phalanges have CAT2 lipping around the ASMC4. An anterior pit with porous texture proximal to the AAF is observed on the digit IV proximal phalanges, as on ETMNH 601. Right: (~10.3 mm med-lat, ~10.5 mm prox-dist, and ~4.7 mm deep), Left: (~10.9 mm med-lat, ~2.87-9.1 mm prox-dist, and

~3.9 mm deep). CAT2 lipping on both ASMP4s' medial edge. Large bone loss pits (~1.5-2.4 mm diameter) adjacent to medial edge of ASMP4.

ETMNH 17357 is a probable left digit IV proximal phalanx with probable CAT2 lipping on the ASMC4, the diagnostic shelf difficult to distinguish. Osteolysis is observed on the lateral anterior surface (~24.7 mm med-lat, ~9.2 mm prox-dist, and ~5 mm deep, widening prox-dist laterally). The lateral AAF has postmortem fractures and weathering on the anteromedial ASMP4.

On ETMNH 32999, the left digit II proximal phalanx was broken into 3 large fragments postmortem, having since been reassembled. The epiphyseal boundary/growth plates are visible.

The identification of UTK 2.02 is uncertain, being either a right digit II or left digit IV proximal phalanx. It has smooth rugosities and a lip covered in concretion on the right (lateral/medial) of the distal articular surface (~6.6 mm ant-post, ~4.5 mm prox-dist, and ~1 mm med-lat).

The identification of UTK 14.xx is similarly uncertain as UTK 2.02, being either a right digit II or left digit IV proximal phalanx. The anterior of the bone has a shelf (raised ~3 mm) and taphonomic weathering/bone loss on the proximal articular surface. Proximal to the AAF is a bone loss cavity (~15.7 mm med-lat, ~10.5 mm prox-dist, and ~5.4 mm deep), as well as a depression between the AAF and distal articular surface, noting the in-life separation of the interphalangeal and sesamoid articular cartilage (~10 mm, ~5.2 mm ant-post, and ~0.7 mm). Tactile observation indicates the probable presence of CAT1 lipping on lateral/medial edge of distal articular surface.

UTK 15.xx is a left digit III proximal phalanx with CAT2 anterior lipping on proximal articular surface, and bone loss surrounding the AAF (~4.1 mm separation/'neck'). Additionally,

distinct cavities are observed laterally and medially (~6.9 mm med-lat, ~4.9 mm prox-dist, and ~2.9 mm deep) and (~13 mm med-lat, ~6.3 mm prox-dist, and ~3.5 mm deep).

Medial Phalanges

Included specimens: ETMNH 564, 601, 609, 769, 8271, 32999.

The isolated partial phalanx of ETMNH 564 is either a right digit II or left digit IV phalanx, though its incompleteness makes ID uncertain. It has postmortem breakage on the left side of the bone, and osteolysis across the preserved anterior surface (~4.2-6.3 mm prox-dist, ~2-4 mm deep).

On ETMNH 601, the right digit II medial phalanx has bone loss and perforations on the proximal anterior surface (~21 mm med-lat, ~3.1-5mm prox-dist, and ~1.4mm deep). The posterior of ASPP2 has an upturned lip/spur, between the lobes of the pad (~4.4 mm med-lat, ~1.6 mm ant-post, and <1 mm deep). Early CAT2 lipping is observed posterolaterally on the ASPP2, with a visible shelf present. Additionally, the pad of the ASPP2 has an indistinct medial edge. Notable bone loss and perforations are present posterolaterally between ASDP2 and the rugosity (~11.6 mm ant-post, ~9.5 mm prox-dist, and ~1.8 mm deep). The center of ASDP2 has a small, odd divot (~2.7mm ant-post, ~1.5mm med-lat) with 2 small striations near the posterior edge of the surface between the two lobes (~1.5 mm ant-post). The left digit II medial phalanx has similar but less dramatic anterior bone loss and porous texturing on the proximal anterior surface (~1.7-3 mm prox-dist, ~1 mm deep). The ASPP2 has CAT2 lateral and posterior lipping as well as a spur/upturned lip on the posteriorly between lobes (~4.1 mm med-lat, ~1.7 mm ant-post). The lateral surface has perforations proximally and distally adjacent to the rugosity, and a bone loss cavity distal to the rugosity (~7.5 mm prox-dist, ~16 mm ant-post, and 2.3 mm deep). The ASDP2 has one small striation (~2.2 mm ant-post) on its posterior. The right digit III medial

phalanx of ETMNH 601 has osteolytic cavities and porous surfaces on the lateral (~9.3 mm med-lat, ~7.7 mm prox-dist, and ~3.2 mm deep) and medial (~8.8 mm med-lat, ~5.8 mm prox-dist, and ~2.4 mm deep) sides of the distal AAF. These extend proximally into the lateral and medial rugosities (~8.7 mm and ~6.5 mm, respectively) and extend to the entire lateral and medial sides. Osteolysis is observed around a posterior nutritive foramen on the right digit III medial phalanx. On the left digit III medial phalanx, the proximal AAF is severely reduced with a bone loss cavity distally adjacent. Also, the left digit III medial phalanx has less extensive bone loss around the distal AFF (lateral - ~7.9 mm prox-dist, ~4.9 mm med-lat, and ~2.3 mm deep; medial - ~4.3 mm prox-dist, ~2.5 mm med-lat, and ~1.4 mm deep). The right digit IV medial phalanx of ETMNH 601 has limited proximal anterolateral and distal posterolateral bone loss of the rugosity (non-focal, dispersed within an area ~8.7 mm across), with more significant bone loss on the distal posteromedial rugosity (~10.6 mm ant-post, ~4.7 mm prox-dist, and ~2.6 mm deep). The left digit IV medial phalanx has taphonomic weathering to its anterolateral portion. Otherwise, irregularities are mirrored from the right phalanx, with the medial cavity being greater on the left (posteromedial cavity - ~10.64 mm across, and ~2.4 mm deep) with adjacent postmortem breakage to the posteromedial ASDP4.

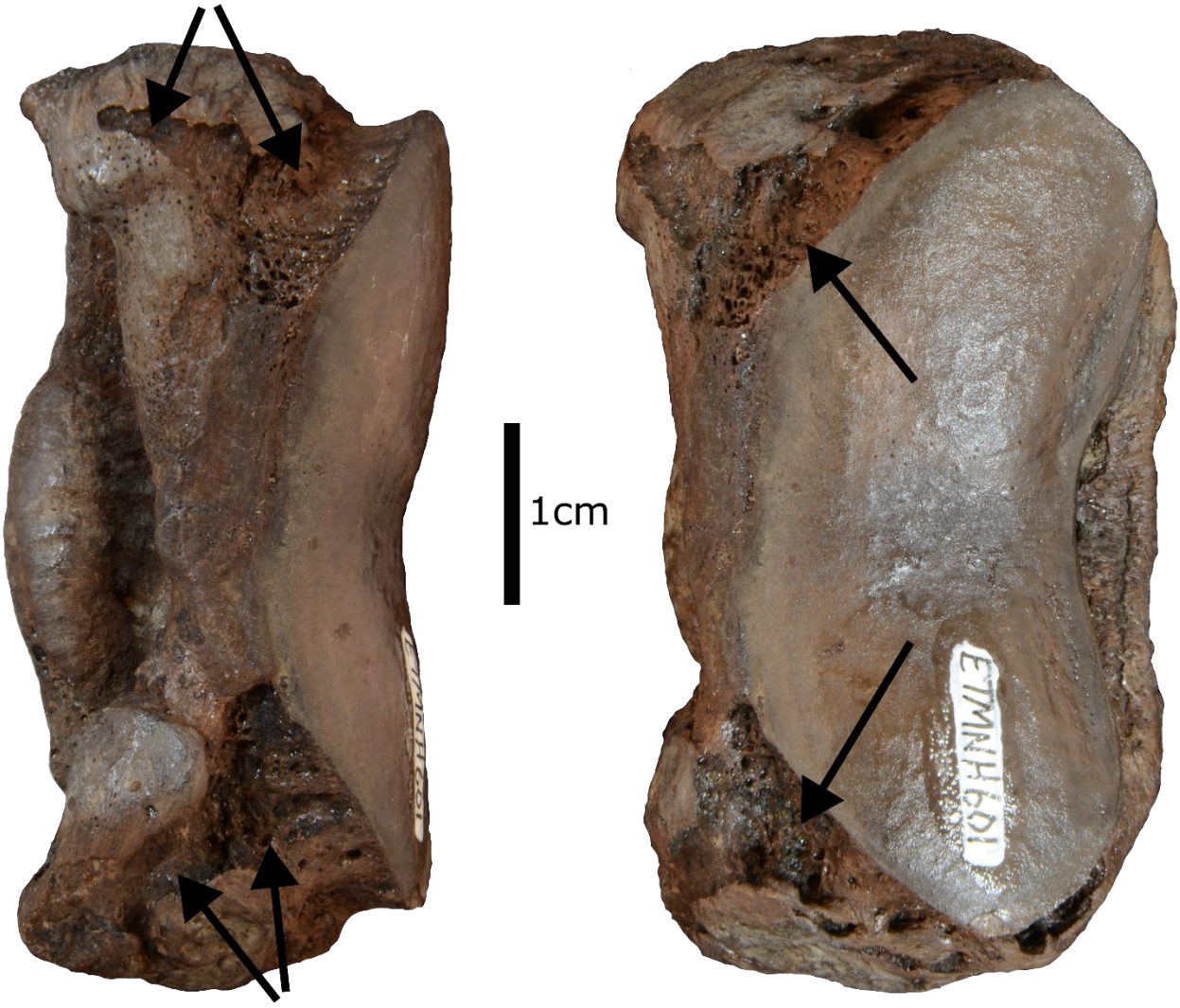

Fig. 24 Left digit III medial phalanx of ETMNH 601 (*Teleoceras aepysoma* from Gray Fossil Site, Washington Co., Tennessee) in anterior (left) and distal (right) view. Note osteolysis around the articular surface, denoted by arrows, but not affecting the articular surface itself

On ETMNH 609, the right digit II medial phalanx has an eroded rugosity on the proximomedial anterior surface (~18.3 mm, ~2.6-6.8 mm, and ~1.2 mm), with there also being some bone loss on the medial rugosity (~7 mm ant-post and ~4.2 mm prox-dist). The left digit II medial phalanx has similar anterior bone loss (~17.2 mm med-lat, ~2.5-3.6 mm prox-dist, and ~1.4 mm deep) to the right element, and lateral bone loss of ASDP2 and the adjacent rugosity (~7.1 mm ant-post and ~12.9 mm prox-dist). The right digit III medial phalanx of ETMNH 609

has some bone loss across anterior surface between ASDP3 and the anteroproximal rugosity, as well as bone loss and postmortem breakage/weathering to the medial rugosity (~8 mm ant-post, ~6.2 mm prox-dist, and ~3 mm deep), and a bone loss cavity on the posterior lateral surface (~8.4 mm ant-post, ~10.6 mm prox-dist, and ~1.7 mm deep). The left digit III medial phalanx has the same/similar irregularities, except the bone loss extends anteriorly similar to the condition of ETMNH 601's right digit III phalanx. Measurements: anteromedial cavity (~4.8 mm across, and ~1 mm deep), posteromedial (~7.5 mm across, and ~3 mm deep), anterolateral (~3.2 mm wide, ~9.5 mm prox-dist, and ~1 mm deep), and posterolateral (~6.5 mm ant-post, ~9.4 mm prox-dist, and ~2.5 mm deep). The right digit IV medial phalanx of ETMNH 609 has a bone loss cavity on the posterior medial surface (~6.5 mm ant-post, ~8.7 mm prox-dist, and ~1.3 mm deep), and a rounded spur on the posterolateral ASDP4. The left digit IV medial phalanx has a bone loss cavity in same place as on right (~6.5 mm ant-post, ~6.2 mm prox-dist, and ~1.3 mm deep).

On ETMNH 8271, the right digit II phalanx of ETMNH 8271 has bone loss on the medial anterior surface (~21.4 mm med-lat, ~6.4-6.9 mm prox-dist, and ~0.9 mm deep). The right digit III medial phalanx of ETMNH 8271 was broken postmortem, with the lateral third broken off, but was reassembled in lab prep. The anterior surface has some osteolysis, with exaggerated perforation proximally adjacent to the AAF and larger patch, more medially located, adjacent to the ASPP4 (~18.7 mm med-lat, ~6.2 mm prox-dist, and ~0.6 mm deep). The lateral and medial anterior surface have bone loss, with the medial extent potentially also modified by taphonomic weathering (~10 mm med-lat, ~3.8 mm prox-dist, and ~2.8 mm deep; ~10 mm med-lat, ~3.3 mm prox-dist, and ~1-2.5 mm deep). The ASPP3 has perforations and bone loss on its posterior (~17.9 mm med-lat, ~2.4 mm prox-dist, and ~1.2 mm deep), and posterior bone loss of rugosities

on lateral and medial surfaces (~6.7 mm across and ~1.5 mm deep; ~6.6 mm across and ~2.1 mm deep). The left digit III medial phalanx has some bone loss between ASPP3 and the proximal anterior rugosity (~1.18 mm ant-post). The ASPP3 has porous surfaces posterior to it, and the AAF has proximal bone loss (~1.7-2.6 mm prox-dist). The lateral and medial rugosities have similar posterior bone loss, but this osteolysis is less distinct (~6.8 mm across, ~2.5 mm and ~2.8 mm deep). The ASDP3 has an anterior medial defect, likely a combination of postmortem breakage and preparation (~7.9 mm wide and ~4.2 mm deep). Left digit IV medial phalanx of ETMNH 8271 has anterior lateral bone loss adjacent to ASPP4, along with similar irregularities to other specimens (ETMNH 601 and ETMNH 609). The phalanx has distal posterior bone loss of the medial and lateral surface rugosities (~8.1 mm ant-post, ~7.4 mm prox-dist, and ~1.4 mm deep) and (~8 mm ant-post, ~4.9 mm prox-dist, and ~0.9 mm deep), as well as lateral bone loss cuting into ASDP4 (~5.4 mm wide and ~1.7 mm deep into the surface laterally) in a semi-circular shape.

The left digit III medial phalanx of ETMNH 32999 has taphonomic weathering across all surfaces.

Distal Phalanges

Included specimens: ETMNH 601, 609, 743, 5233, 8271, 19280, 32999.

The right digit III distal phalanx of ETMNH 601 has anterior bone loss on ASMP3 (~14.85 mm med-lat, ~2.82 mm ant-post, and ~1.37 mm deep). The distal phalanx has a modified/oversized anterodistal nutritive foramen (~13.7 mm front-back, and ~9.66 mm med-lat), with internal pitting (between ~1-<1 mm). The left digit III distal phalanx has anterior bone loss of the ASMP3, as on right (~17.06 mm med-lat, ~2.15 mm ant-post, and ~1 mm deep). The

left distal phalanx has a potential modified anterodistal foramen similar to the right phalanx, though it is difficult to ascertain due to inherent modified/irregular nature of distal phalanges.

On ETMNH 609, the right digit II distal phalanx has a small patch of bone loss on posterior ASMP2 (~2.2 mm med-lat and ~1.45 mm ant-post). The right digit III distal phalanx has general weathering and medial postmortem breakage. The left digit III distal phalanx has a potential band of bone loss across anterior ASMP3 (~1.25 mm ant-post).

ETMNH 743 consists of a partial left portion of an unidentified phalanx, with part of the articular surface preserved.

ETMNH 5233 is a partial central portion, with most of the central articular surface preserved (potentially a digit III phalanx). It possesses large internal cavities laterally and medially anterior to articular surface.

On ETMNH 8271, the right digit II distal phalanx (inferred as manual due to large size compared to digit III phalanx) has increased anterior perforation. It was broken into three roughly equal sized fragments postmortem, which have since been reassembled. The right digit III distal phalanx is highly vascularized distally, likely the result of nerves and nutritive blood vessels for the hoof (Short 2013; Short et al. 2019). The left is similar to the right, but also suffers from taphonomic weathering, especially distally and laterally. The right digit IV distal phalanx is broken similarly to the digit II distal phalanx, though the equivalent third lateral fragment is missing. As with the digit II distal phalanx, the right digit IV distal phalanx has since been reassembled.

On ETMNH 32999, the right digit II distal phalanx was weathered postmortem. The right digit III distal phalanx is partial with only central portion preserved; it has been heavily

weathered postmortem. The right digit IV distal phalanx has taphonomic weathering and the lateral portion missing past ASMP4.

Manual Sesamoids

Included specimens: ETMNH 601, 609, 4381, 8271, 12175, 12776, 12777, 13968, 20825, 21302, 31001, 32999, 38000.

Sesamoids have been identified from 12 different specimens. They range in preservation from being all present and in good condition, as in ETMNH 601 and ETMNH 609, to heavily weathered isolated elements such as ETMNH 31001. Most of the specimens consist only of metacarpal sesamoids, though some phalangeal sesamoids have been recovered (ETMNH 601: left digit III, ETMNH 609: both digit III, ETMNH 4381: digit III, ETMNH 8271: digit III and digit II/IV, ETMNH 12776: digit III, ETMNH 12777: digit III, ETMNH 13968: digit II/IV, and ETMNH 20825: digit II/IV). These are small variable bones, with limited degree of uniformity, to the point that distinguishing whether they are manual or pedal can be difficult (Short et al. 2019).

On ETMNH 601, the right medial MC2 sesamoid has developed an accessory lateral articular facet, as part of CAT2 lipping on the proximolateral side. Some small postmortem fractures are present on the distolateral portion. The right lateral MC2 sesamoid has a larger accessory facet on mediodistal portion than the right (~5.3 mm ant-post and ~7 mm prox-dist). The right MC4 sesamoids have accessory distal facet on lateral sesamoid, probably also present on medial but taphonomic breakage obscures this. Both have accessory medial/lateral facets facing each other. The left MC2 sesamoids of ETMNH 601 have accessory distal articular facets. The left MC3 sesamoids have enlarged foramina, like on the right, but more eroded. The left MC3 sesamoids have more extensive osteolysis dorsally and ventrally adjacent to ASMC3 (Fig.

25). This osteolysis extends laterally on the medial sesamoid and medially on the lateral sesamoid. The lateral MC3 sesamoid displays a deep, tear-shaped cavity on the medial surface (Fig. 25), with a channel also present on the posterolateral surface (Fig. 25; length: ~15.5 mm, width: ~1.6 mm, and depth: ~1.2 mm). The left MC4 medial and lateral sesamoids have accessory articular facets laterally and medially to their ASMC4, respectively. Lateral MC4 sesamoid has dorsal bone loss on and adjacent to ASMC4.

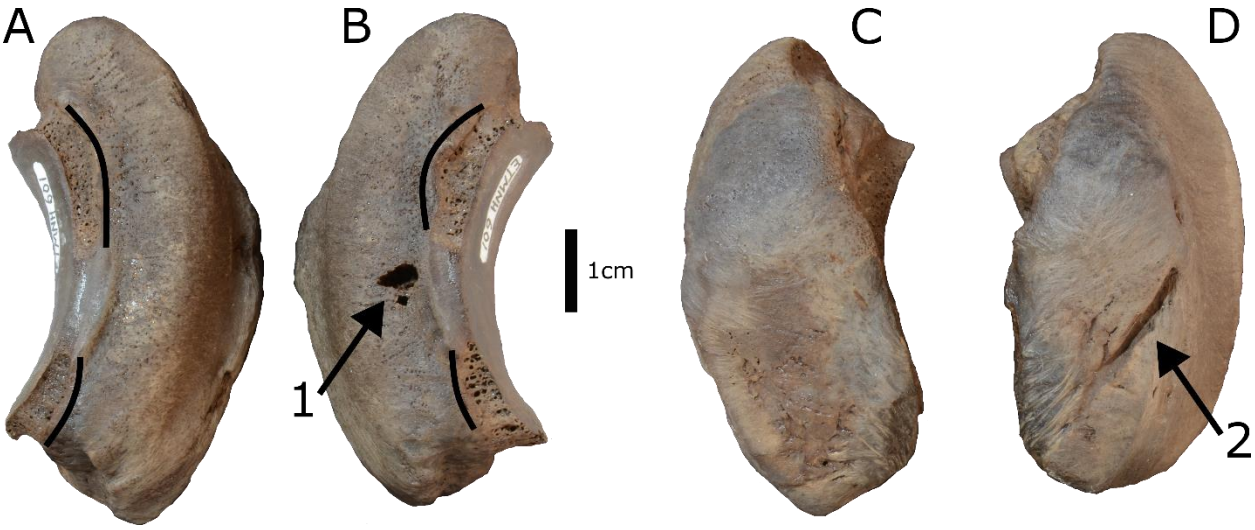

Fig. 25 Left metacarpal 3 (MC3) sesamoids of ETMNH 601 (*Teleoceras aepysoma* from Gray Fossil Site, Washington Co., Tennessee). Note abnormal cavity (**1**), channel (**2**), and osteolysis along the edge of the articular surfaces (emphasized by lines). **A**) medial MC3 sesamoid in lateral view, **B**) lateral MC3 sesamoid in medial view, **C**) medial sesamoid in posterior view, and **D**) lateral sesamoid in lateral view

On ETMNH 609, the right medial MC3 sesamoid has an irregular, enlarged medial cavity next to a foramen and appears to be partially filled in with epoxy from reconstruction (~6.8 mm, ~11.3 mm, and ~3.1 mm deep). The right digit III phalangeal/distal sesamoid has a shallow channel with pitting/foramina distal to the articular surface (~2.8-4 mm wide). The left medial MC3 sesamoid of ETMNH 609 has an enlarged/modified foramina cavity. Its condition is more

regular than on the right. The left digit III phalangeal/distal sesamoid has similar osteolysis to the right, along with an indentation on the central portion of ventral articular surface.

ETMNH 4381, an assumed digit III phalangeal/distal sesamoid based on shape, has a broad osteolytic surface covering most of the surface posteroventral to the label.

On ETMNH 8271, the right medial and lateral MC3 sesamoids have enlarged lateral and medial foramina cavities, respectively. The medial sesamoid's cavity is more dorsoventrally elongate (kidney bean-shaped), while the lateral sesamoid's more circular. The right lateral MC4 sesamoid has an accessory articular facet ventral to ASMC4. The left medial MC3 sesamoid continues the trend of enlarged lateral foramina cavity, though it is more circular on this sesamoid than on the other medial sesamoids. An uncertain right digit IV/left digit II phalangeal/distal sesamoid associated with ETMNH 8271 displays lateral/medial bone loss.

The left medial MC2 sesamoid of ETMNH 12175 has osteolysis ventrolateral (~12 mm med-lat, ~3.2 mm ant-post, and ~0.9 mm deep) and dorsomedial (~9.3 mm dors-vent, ~4.3 mm ant-post, and ~0.7 mm deep) to ASMC2.

On ETMNH 12776, a digit III phalangeal/distal sesamoid has a long osteolysis surface dorsal (in reference to label) to articular surface. Uncertain whether it is a left or right element.

On ETMNH 12777, a digit III phalangeal/distal sesamoid has a mixed osteolysis and taphonomic weathered surface in the same place as on ETMNH 12776. Uncertain whether it is a left or right element.

An uncertain digit II/IV phalangeal/distal sesamoid, associated with ETMNH 13968, has medial/lateral and ventral (in reference to label) osteolysis adjacent to the articular surface.

A phalangeal/distal sesamoid, inferred to be digit II, from ETMNH 20825 has deep osteolysis anteriorly (in reference to label) adjacent to the articular surface, with some of said surface having been dorsally eroded.

ETMNH 31001 is a significantly weathered sesamoid, with little of the original surface remaining.

On ETMNH 32999, the right medial and lateral MC3 sesamoids are missing/have reduced medial and lateral foramina, respectively. In addition, both have taphonomic weathering in those areas. The medial sesamoid has posterodorsal taphonomic weathering with the lateral sesamoid having anteroventral postmortem breakage and weathering.

An unidentified MC2/MC4 sesamoid from ETMNH 38000 has anterior taphonomic weathering.

Hindlimbs

Innominate

Included specimens: ETMNH 601, 609.

The innominate bones preserved from GFS belong to ETMNH 601 and ETMNH 609. Both specimens are partial with limited reconstruction/reassembly. Both show some degree of in life modification, though interestingly the younger ETMNH 609 shows more than the elder ETMNH 601.

Both innominate bones from ETMNH 601 are broken with reassembly limited to the wing of the ilium and acetabula. The left innominate bone's acetabulum has a cavity in its anteroventral corner which is rectangular with blunted corners, raised perimeter, and shallower extension anteroventrally (~11.85-15.21 mm at longest, ~7.21 mm at widest/second longest point, and ~3.2 mm deep).

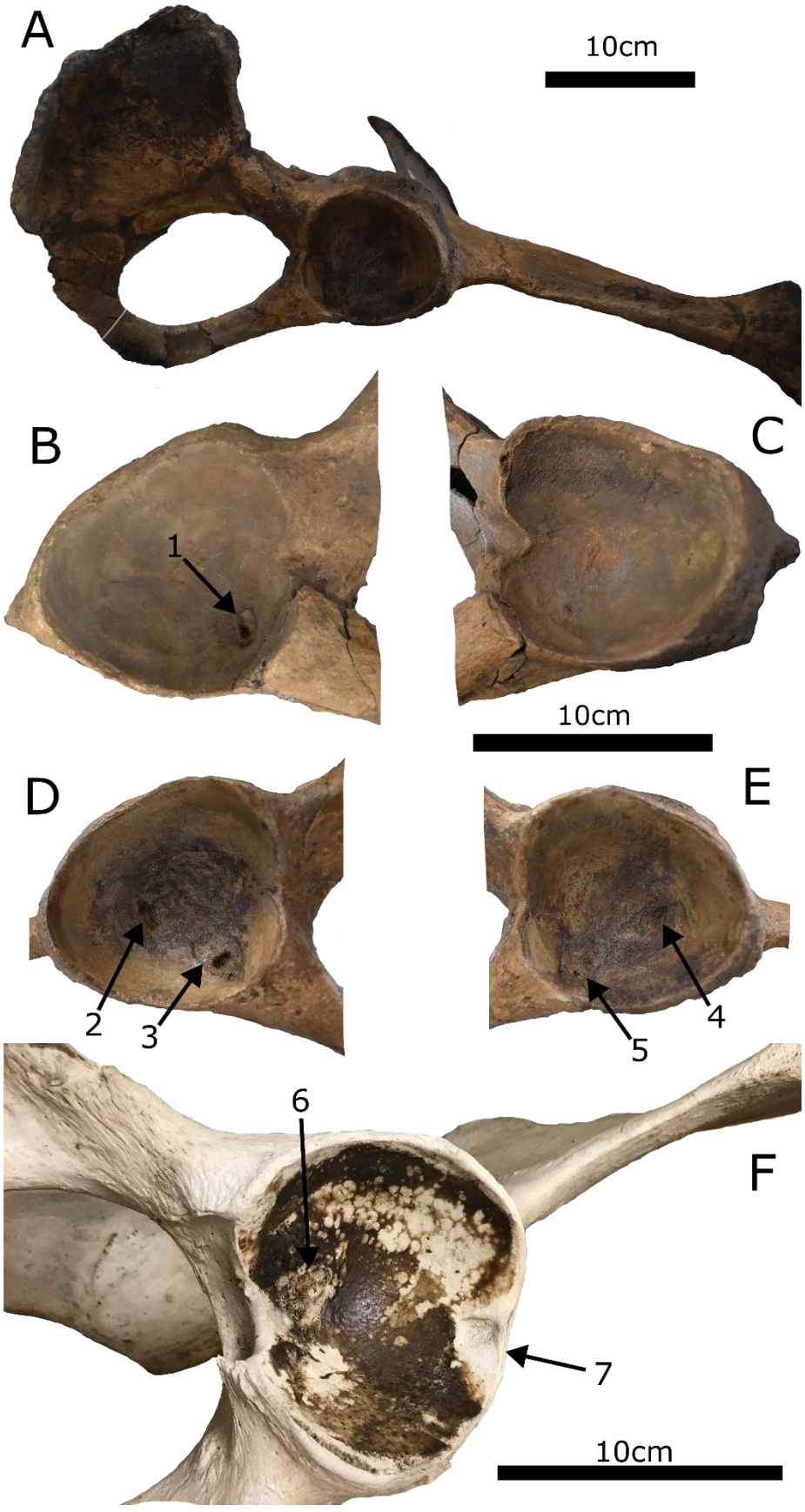
A
10cm
B
1
C
10cm
D
2
3
E
4
5
6
F
7
10cm

Fig. 26 Fossil and Modern Innominate bones. ETMNH 601 and ETMNH 609 (*Teleoceras aepysoma* from Gray Fossil Site, Washington Co., Tennessee). **A**) full view of 609's right innominate in ventral view for reference. (**B-E**) close-ups of the acetabula from ETMNH 601 (**B** and **C**) and ETMNH 609 (**D** and **E**). **B**) with the irregular/pathologic pits (**1**). **D**) showing the left acetabulum of ETMNH 609 with irregular/pathologic pit (**2**) and avulsed region (**3**). **E**) showing the right acetabulum of ETMNH 609 with counterpart to **D**'s pit (**4**). **F**) showing the left acetabulum of ETMNH-Z 7216 (*Rhinoceros unicornis* from Buffalo Zoo) in ventral view. **5**) a shallow depression consistent with the insertion point of the ligamentum teres. **6**) a depression of unknown origin, this depression is also mirrored on the right acetabulum

Both innominate bones from ETMNH 609 are partial and have been reconstructed. The right innominate has a cavity dorsal of the center of the acetabulum (~13.46 mm anteroventral-posterodorsal, ~8.31 mm anterodorsal-posteroventral, and ~4.71 mm deep), as well as a series of three irregularly shaped pits/avulsions around exposed cancellous bone at the anteroventral corner (the theoretical insertion point of ligamentum teres; due to curved internal surface of acetabulum measurements (especially depth) may not be 100% precise; left main pit (~3.64 mm across, ~3 mm deep), left antipodal pit (~4.82 mm long, ~2.07 mm wide, ~2 mm deep); right pit (~4.58 mm long, ~2.81 mm wide, ~2 mm deep)). Shallow trenches/scars dragging anteriorly and becoming shallower from the 3 pits. Cancellous bone patch which is rectangular with blunted corners (~16 mm ant-post, ~14.54 mm dors-vent). The left innominate has 2 large cavities/avulsions, one on the anteroventral corner (~8.5 mm anteroventral-posterodorsal, ~6 mm anterodorsal-posteroventral, ~5.7 mm deep), surrounded by healed/accessory bone (similar to that of the three pits on the right innominate, ~14.4 mm anteroventral-posterodorsal, ~20.8 mm anterodorsal-posteroventral), and just dorsal of the center of the acetabulum (~6.79 mm

anteroventral-posterodorsal, ~14.25 mm anterodorsal-posteroventral, and ~6.15 mm deep). Bone surface posterior to and posteroventral to second cavity is rugose/eroded.

Femur

Included specimens: ETMNH 601, 609, 3721, 33000.

Femora from five specimens have been recovered, with ETMNH 601, ETMNH 609, and ETMNH 33000 being paired elements, and ETMNH 3721 being an isolated right element. All are broken to some degree, with ETMNH 601 and ETMNH 609 being nearly complete and reassembled. ETMNH 33000 is less complete, with the right missing some small fragments and left missing more including most of the lateral side of the head, but they have also been reassembled, while ETMNH 3721 is the least complete with what fragments are present have yet to be reassembled, with the diaphysis mostly complete and the distal epiphysis in three large fragments, with some still having cemented matrix on them. ETMNH 601, ETMNH 609, and ETMNH 33000 represent mature individuals, as evidenced by fused epiphyseal plates (Short 2013; Short et al. 2019), while the unfused epiphyseal plates suggest ETMNH 3721 comes from a juvenile.

The right femur of ETMNH 601 is broken and has been reassembled. The posterior of the MEc has a roughly triangle-shaped cavity, with the apex pointing proximally, which widens and deepens distally (Fig. 27; ~20.78 mm prox-dist, ~13 mm med-lat at widest point, and ~3.77 mm deep at deepest point). The cavity is surrounded by fibrous looking bone, probably muscle scarring. The left femur has a raised rugosity in same place (Fig. 27), which appears similar.

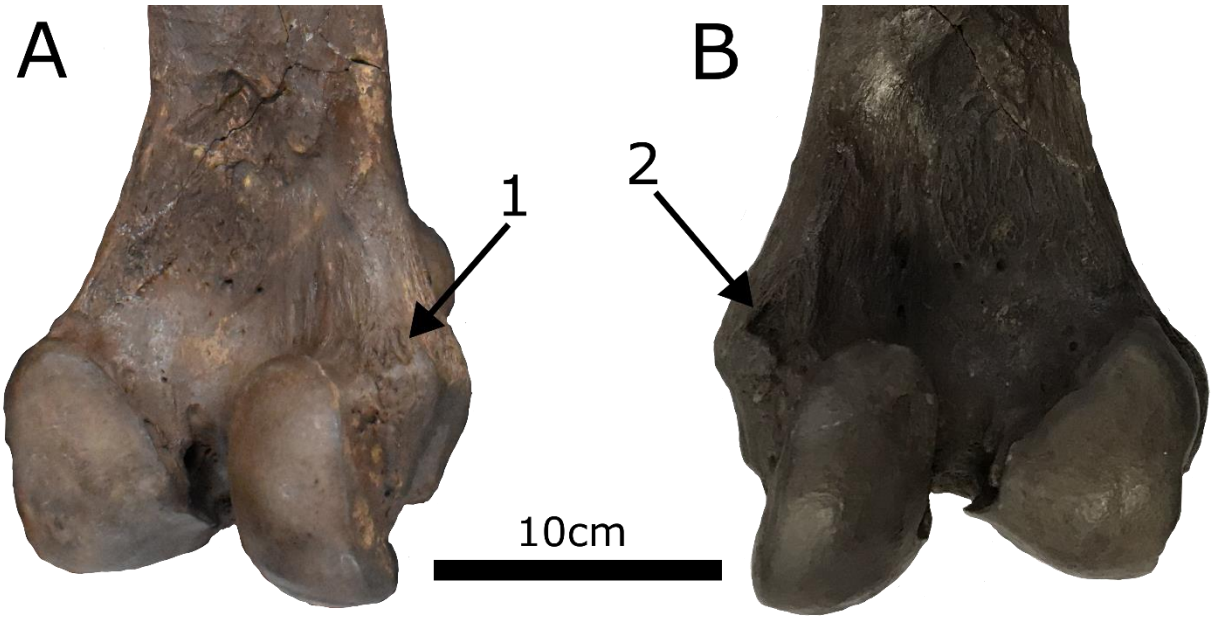

Fig. 27 Distal femora of ETMNH 601 (*Teleoceras aepysoma* from Gray Fossil Site, Washington Co., Tennessee) in posterior view. **A**) left femur with arrow indicating muscle scarring on the posterior of the medial epicondyle (MEc) (**1**). **B**) right femur with arrow indicating the cavity on the MEc (**2**)

The right and left femora of ETMNH 33000 with MEc cavities similar to the right femur of ETMNH 601, though the right appears more rectangular and more healed (~23.45 mm prox-dist, ~8.37 mm med-dist, and ~2.82 mm deep), and the left is somewhat obscured by taphonomic weathering but looks to share more with its right counterpart than ETMNH 601. (~13.68 mm prox-dist. ~8.24 mm med-lat, and ~2.27 mm deep)

Patella

Included specimens: ETMNH 601, 609, 33000.

Patellae are represented from the three most complete specimens, ETMNH 601, ETMNH 609, and ETMNH 33000, with all three preserving both elements. Half of the patellae are in good condition, with the right of ETMNH 601 and both patellae of ETMNH 33000 being broken. All three have been reassembled, though the right of ETMNH 33000 is missing large

chunks of the articular surface. Only ETMNH 33000 shows any degree of notable lipping, not unexpected of the oldest of the complete specimens. ETMNH 33000 was uncovered after the publication of the 2019 species description, and so has not been given a definitive age range. Despite this, based on relative tooth wear and bone modification, it is evident that it is older than either ETMNH 609 or ETMNH 601.

ETMNH 33000 has notable lipping on its left patella, consistent with age. There is CAT2 lipping, with diagnostic shelf, around most of the articular surface, as well as some rounded osteophytes on the lateral portion of the base and apex (sensu. Short et al. 2019).

Tibia and Fibula

Included specimens: ETMNH 601, 609, 1902 (on exhibit), 8271, 19280, 28800, 31305, 33000.

Due to the tibiae and fibulae being fused in even "middle-aged" adult specimens of *T. aepysoma* from GFS, these bones will be discussed together here. Eight specimens from GFS preserve tibia and fibula material, though only four of these specimens preserve more than a proximal or distal fragment. All were broken to some degree (Short 2013; Short et al. 2019), but ETMNH 601, ETMNH 609, ETMNH 1902, and ETMNH 33000 have been almost completely reassembled. The left elements of ETMNH 601, ETMNH 609, and ETMNH 33000 show a greater degree of weathering than their right counterparts, a continuing pattern mentioned previously on other elements of the type specimens (Short 2013; Short et al. 2019). Three specimens display proximal fusion between the tibia and fibula: ETMNH 601, ETMNH 19280, and ETMNH 33000. On ETMNH 601, a bone fragment was cemented during taphonomy via matrix on the right tibia posterolaterally on the middle diaphysis. Only the part of proximal ends of the tibia and fibula were recovered from ETMNH 19280, which are fused proximally, as

stated above. The tibia has notable lipping on the articular surface for femur (ASF). The right tibia and fibula of ETMNH 33000 shows margin lipping on their distal articular surfaces, erring towards CAT2 on the medial and lateral sides of the tibia and fibula, respectively. Similar marginal lipping is not observed on the left elements due to weathering.

Tarsals

Calcaneum

Included specimens: ETMNH 601, 609, 33000.

The calcaneum sample from GFS includes elements from three specimens: ETMNH 601, ETMNH 609, and ETMNH 33000. All three specimens preserve both elements. All are in good condition, with only ETMNH 601 and ETMNH 33000's left calcanei needing reassembly. The left of ETMNH 601 was recovered broken into multiple fragments, while the left of ETMNH 33000 was only broken in half at the CTb. Both were reassembled. On ETMNH 609, the right and left elements show differential weathering, with the latter showing more as elsewhere in the skeleton.

In ETMNH 601, a folded bone/split was propagating laterally between the anterior and posterior portions of the ASA2 on the right calcaneum (~18.39 mm med-lat and as wide as ~1.54mm ant-post). As mentioned earlier, the left calcaneum was broken but has since been reassembled, though a few small fragments are still missing. The left calcaneum's ASA2 displays potential lateral and medial precursor folds/incisions (lateral: ~4.41 mm med-lat and ~1.21 mm ant-post, medial: ~8.89 mm med-lat and ~1.34 mm ant-post), with the medial one extending off the articular facet for at least half the measured length.

The right calcaneum of ETMNH 609 has a mediolateral pinch/incision centrally on the ASA2 (~9.15 mm med-lat, ~1.46 mm ant-post medial and ~1.74 mm ant-post lateral). The left

calcaneum's ASA2 has a medial incision contained entirely within the bounds of the articular surface (~9.64 mm med-lat, and ~0.89 mm ant-post).

ETMNH 33000 has the fewest traces of mediolateral incision on the ASA2. The right calcaneum has barely visible bone creases. The left calcaneum has some limited bone loss of posterior medial ASA2, potentially postmortem (~3.16 mm med-lat, ~2.32 mm ant-post). The right calcaneum has superficial bone loss on the dorsolateral ASCb (~14.25 mm med-lat, ~9.39 mm dors-vent), and some deeper bone loss on the ventromedial portion (~5.27 mm med-lat, ~4 mm dors-vent, and ~0.71 mm deep). The medial portion of anterior process (AP) is eroded/partially hollowed-out (~21.2 mm ant-post, ~10.96 mm dors-vent, and ~4.51 mm deep). The right has postmortem breakage/removal of cortical bone of the dorsolateral CTb. The main defect on the CTb is roughly triangular with a posterior apex (~17.29 mm ant-post, ~12.93-20.73 mm, and ~1.51 mm deep), and the secondary, more superficial portion is medial (~6.21 mm ant-post, ~11.96 mm med-lat). The ASCb has irregular dorsolateral bone loss reminiscent of what is seen on the right (rough extent: ~9.62 mm med-lat, and ~13.94 mm dors-vent).

Astragalus

Included specimens: ETMNH 601, 609, 1901, 6647, 14175, 21073, 33000.

Astragali are represented by elements from seven different specimens, with only ETMNH 601 and ETMNH 609 being recovered with both elements. ETMNH 14175 and ETMNH 33000 preserve right astragali, while ETMNH 1901, ETMNH 6647, and ETMNH 21073 preserve lefts. All are in generally good condition except for some taphonomic weathering, with ETMNH 1901 showing the greatest degree of this, and a small amount of reassembly to the astragalus of ETMNH 601.

On ETMNH 601, the ventral portion of the right astragalus's DR, between the ASCb and ASN, is slightly depressed (~17.02 mm ant-post, ~0.96 mm deep), though any other modifications are uncertain/obscured due to leftovers from matrix removal during prep on the ASN. The left has a roughly circular pit (~4.03 mm med-lat, ~5.48 mm ant-post), likely a postmortem fracture, with exposed cancellous bone. The left astragalus has a small depression/incision medially to the DR pit on the ASN (~2.12 mm med-lat, ~4.16 mm ant-post). The ASN has a semi-circular bone loss cavity on the anterior (~7.08 mm med-lat, ~3.04 mm dors-vent, and ~1.84 mm deep), and the MASC has CAT2 lipping on its ventral edge.

On ETMNH 609, the central portion of the right astragalus's DR is depressed (posteriorly biased), with a pit/incision medially adjacent to/part of it (~10.88 mm ant-post, ~8 mm med-lat, and ~2.03-1.56 mm deep). Both features are present on the left as well (~8.03 mm ant-post, ~8.29 mm med-lat, and ~1.97-1.88 mm deep). These features on both bones have a porous texture, distinct from cancellous bone. Additionally, both elements have CAT2 lipping on the distal articular surface for the calcaneum.

On ETMNH 1901, the DR depression appears to have been present on the left astragalus at one point, though it is uncertain due to anterior taphonomic weathering.

The left astragalus's DR is sharper/more blade-like on ETMNH 6647 than ETMNH 601, with a small osteophyte on the anterior portion and some porous texturing medially adjacent to it, where the pit would be on ETMNH 609.

The condition of the right astragalus of ETMNH 14175 is similar to that of ETMNH 6647, with an additional miniscule notch and lacking the texturing seen on the other specimens.

ETMNH 21073 has an underdeveloped DR depression, relative to other specimens, on its' left astragalus (~1.57 mm ant-post).

The right astragalus of ETMNH 33000 is similarly unaffected as in ETMNH 601, though with some hints of porous texture potentially attributable to taphonomic weathering.

Navicular

Included specimens: ETMNH 601, 609, 33000.

The navicular has representatives from three specimens. Only ETMNH 33000 does not have both right and left elements, preserving only the right navicular. The naviculars are in generally good condition with only ETMNH 601 having to be reassembled (Short 2013; Short et al. 2019). ETMNH 609 shows differential weathering between the left and right elements with the right showing more weathering, in contrast to elsewhere in the skeleton. Of note, the posterior/palmar cavity formed by navicular, ectocuneiform, mesocuneiform, and entocuneiform is much larger in ETMNH 601 than ETMNH 609.

The right navicular of ETMNH 601 was broken postmortem on the medial process anteriorly, and the left was broken on posterior portion. Both have been reassembled. Both naviculars have an osteophyte between ASMe and ASCb2 (~2.43 mm and 3.02 mm high). The left entocuneiform has lateral bone loss on the ASMe (~15 mm ant-post, ~4 mm med-lat, and ~1.98 mm).

On ETMNH 609, the left navicular's articular surface for astragalus (ASA) has probable CAT2 marginal lipping on the anteromedial corner. The posterior ASMe and ASCb2 show evidence for CAT2 lipping in the form of shelves on the articular surfaces. The weathering on the right navicular of ETMNH 609 has obliterated any evidence for marginal lipping.

ETMNH 33000 has CAT1 marginal lipping around the medial edge of the ASA, as denoted by tactile lip. Small osteophytes present on lateral ASA edge adjacent to ASCb2. The

ASMe has CAT1 lipping on medial edge and an osteophyte on the posteromedial edge of ASCb2 (~6.6 mm med-lat, ~2.3 mm ant-post, and ~0.5 mm high).

Cuboid

Included specimens: ETMNH 601, 609, 33000.

As with the navicular, the cuboid has representatives from three specimens. Only ETMNH 33000 does not have both right and left elements, preserving only the right cuboid. All are in good condition with only the right cuboid of ETMNH 609 requiring some reassembly (Short 2013; Short et al. 2019).

On ETMNH 601, the ASA and articular surface for ectocuneiform 2 (ASE2) are connected on both cuboids. The left cuboid has porous bone anterior to ASMT3 and ASMT4, as well as an osteolytic cavity (~20.1 mm med-lat, ~7.29 mm prox-dist, and ~3.35 mm deep).

In ETMNH 609, both entocuneiforms' ASA and ASE2 are separated. The left cuboid has a small osteophyte centrally located on the dividing ridge of ASA and ASCL (~3.39 mm ant-post, ~1.67 mm med-lat, and ~0.71 mm high).

On ETMNH 33000, the ASA and ASE2 are connected on the right cuboid, as on ETMNH 601; and a row of small osteophytes and pits on same place as on the left cuboid of ETMNH 609 (row ~8.71 mm ant-post, osteophytes <1 mm).

Entocuneiform

Included specimens: ETMNH 601, 609.

Entocuneiforms are only represented by two specimens ETMNH 601 and ETMNH 609, of which both preserved the left and right elements. All are largely unaffected by taphonomic processes.

On ETMNH 601, the ASMe and ASN connected on both entocuneiforms. In addition to this, the anterior processes on both bones have numerous accessory processes. On the left entocuneiform of ETMNH 601, the ASN is eroded, being about half the size of that on the right entocuneiform (Erosive band ~4.87-6.66 mm, and up to ~1.45 mm deep). The left entocuneiform hass bone loss anterior to the ASMe with a notable pit/cavity anterolateral to it (~4.04 mm med-lat, ~2.82 mm ant-post, and ~2.67 mm deep).

On ETMNH 609, the entocuneiforms' ASMe and ASN are separated, and the anterior processes are more uniform.

Mesocuneiform

Included specimens: ETMNH 601, 609, 3749, 19280, 33000.

Mesocuneiforms are the second most common rhino tarsal at GFS, being represented by material from five specimens. Only ETMNH 601 and ETMNH 609 preserve both left and right elements. Almost all are intact with only the right mesocuneiform of ETMNH 601 having a defect, missing a small fragment of the rugosity (Short, 2013; Short et al., 2019).

The mesocuneiforms' anterior rugosity are much more developed on ETMNH 601 than on ETMNH 609. On the right in ETMNH 601, the ASEn has been extended proximodistally, connecting ASN and ASMT2, in line with extension of the ASMe on the entocuneiform. The ASEn is also mediolaterally compressed. The left entocuneiform of ETMNH 601 has a large osteolytic feature affecting the ASMT2 anterolaterally, the anterior rugosity posterodistally and the ASEn and ASN laterally (Fig. 28; Channel ~3.73-11.57 mm wide and ~2.25-4.54 mm deep).

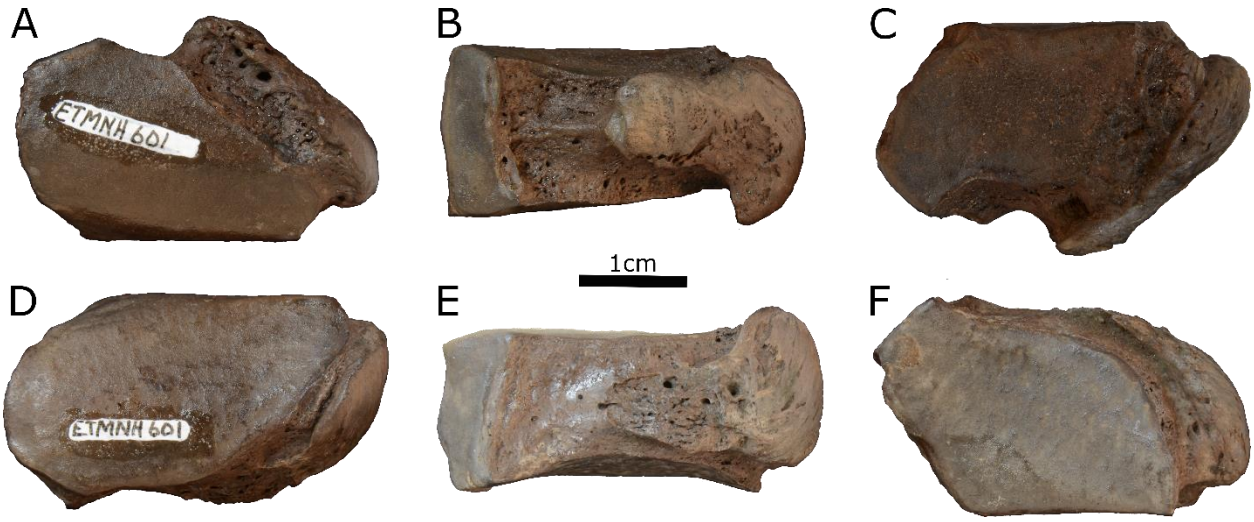

Fig. 28 Mesocuneiforms from ETMNH 601 (*Teleoceras aepysoma* from Gray Fossil Site, Washington Co., Tennessee). Top showing the altered condition of the left mesocuneiform (**A-C**) with a deep channel, and bottom showing normal, unaltered condition the right mesocuneiform (**D-F**). **A** and **D** proximal view, **B** and **E** medial view, and **C** and **F** distal view

The ASEn and ASN are separated on ETMNH 609, and the anterior rugosity is undeveloped relative to the condition in ETMNH 601.

On ETMNH 3749, the condition of the anterior rugosity of the right mesocuneiform is intermediate relative to the other specimens.

ETMNH 19280 has a large bone loss cavity (~8.3 mm ant-post, ~5.3 mm med-lat, and ~3.9 mm deep) on the anterior rugosity adjacent to the ASN of the left mesocuneiform.

The right mesocuneiform's anterior rugosity on ETMNH 33000 is most similar to the condition on ETMNH 609.

Ectocuneiform

Included specimens: ETMNH 601, 609, 33000.

The ectocuneiform has representatives from three specimens. Only ETMNH 33000 does not have both right and left elements, preserving only the right ectocuneiform. The ectocuneiforms are in generally good condition (Short 2013; Short et al. 2019).

Lipping/modification consistent with age/size on ETMNH 601. The ASN and ASMe completely joined on both ectocuneiforms on ETMNH 601.

On ETMNH 609, the ectocuneiform's ASN and ASMe joined posteriorly over a third to half their length.

On ETMNH 33000, the ectocuneiform's ASN and ASMe joining intermediate (3/4 – 4/5 the length) on the right ectocuneiform.

Metatarsals

Included specimens: ETMNH 601, 609, 33000, 37998.

Metatarsals from GFS include elements from four specimens, with ETMNH 601 and ETMNH 609 including all elements, ETMNH 33000 including only the right foot, and a left second and fourth metatarsal from ETMNH 37998. ETMNH 601 and ETMNH 609 are the only specimens with fractured metatarsals requiring reassembly (Short 2013; Short et al. 2019), while the remaining specimens are intact. The left MT2 of ETMNH 601 was broken in half across the diaphysis, right MT3 of ETMNH 601 was broken diagonally across the diaphysis, and left MT4 of ETMNH 601 needed some anteromedial repairs. The fracturing of the left MT3 of ETMNH 609 mentioned by Short et al. (2019) has been entirely covered by the reconstruction efforts used to repair it. In addition to postmortem breakage, the left MT2 of ETMNH 601 has several irregularities associated with the phalanges. ETMNH 609's right metatarsals show more weathering than the left, similar to the naviculars of the specimen. In depth descriptions will be done by element; MT2, MT3, and MT4, respectively.

Metatarsal 2

Included specimens: ETMNH 601, 609, 33000, 37998.

The MT2s of ETMNH 601 have reduced ALPs. The left MT2 of ETMNH 601 has an eroded ASMe corresponding to and forming a pocket with the feature on the left mesocuneiform's ASMT2 (~19.39 mm med-lat, ~7.15 mm ant-post, ~2 mm deep). The proximal articular surfaces have CAT1/2 lipping on their posterior edges, and a large osteolysisal cavity on the anterior surface medial to the ALP (~14.41 mm med-lat, ~11.88 mm prox-dist, and ~7.63 mm deep). The proximal ASPP2 is eroded with a porous surface (~20.18 mm med-lat, ~8.86 mm prox-dist, and up to ~2.88 mm deep), though the underlying bone is solid.

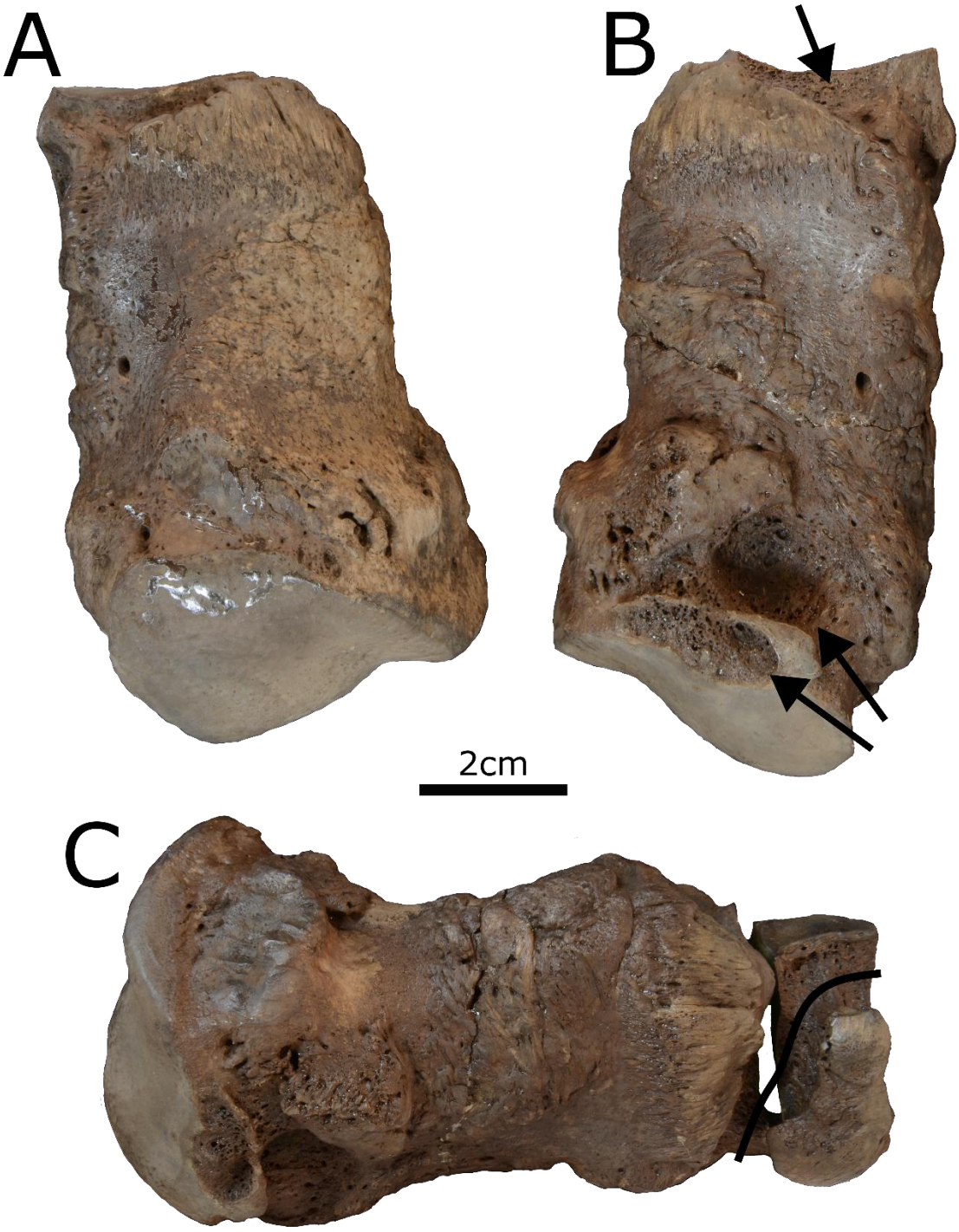

Fig. 29 Second metatarsals (MT2) and left entocuneiform from ETMNH 601 (*Teleoceras aepysoma* from Gray Fossil Site, Washington Co., Tennessee) in anterior view. **A**) unmodified right MT2. **B**) pathological left MT2 with osteolysis to anterior to both articular surfaces (arrows). **C**) showing the cavity formed by the left mesocuneiform and MT2 (line)

ETMNH 609 has the most prominent ALPs, and less rugose diaphyses than on ETMNH 601. The left MT2 of ETMNH 609 has potential osteolysis posteriorly on the boundary of the ASEc and ASMT3 (~4.37 mm ant-post, and ~3.09 mm med-lat).

On ETMNH 33000, the right MT2's ALP is intermediate, with osteolysis laterally adjacent to it (Fig. 30; ~8.26 mm med-lat, ~13.73 mm prox-dist). The ASPP2 has a lateral cavity (~5.3 mm med-lat, ~8.35-12.28 mm prox-dist, and 4.31 mm deep), and osteophyte distal on ASSD1 (~2.99 mm ant-post, ~2.57 mm med-lat) with bone loss proximal (~6.91 mm across, triangular).

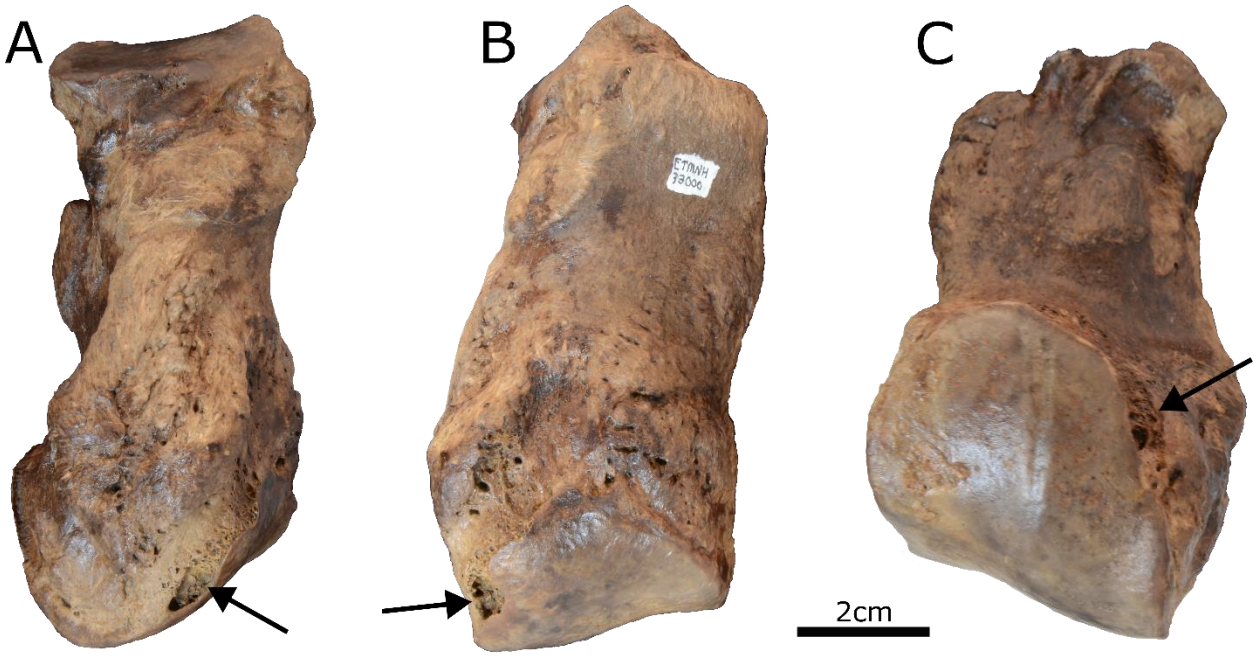

Fig. 30 Right second metatarsal (MT2) of ETMNH 33000 (*Teleoceras aepysoma* from Gray Fossil Site, Washington Co., Tennessee). Note osteolysis laterally adjacent to the distal articular surface denoted by arrows. **A**) lateral view, **B**) anterior view, and **C**) proximal view

The left MT2 of ETMNH 37998 has intermediate ALPs, relative to ETMNH 601 and ETMNH 609. ETMNH 37998 has exaggerated foramina with internal perforations proximal to ASPP2 (8 are greater than 1 mm; the largest is circular: ~7.64 mm med-lat, ~5.31 mm prox-dist,

and ~4.48 mm deep; the 2nd largest is pointed oval-shaped: ~2.02 mm med-lat, ~5.83 mm prox-dist, >4 mm deep).

Metatarsal 3

Included specimens: ETMNH 601, 609, 33000

The right MT3 of ETMNH 601 was broken across the diaphysis postmortem and has been reassembled. Lipping/modification on the bone is consistent with age/size. Marginal lipping is more significant on the left element, being up to CAT2 on posterior proximal articular surfaces. An 'incision' deeper than on ETMNH 609 separates posterior portions of ASCb and ASMT4. This division is more significant on the left element. The left MT3 of ETMNH 601 has an osteolytic incision on posterior corner of ASCb, adjacent to marginal lipping (~2.5 mm ant-post, ~3.78 mm med-lat; right triangle-shaped, apex pointing anteriorly). On ETMNH 33000, the right MT3's ASCb/ASMT4 'incision' is equal to that on the left MT3 of ETMNH 601, though with less distinct lipping.

Metatarsal 4

Included specimens: ETMNH 601, 609, 33000, 37998.

On ETMNH 601, the left MT4 has a large area of bone loss on the anterior edge of the ASCb (~28.5 mm med-lat, ~6.54 mm ant-post/prox-dist, and ~2.2 mm deep). The ASPP4 also has a large osteolytic defect proximal to it (~16 mm med-lat, ~12.3 mm prox-dist, and ~7.6 mm deep), and bone loss on the anterior (~21 mm med-lat, ~8 mm prox-dist, and ~0.7-1.8 mm deep). On ETMNH 33000, the ASPP4 has a bone loss cavity on the medial edge (~3.44mm med-lat, ~9.34mm prox-dist, and ~1.24mm deep).

Pedal Phalanges

Included specimens: ETMNH 601, 609, 12450, 33000, 38065; UTK 2.03 (all from GFS and part of the ETMNH collection).

Phalanges have been recovered from 6 specimens, some represented by full sets (ETMNH 601 and ETMNH 609, with ETMNH 609 only missing the left 4th distal phalanx), while others are only isolated elements (ETMNH 12450 and ETMNH 38065). Sidedness is difficult to discern for some of the less complete specimens, therefore the best guess will be used in these cases. Preservation is good for the most part, with only the fused digit II distal/medial phalanx of ETMNH 601 and one of the digit III distal phalanges of ETMNH 33000 requiring reassembly. Notably, ETMNH 601 has severely pathological phalanges, with all left digit II having some defects (especially the medial and distal phalanges, which are fused) and left digit III distal phalanx being excessively porous on its anterior portion. The descriptions will be sectioned into proximal, medial, and distal phalanges.

Proximal Phalanges

Included specimens: ETMNH 601, 609, 12450, 33000.

The right digit II proximal phalanx of ETMNH 601 has a modified nutritive foramen cavity on the posterior surface adjacent to ASMP2 (~7.07 mm med-lat, ~5.44 mm prox-dist, and ~3.53 mm deep). The ASMP2 has taphonomic weathering on the anteromedial side, as well as a depression on the anterior center of the surface (articular cartilage separation; ~9.37 mm med-lat, ~3.46 mm ant-post, and ~0.76 mm deep) and a line/incision dividing posterior half of the pad between the two lobes (~11.83 mm ant-post). The left digit II proximal phalanx of ETMNH 601 has significant deformation from bone loss and accessory bone growth, reaction to trauma/fusion of the distal two phalanges. The ASMP2 lumpy with healed bone loss. The right digit III

proximal phalanx of ETMNH 601 has an anterolateral postmortem breakage to the ASMT3. The AFF has bone loss medially around it (~2.49-2.85 mm wide), and a small posterior postmortem breakage to ASMP3. The AFF absent on the left digit III proximal phalanx along with potential bone loss on anterior surface adjacent to the proximal and distal articular surfaces. The right digit IV proximal phalanx of ETMNH 601 has a modified nutritive foramen cavity on distal posterior surface adjacent to ASMP4 (~4.35 mm med-lat, ~3.98 mm prox-dist, and ~3.51 mm deep). The ASMP4 has a depression on the anterior (~6.22 mm med-lat, ~4.32 mm ant-post, and ~1.3 mm deep).

The right digit II proximal phalanx of ETMNH 609 has a depression on the anterior of the ASMP2, which is larger than that of ETMNH 601. The depression has barely discernable surface porosity within it (~13.89 mm med-lat, ~4.46 mm ant-post, and ~1.02 mm deep). The left digit II proximal phalanx of ETMNH 609 has a similar depression (~13.67 mm med-lat, ~4.22 mm ant-post, and ~1.07 mm deep). Both digit III proximal phalanges of ETMNH 609 have a small depression on the anterior of the ASMP3, it is more distinct on right than left. The right digit IV proximal phalanx of ETMNH 609 has a small depression on the anterior of ASMP4 (~2.5 mm med-lat, ~7.65 mm ant-post). The left digit IV proximal phalanx of ETMNH 609 has a larger, more developed depression with barely discernable surface porosity within it (~6.65 mm med-lat, ~2.8 mm ant-post, and ~0.60 mm deep), as well as potential osteolysis on the posteromedial edge (~5.1 mm med-lat, ~5.62 mm ant-post).

The right digit IV proximal phalanx of ETMNH 12450 has some anterolateral bone loss on the ASMP4 (~8.66 mm med-lat, ~7.38 mm ant-post).

The right digit II proximal phalanx of ETMNH 33000 has notable anterodistal postmortem breakage. The anterolateral ASMT2 has been eroded, and the AFF and ASMP2 have

a small depression between them (~5.18 mm med-lat, ~2.54 mm ant-post, and ~1.04 mm deep). The right digit IV proximal phalanx of ETMNH 33000 has notable anterior postmortem breakage and osteolysis, both proximally and mediodistally. The ASMP4 has significant active bone loss and pitting on the posterolateral surface (~7.05 mm med-lat, ~6.04 mm ant-post, and ~1.78 mm deep), with an older, deeper healed bone loss cavity anterior with crimping around the edge (~3.13 mm med-lat, ~4.85 mm ant-post, and ~2.05 mm deep), visible in Fig. 31. The left digit IV proximal phalanx of has some shallow depressions on the anteromedial (~4.21 mm med-lat, ~5.97 mm ant-post) and posterolateral ASMP4 (~6.76 mm med-lat, ~5.56 mm ant-post).

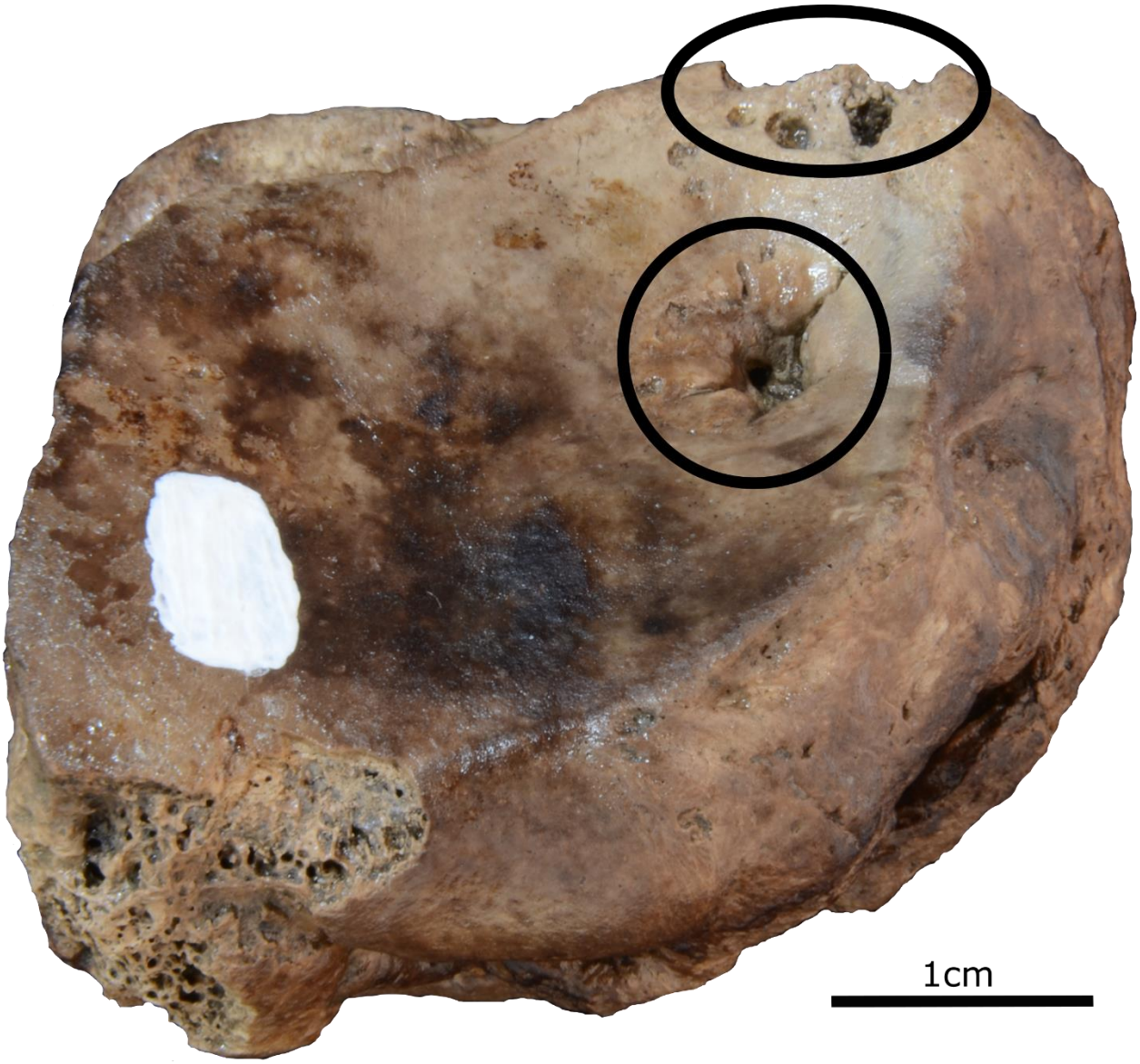

Fig. 31 Right digit IV proximal phalanx of ETMNH 33000 (*Teleoceras aepysoma* from Gray Fossil Site, Washington Co., Tennessee) in proximal view. Note older pathology (circle) and newer pathology (oval)

A lateral proximal phalanx, interpreted to be left digit II, of uncertain association with ETMNH 33000 has osteolysis across the anterior surface, as well as postmortem defects on the anterior of ASMC2 and a depression/channel between ASMP2 and the AAF.

Medial Phalanges

Included specimens: ETMNH 601, 609, 33000.

In ETMNH 601, the right digit II medial phalanx has healed bone loss on the posteromedial ASPP2 (~8.02 mm med-lat, ~4.97 mm ant-post). The right digit II medial phalanx has bone loss on the proximal anteromedial rugosity and distal posterolateral rugosity, like that seen on manual counterparts (~8.41 mm med-lat, ~6.74 mm prox-dist, and ~1.49 mm deep; ~9.06 mm med-lat, ~7.59 mm ant-post/prox-dist, and ~2.04 mm deep). The ASDP2 has a small, linear bone fold on posterior (~2.73 mm ant-post). The left digit II medial phalanx is fused to the distal phalanx with no discernable boundary (CAT4 lipping, Fig. 32), with its ASPP2 widened and pockmarked with healed bone loss as a result of the healed injury. The right digit III medial phalanx of ETMNH 601 is missing the proximal AFF. This likely happened postmortem, due to a visible break surface, though it was potentially aided by bone loss of surrounding material, as indicated by perforations in surrounding material (osteolytic defect spans the whole width of the articular facet, ~1.8-4.67 mm prox-dist, and up to ~5.5 mm deep in places). The posterior lateral surface has evidence of distal osteolysis (~7.5 mm prox-dist, ~6.56 mm ant-post, and ~1.83 mm deep; notable foramina). The ASDP3 has two depressions on the anterior boundary with the absent AAF, between 5-6 mm across. The left digit III medial phalanx of ETMNH 601 has significant osteolysis to the anterior surface, with much of the bone having been eroded away as indicated by the presence of pits over 7 mm wide and 5.5 mm deep in this area. Osteolysis of lateral and medial surface on the left phalanx is more significant than on the right. The right digit IV medial phalanx of ETMNH 601 has mediolateral bone loss along the entire anterior surface (~1.82-4.29 mm prox-dist, and ~3.2 mm deep). The medial surface adjacent to ASDP4 has distal osteolysis (~8.67 mm ant-post, ~4.21 mm prox-dist, and ~0.89 mm deep), and the center of

ASDP4 has a depression (~5.57 mm med-lat, ~3.2 mm ant-post, and ~0.75 mm deep). The left digit IV medial phalanx of ETMNH 601 has an osteolytic pit with a cavitated surface lateral to ASPP4 (~1.64 mm med-lat, ~4.94 mm ant-post, and ~2.1 mm deep), as well as exaggerated foramina on the proximal posterior surface adjacent to ASPP4 more significant than that seen on right (up to 2 mm diameters). The digit IV phalanx has mediolateral bone loss along the whole anterior surface (~2.29-4.22 mm prox-dist, ~3.3 mm and up to ~4.73 mm deep), and distal bone loss around medial and lateral surfaces, with the lateral surface with porous surface (~2.25-5.45 mm prox-dist).

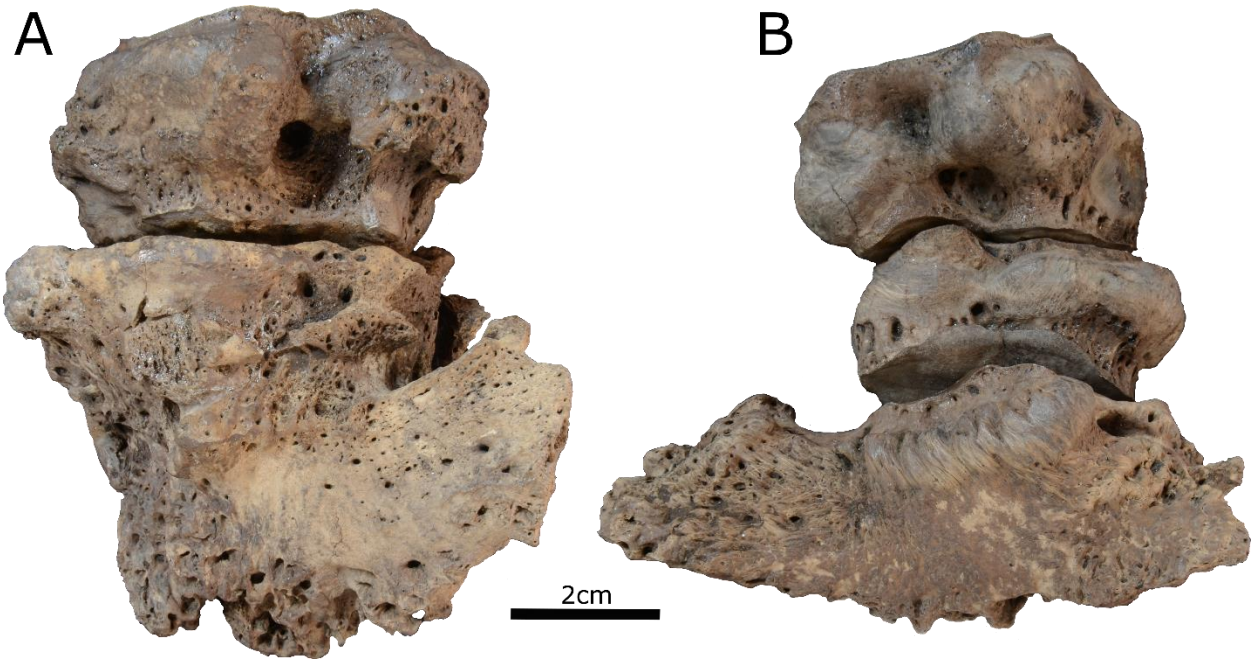

Fig. 32 Both pedal digit IIs from ETMNH 601 (*Teleoceras aepysoma* from Gray Fossil Site, Washington Co., Tennessee) in posterodistal view. Note the ankylosed (fused) medial and distal phalanges of the left pes (**A**) and the unmodified right pes digit (**B**)

In ETMNH 609, the right digit II medial phalanx has some anterior bone loss with perforations (~19.55 mm med-lat, ~1.76 mm ant-post). The phalanx has a small bone loss divot on posteromedial ASDP2 with spurs surrounding it (~2.94 mm med-lat, and ~1.28 mm ant-post).

The left digit II medial phalanx has similar anterior bone loss to that on the right. The right digit III medial phalanx of ETMNH 609 has some anteromedial bone loss on ASPP3 (~7.59 mm med-lat and ~1.45 mm ant-post) and the proximal anterior surface (~4.41 mm med lat and ~2.2 mm prox-dist). The right phalanx has posterodistal bone loss on the medial and lateral surfaces (~10.61 mm ant-post, up to 4.97 mm prox-dist posteriorly; ~12.19 mm ant-post, ~4.07 mm prox-dist), and a depression on the anteromedial ASDP3 with small, barely visible perforations (~8.8 mm med-lat, ~4.09 mm ant-post). The left digit III medial phalanx of ETMNH 609 has some anteromedial bone loss on the proximal anterior surface adjacent to ASPP3, as on right, though more extensive with porous texturing (~7.88 mm med-lat, 2.02 mm ant-post). Similarly, the medial and lateral surfaces display posterodistal bone loss, though less extensive on lateral surface (~6.83 mm prox-dist, ~7.28 mm ant-post, 1.03 mm deep; ~3.57 mm prox-dist, 5.07 mm ant-post, and ~1.26 mm deep). The right digit IV phalanx of ETMNH 609 has anteromedial bone loss on ASPP4 (~3.4 mm med-lat, ~4.38 mm ant-post). The digit III phalanx has distal posterior bone loss on the medial and lateral surfaces (medial - ~3.92 mm prox-dist, 6.28 mm ant-post, 1.1 mm deep; lateral - ~4.74 mm prox-dist, ~3.91 mm ant-post, ~1.3mm deep). The ASDP4 has a sigmoidal depression across the posterior (~16.44 mm med-lat, ~1.58-2.18 mm wide). The left digit IV medial phalanx has similar posterodistal bone loss on medial and lateral surfaces as on right (medial - ~6 mm prox-dist, 7.92 mm ant-post, 1.08 mm deep; lateral - ~3.02 mm prox-dist, ~5.03 mm ant-post, ~0.92 mm deep). The ASDP4 has a sigmoidal depression mirrored from the right, though with a broader central portion (~20.76 mm med-lat, ~8.67 mm ant-post at max).

The right digit II medial phalanx of ETMNH 33000 has posterior bone loss adjacent to ASPP2 (~9.8 mm med-lat, ~4 mm prox-dist, and ~1.3 mm deep), and posterodistal bone loss on the medial and lateral surfaces (~8.9 mm ant-post, ~7.6 mm prox-dist, and ~1.8 mm deep; ~6.8

mm med-lat, ~5.2 mm prox-dist, and ~1.5 mm deep). The ASDP2 has a sigmoidal depression covering nearly the full width of the surface (~18.6 mm med-lat and ~2.3 mm ant-post). The right digit III medial phalanx of ETMNH 33000 has notable anteromedial, posterior, and lateral taphonomic breakage on it. This phalanx also has posterodistal bone loss on the medial surface, and posterior bone loss adjacent to ASDP3. The right digit IV medial phalanx of ETMNH 33000 has anterior bone loss on the ASPP4, and postmortem wear to anterior surface obfuscates extent of bone loss. The right phalanx has posterodistal bone loss on the medial surface. The left digit IV medial phalanx of ETMNH 33000 has perforations on the lateral anterior surface.

Distal Phalanges

Included specimens: ETMNH 601, 609, 33000, 38065; UTK 2.03 (all from GFS and part of the ETMNH collection).

Pedal distal phalanges from GFS are represented by five specimens. Only ETMNH 601 has a complete set, with ETMNH 609 missing the left digit IV distal phalanx, ETMNH 38065 only has a third digit phalange, ETMNH 33000 both digit II and III distal phalanges, and UTK 2.03 being a digit III distal phalanx. Most of the elements have only sustained some taphonomic weathering; whereas ETMNH 601 had the lateral third of the right digit IV distal phalanx broken off, and on ETMNH 33000 the right digit II phalanx was broken in half and the left digit III distal phalanx is partial/broken with the three largest fragments reassembled. ETMNH 601 is the least affected by taphonomic defects and preserves notable pathologies on the left digit II and III distal phalanges. The distal phalanx of ETMNH 38065 is by far the least perforated, likely suggesting it is a much younger individual, and UTK 2.03 appears to be intermediate between ETMNH 38065 and the other specimens.

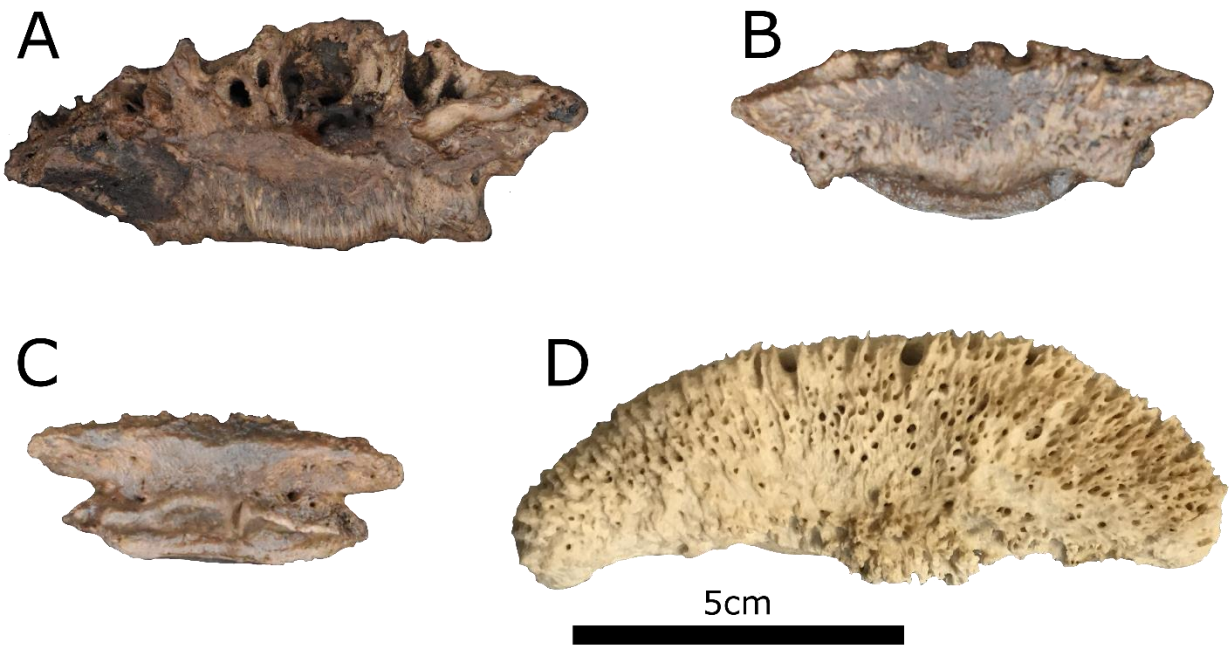

Fig. 33 Distal view of digit III distal phalanges of **A**) ETMNH 601, **B**) ETMNH 609, and **C**) ETMNH 38065 (*Teleoceras aepysoma* from Gray Fossil Site, Washington Co., Tennessee). **D**) distal view of digit III distal phalanx of ETMNH-Z 7216 (*Rhinoceros unicornis*, from Buffalo Zoo). Note the especially large pits and ridges on ETMNH 601 and the comparative smoothness of ETMNH 38065

The right digit II phalanx of ETMNH 601 is porous on the anterior portion of the distal phalanx. The ventral side of the distal phalanx has enlarged nutritive foramen on the anterior (largest foramen: ~7.2 mm ant-post, ~4.9 mm med-lat, and ~7.5 mm deep). The left digit II distal phalanx is fused to the medial phalanx (CAT4), as mentioned previously. It is significantly disfigured with reactive bone. The right digit III distal phalanx of ETMNH 601 is porous on the anterior portion of the distal phalanx. The ASMP3 has bone loss anterior to it (~14.4 mm med-lat, ~1.2 mm ant-post, and ~0.6 mm deep). The left digit III distal phalanx has more anterior bone loss than the right (~30.4 mm med-lat, ~1.3-2.8 mm ant-post, and ~0.5 mm deep). The anterior ventral/distal surface has greatly enlarged nutritive foramen/amalgam of multiple

foramina (~13.47 mm med-lat, ~17.3 mm ant-post, ~11.17 mm deep). The right digit IV distal phalanx of ETMNH 601 is partial, with the lateral third having been broken off postmortem. It was subsequently reassembled. The nutritive foramina on the posterior surface adjacent to ASMP4 are covered by matrix. The left digit IV distal phalanx has increased porosity on anterior portion of the distal phalanx, likely in reaction to the second digit pathology (largest foramen: ~8.6 mm med-lat, ~4.7 mm ant-post, and ~7.6 mm deep).

In ETMNH 609, the right digit II distal phalanx has some taphonomic weathering of the proximal anterior portion. Both right and left digit III distal phalanges on ETMNH 609 have enlarged nutritive foramina on the distal anterior. The left digit IV distal phalanx of ETMNH 609 has some lateral taphonomic weathering on the anterior.

The right digit II distal phalanx of ETMNH 33000 has porosity intermediate between ETMNH 601 and ETMNH 609. The left digit II distal phalanx of ETMNH 33000 has taphonomic weathering on the anterior. The right digit III distal phalanx of ETMNH 33000 has intermediate porosity, with enlarged anterodistal foramina indicative of age. The left digit III distal phalanx is partial and broken, with heavy taphonomic weathering and the three largest fragments reassembled.

The digit III phalanx (inferred as pedal due to small size compared to other phalanges) of ETMNH 38065 has some taphonomic weathering on the left end of the bone. Relatively under perforated anterior compared to the other specimens, especially ETMNH 601.

UTK 2.03 digit III distal phalanx has postmortem breakage to the right end, with gross perforations on the anterior surface.

Pedal Sesamoids

Included specimens: ETMNH 601, 609, 3752, 33000.

Pedal sesamoids have been recovered from four specimens. Only ETMNH 609 preserves a full set of metatarsal sesamoids, with ETMNH 601 missing the left MT2's lateral sesamoid, and ETMNH 33000 having five unidentified metatarsal sesamoids from the right foot. Phalangeal sesamoids are only preserved in ETMNH 601 (4) and ETMNH 3752 (1). Only the right medial MT2 and MT3 sesamoids and digit IV phalangeal sesamoid from ETMNH 601 required reassembly.

On ETMNH 601, the right medial MT2 sesamoid is broken on posterior dorsal side, mostly reassembled. The lateral sesamoid's ASMT2 has CAT2 marginal lipping on the ventral edge. The right medial MT3 sesamoid of ETMNH 601 has ventral breakage and is mostly reassembled. The right medial sesamoid has an enlarged medial foramina cavity with medial bone loss (total cavity size: ~11.7 mm ant-post, ~20.8 mm dors-vent, and ~2.2 mm deep). The lateral MT3 sesamoid has bone loss lateral to the lateral foramen (~4.8 mm ant-post, ~10.2 mm dors-vent, and ~2.2 mm deep). The right MT2 phalangeal sesamoid of ETMNH 601 has bone loss around the articular surface, with the greatest extent being on dorsal side (in reference to label; ~3.8 mm ant-post and ~1.4 mm deep). The left MT2 sesamoids are deformed sympathetic to the second digit pathology. The medial left MT2 sesamoid has bone loss along the entire lateral surface adjacent to ASMT2 (~3-5 mm ant-post, and ~2 mm deep). This bone loss is mirrored on the lateral MT2 sesamoid (~2.2-3.5 mm ant-post, and ~2.1 mm deep), in addition to antero-ventral bone loss (~16.9 mm med-lat, ~2.8-61 mm dors-vent, and ~3.1 mm deep). The ventral rugosity has further bone loss (~14.2 mm ant-post, ~22.2 mm med-lat, and ~3.7 mm deep). The right MT3 phalangeal sesamoid of ETMNH 601 has osteolysis along the whole dorsal surface (in reference to label) adjacent to articular surface (~2.3-4.4 mm ant-post and ~1-1.2 mm deep). The left medial MT3 sesamoid has bone loss medial to medial foramina (~7.9 mm ant-

post, ~12.6 mm dors-vent, and ~2.1 mm deep), and on the medial side of the dorsal rugosity (~9.8 mm ant-post, ~14 mm dors-vent, and ~1.6 mm deep). The right MT4 phalangeal sesamoid of ETMNH 601 is broken on the left side (in reference to label) and has been reassembled. The left lateral MT4 sesamoid with mediodorsal and ventral postmortem breakage and weathering on ASMT4. The medial left MT4 sesamoid has bone loss on the lateral surface adjacent to ASMT2 (~8.2 mm ant-post, ~11.3 mm dors-vent, and ~2.1 mm deep). The bone loss on the medial sesamoid is mirrored by marginal lipping (CAT2) which extends anteroventrally on the lateral MT4 sesamoid (~8.2 mm ant-post, ~11.3 mm dors-vent, and ~2.1 mm deep). The left medial MT4 sesamoid has lateral postmortem breakage and weathering on dorsal and ventral portions of ASMT4.

The left lateral MT2 sesamoid of ETMNH 609 has osteolysis ventrally adjacent to ASMT2 (~3.6 mm dors-vent, ~8 mm med-lat, and ~1 mm deep). The left medial MT3 sesamoid has a larger foramina cavity than the lateral, smaller than on right. The left MT4 medial sesamoid has ventral bone loss next to ASMT4 and appears to extend from a foramen (~2.6 mm ant-post, ~7.4 mm med-lat, and ~0.8 mm). Both right MT4 sesamoids of 609 have bone loss ventrally adjacent to ASMT4 (medial: ~3.6 mm ant-post, ~9.5 mm med-lat, and ~0.4 mm deep; lateral: ~11 mm dors-vent, ~3.3 mm med-lat, and ~0.6 mm deep).

On ETMNH 3752, the left digit IV phalangeal sesamoid (based on comparison to ETMNH 601) has dorsolateral bone loss anteriorly adjacent to the articular surface (directions in reference to label; ~1-9.3 mm ant-post and ~1.6 mm deep).

The probable right medial MT2 sesamoid of ETMNH 3300 has a depression on the lateral side. An unidentified sesamoid associated with ETMNH 33000 (probably right medial/left lateral MT3 sesamoid based on relative size) is partial with the dorsal most portion absent. An

unidentified sesamoid associated with ETMNH 33000 (probably right lateral/left medial MT3 sesamoid based on relative size) is in good condition with some weathering on the ventral articular surface exposing cancellous bone. On a probable right medial MT4 sesamoid, only the medial side of the ASMT4 does not have some degree of adjacent bone loss (~2.6-4.4 mm wide, and ~0.7-1.4 mm deep). A probable right lateral MT4 sesamoid has ventrolateral bone loss adjacent to ASMT4 (~17 mm dors-vent, ~4.3 mm med-lat, and ~0.9 mm deep).

CHAPTER 4. DISCUSSION

Nasal Defect

The shape of the nasal's rostral point on ETMNH 12175 (Fig. 4) is potentially the result of taphonomic effects (e. g. weathering, compression, etc.). This is unlikely as, although the rostral point displays a higher degree of weathering than the rest of the nasal, the amount of weathering required to achieve the present shape would expose trabeculae not currently exposed in ETMNH 12175. Congenital defects or healing from an injury cannot be ruled out as causes prior to comparison to a larger sample.

Lambdoid Asymmetry

Asymmetry of the lambdoid crests of ETMNH 609 was suggested to be pathological by Short et al. (2019), with the current paper noting that the lambdoid crests of ETMNH 601 are also asymmetrical, though to a lesser degree (Figures 1 & 33). Preferential chewing instigated by dental and periodontal pathology has been noted to cause asymmetry in the cranium of other mammals (e.g. Howell 1925; Kargopoulos et al. 2023 preprint) and sided/handedness causing similar asymmetry in humans (e.g. LeMay 1977). Despite the intuitive nature of this idea, most references are anecdotal at best. It should be noted that at least some of the asymmetry of ETMNH 601 is attributable to taphonomic damage, so the full in-life extent of the lambdoid of ETMNH 601 is unclear (Fig. 34). Looking at specimens from another sample of *Teleoceras* from AFB, very slight asymmetry is also observed on UNSM 52272 (Fig. 34), while the asymmetry of USMN 52239 is more typical of taphonomic distortion (Fig. 34). Whether the asymmetry of the lambdoid crests is pathological, taphonomic, congenital, or some combination is difficult to discern at this time. Properly addressing this question is beyond the scope of this study and

would require a more detailed examination of other populations and/or species within the genus and modern taxa.

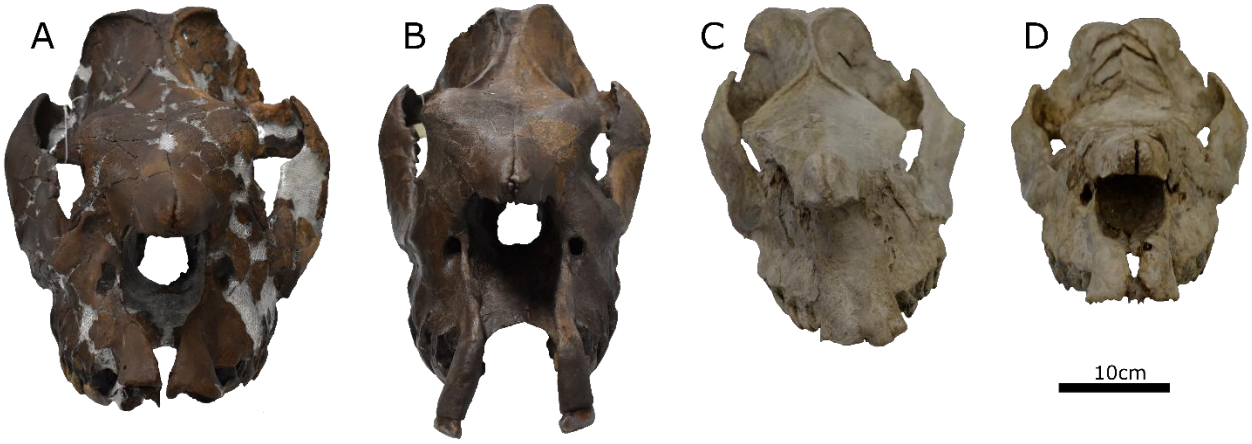

Fig. 34 Anterior view of crania from *Teleoceras aepysoma* from Gray Fossil Site (GFS), Washington Co., Tennessee (**A** is ETMNH 601 and **B** is ETMNH 609) and *Teleoceras major* from Ashfall Fossil Bed (AFB), Antelope Co., Nebraska (**C** is UNSM 52239 and **D** is UNSM 52272) comparing the symmetry of the lambdoid crests. The GFS specimens are not fully intact and so the full extent of asymmetry is hard to discern, while the intact AFB specimens provide an example to compare. **C** shows asymmetry typical of taphonomic deformation, while **D** appears to be undeformed

Periodontal Pathology

Lesions noted on ETMNH 601, ETMNH 609, and ETMNH 21659 lend themselves to being interpreted as pathologies, as the pores noted in the description do not compare well with cancellous bone that would be exposed by taphonomic processes. These lesions can be interpreted as periodontitis, as bone loss to alveolar bone is diagnostic of periodontitis (Mariotti 2007). The dentary of ETMNH 21659 preserves a notable lingual pathology in the form of a pathological exostosis on the lingual side of the dentary below the m3 (Fig. 5). Periodontal pathologies in zoo animals are known to propagate further down into the dentaries and form

larger lesions (K. Volle pers. comm. 2023). Despite the dramatic exostosis in ETMNH 21659, it is only superficially related to the underlying bone (as seen in Fig. 5). Lack of more direct impact on the underlying bone suggests that the propagation was outside the bone, rather than internal and/or that insufficient time had passed for a deeper influence. What the superficial relationship of the exostosis and underlying bone means is uncertain at this time and further diagnosis is beyond the scope of this study.

Moodie (1922) reported a pathology similar in description to ETMNH 21659 in *Aphelops*. Another similar pathology, though more severe than the condition in ETMNH 21659, was noted in a specimen of *Equus simplicidens* by Griffin et al. (2016). Both studies compared their observations to "lumpy jaw" (Moodie 1922; Griffin et al. 2016). "Lumpy jaw" (often actinomycosis) is a disease often seen in cattle and other domestic ungulates and is typically attributed to the bacterial genus *Actinomyces* (Moodie 1922; Leader-Williams 1982; Hoefs and Bunch 2001; Griffin et al. 2016). Actinomycosis has also been reported in captive rhinos (Silberman and Fulton 1979). In the *E. simplicidens* specimen however, Griffin et al. (2016) suggested that a dental abscess was the most likely cause in their specimen, as equids rarely carry *Actinomyces*. Though, Griffin et al. (2016) also indicated that more in-depth study, including histology, would be required to come to a definitive conclusion. The pathologies exhibited by ETMNH 21659 may also be compared to pathologies seen in zoo animals suffering from periodontal diseases which propagated further into the mandible (K. Volle pers. comm. 2023). Further research on the dentary exostosis of ETMNH 21659 is recommended for a researcher more familiar with dental pathology.

Apparent frequency of periodontal pathology seems to be higher in the GFS *T. aepysoma* sample than that of other *Teleoceras* populations, such as Ashfall Fossil Beds (AFB). This

frequency could be the result of the shift towards browsing (as suggested by DeSantis and Wallace 2008), rather than grazing diet, as is typical of the genus (Voorhies and Thomasson 1979; Wang and Secord 2020). This might be explained by the paleoenvironment of GFS representing suboptimal habitat for *T. aepysoma*, as the best specimens from GFS represent the demographic observed to be the most susceptible to being ousted from prime habitat in *Rhinoceros unicornis* (Dinerstein, 2003), those being younger (ETMNH 609) and injured males (ETMNH 601 and ETMNH 33000). Zoo veterinary and zooarchaeological literature supports this interpretation, indicating that changes to an animal's diet can result in an increase in periodontal pathology (Coyler 1936; Robinson 1979; Groves 1982; Leader-Williams 1982; Contreras 2005; Holmes et al. 2021). Changes in diet can potentially result in food and mineral particulates becoming compacted between the teeth, thus causing trauma to the gums and alveoli (Hoefs and Bunch 2001; K. Volle pers. comm. 2023). If the Palmetto Fauna *Teleoceras* are indeed *T. aepysoma*, as suggest by Short (2013), then evaluation of this more typical lowland savannah sample for periodontal pathology could provide valuable insight as to whether the highland forest environment (Shunk et al. 2006; Ochoa et al. 2012) of the GFS *T. aepysoma* population is responsible for heightened presence of periodontal pathology.

Tusk Pathology

The marks forming shallow cross-cutting angles (grooves) preserved on the left tusk of ETMNH 33000, the oldest rhino thus far recovered at GFS, are unlikely to be the result of regular wear from occlusion as they are on the anterior of the tusk near the gumline. Taphonomic damage is unlikely because the grooves are not consistent with trowel marks or other forms of taphonomic damage. Though, the damage to the right tusk noted in the description is more likely a result of taphonomic damage. A potential explanation more consistent with the characteristics

on the left tusk of ETMNH 33000 is that they were sustained in intraspecific combat, most probably via face biting as exhibited in more basal rhinos (Hieronymus 2009; Hieronymus et al. 2009) and in *R. unicornis* (Laurie 1982; Dinerstein 2003). Dinerstein (2003) observed that male *R. unicornis* received damage to their tusks during serious confrontations, and that those with broken tusks would retreat to less contested areas. The absence of such pathologies in the younger type specimens (ETMNH 601 and ETMNH 609) is consistent with this hypothesis, as those specimens have had less time in the proverbial ring to develop such pathologies. In *R. unicornis*, younger males are not observed to participate in serious face-to-face confrontations until they reach full size (Dinerstein 2003).

Rib Pathologies

Out of all the elements recorded from the GFS *T. aepysoma* sample in the current paper, the most prominent pathologies are observed in the right ribs of ETMNH 601. Specifically, an ankylosed callus is distally located on two of the anterior right ribs with two rugose swellings proximal to the callus (Fig. 8). The fused rib callus of ETMNH 601 is recognized as fully healed bone (L.G. Emmert pers. comm. 2023), and is verified by micro-CT scans, with uniform and well-organized trabeculae and no adjacent reactive bone (Fig. 8). The proximal swells appear to be less healed than the callus, given their rugose texture and swelling relative to the adjacent bone (Lovell 1997; and as seen as in Fig. 8); an interpretation corroborated by micro-CT, with the proximal swells showing larger and less well-organized trabeculae than the callus (Fig. 8). The differential healing between the callus and swells, with the less healed swells being interpreted as the more recent breaks, suggests multiple trauma instances caused by repeated behavior. This interpretation assumes an equal rate of healing for both injuries, though rate of bone formation can vary (Thompson 2015).

Proximal swells of ETMNH 601 compare favorably to a rib fracture present on ETMNH-Z 7216 (Fig. 8), however the trauma seen in ETMNH 601 is notably more severe. The rib fracture of ETMNH-Z 7216 was sustained after falling on his side during mounting (K. Volle pers. comm. 2023). Given that ETMNH-Z 7216 was a taller animal than ETMNH 601, this would speculatively suggest that ETMNH 601 either suffered a greater fall, unlikely given that only two ribs show evidence of trauma, or that ETMNH 601 received these injuries from a directed impact from either another rhino or other large animal. A behavioral cause seems to have more potential, especially given that the rib fractures of ETMNH 601 are at different stages of healing. This suggests the cause was habitual behaviour, such strikes to the flank during intraspecific combat, rather than a singular event such as a fall. Similar rib injuries resulting from kicking are well documented in feral horses (Grogan and McDonnell 2005; Knubben et al. 2008), as well as fossil *Equus* (Van Kolfschoten et al. 2015). Diedrich (2008) discussed this kind of injury in *Coelodonta* and Mead (2000) mentions most *Teleoceras* he observed have at least one broken rib. Previous studies have used mortality bias in young adult male *Teleoceras* (Mihlbachler 2003) and *Menoceras* (Mihlbachler 2007) to suggest the occurrence of agonistic behaviour in these animals. If the hypothesis of agonistic behavior is true, then the rib callus of ETMNH 601 (and tusk marks of ETMNH 33000) represent some of the first direct physical evidence for this kind of behavior in *Teleoceras*.

ETMNH 601 also has a proximal right rib fragment, most likely one of the posterior right ribs, that has been significantly expanded with lipping and has an irregular surface with pits and bumps (Fig. 9). These features seem most comparable to a healed (sub)luxation (Redfern and Roberts 2019, figure 9.63 page 259). A potential cause for the (sub)luxation would be traumatic flexion of the ribcage, which would be consistent with being struck in the side by a large object.

The causal factors presented here for both sets of pathological ribs on ETMNH 601 are hypotheses.

The above potential evidence for agonistic behavior in the GFS *T. aepysoma* may a result of less space for display/sizing-up competitors, due to the more enclosed habitat of GFS compared to other *Teleoceras* samples (Short et al. 2019), or due to the small sample sized compared to sites such as AFB. Given the status of GFS as an attritional site rather than a catastrophic site, which provide more accurate snapshots of grouping behaviors (Voorhies 1969; Mihlbachler 2003), such hypotheses about population dynamics at GFS are tenuous at best.

Innominate Pathologies

The condition of the right acetabulum is less severe in both ETMNH 601 and ETMNH 609, with only the left innominate of ETMNH 601 having a cavity whereas the right acetabulum of ETMNH 601 being unaffected by pathology (Fig. 26). Of note, the insertion point of the ligamentum teres tends to be located ventroposteriorly in the acetabulum (Cerezal et al. 2010). This places the acetabulum pathologies proximate to the ligamentum teres, suggesting the ligaments involvement with these pathologies. The rim of the cavity on the left acetabulum of ETMNH 601 is raised, suggesting an avulsion (Yu and Yu 2015), likely caused by a hip subluxation or some similar physical stressor to the ligamentum teres (Delcamp et al. 1988; Cerezal et al. 2010, figure 11, page 1646). Furthermore, the left acetabulum of ETMNH 601 has a shallow extension in the anteroventral/longest direction, suggesting an earlier, less severe or healed injury. The left innominate of ETMNH 609 appears to have had an avulsion fracture (Cerezal et al. 2010) that healed, either by refusion of the fractured plug or infilling of new bone (Fig. 26). The right innominate has multiple small pits (Fig. 26), likely indicating something similar to a partial avulsion fracture. Both acetabula of ETMNH 609 exhibit a cavity surrounded

by rugose bone part way across the surface from the assumed insertion point of the ligamentum teres. A similar pathology is seen in humans suffering from ligamentum teres with degenerative fraying (Cerezal et al. 2010, figure 11c page 1646). Such injuries to the ligamentum teres in humans has largely been attributed to over extension/exertion of the joint during strenuous activity, as observed the increase frequency of such injuries in athletes (Byrd and Jones 2004).

A possible cause for the suggested avulsions in ETMNH 601 and ETMNH 609 would be that these individuals underwent regular strenuous activity (Yu and Yu 2015; K. Volle pers. comm. 2023), perhaps losing their footing and slipping occasionally, while traversing uneven terrain common in the region of the fossil site. Asymmetrical presence of the acetabulum pathology in ETMNH 601 is possibly associated with the left foot pathology, via asymmetrical stresses from limping. Additional pathologies in ETMNH 609 are similar to those seen in humans suffering from ligamentum teres with degenerative fraying (Cerezal et al. 2010, figure 11c page 1646). Such pathologies in humans are typically associated with osteoarthritis, with 60% of patients having some kind of joint condition (Cerezal et al. 2010). A similar but smaller cavity to those seen in ETMNH 601 and ETMNH 609 is also present in the acetabulum of ETMNH-Z 7216's right innominate (Fig. 26), though, since there are no trauma events corresponding with these features on ETMNH-Z 7216 (K. Volle pers. comm. 2023), it is likely these are indicators of old age on ETMNH-Z 7216. Though old age may be a partial explanation for these features in the GFS rhinos, it does not satisfactorily explain why ETMNH 609, the younger specimen, shows a greater incidence of these pathologies in its acetabula than 601. Given that the femoral heads are unafflicted by defects in ETMNH 601 and ETMNH 609, hip dysplasia as observed in *Diceratherium* by Stecher et al. (1962) is unlikely.Further finds from GFS will reveal if this is a typical trend in the GFS *T. aepysoma*.

Femoral Pathologies

The right femur of ETMNH 601 has a pathology in the fibrous bone/muscle scarring on the posterior femoral MEc with the left femur's MEc appearing to have a similar pathology, though older/healed with fibrous bone infilling (Fig. 27). The right pathology appears most similar to an avulsion fracture (Yu and Yu 2015), likely the result of a pulled tendon (Fig. 27). Pathologies on both femora's MEc could have resulted from an over-extension, or excessive use (K. Volle pers. comm. 2023), as is hypothesized for the pathologies in the acetabula of ETMNH 609; or as a result a modified gait (as defined by Weiss et al. 2008) due to the injury to the left toe and/or rheumatoid arthritis (RA) in the distal limb bones. Interpretation of the femur pathologies as avulsions is brought into question by the lack of adjacent reactive osteophytes that would be expected for such traumatic pathologies (K. Volle pers. comm. 2023; and as defined by Cook, 2015; Waldron, 2020).

Foot Pathologies

The lower limb bones display the highest quantity of defects observed in the GFS rhinos, especially the carpals, tarsals, and phalanges, though few of these defects are as prominent as those seen in the ribs. The presence of porous, reactive bone in the erosions described in the manual and pedal elements does not appear consistent with that of natural bone modification (or remodeling) as defined by Wolff's Law (Rowe et al. 2018) or trabecular bone exposed by natural or artificial taphonomic forces (Fig. 1). Many of the features noted in the description seem consistent with rheumatoid arthritis (RA) and synovitis (Fig. 35), particularly the marginal osteolysis seen on the phalanges (Schett and Gravallese 2012). Synovitis and RA are suggested to be co-occurring/linked diseases in the literature (Tan et al. 2003; Schett and Gravallese 2012). Factors discouraging interpretation of these marginal pathologies as other types of

destructive/degenerative arthropathies (such as psoriatic arthritis, gout, osteoarthritis, etc.) are the lack of peripheral exostoses and erosion directly to the joint surfaces typically associated with these arthropathies (Stevanović et al. 2015). Schematic examples of various arthropathies can be seen in Fig. 36.

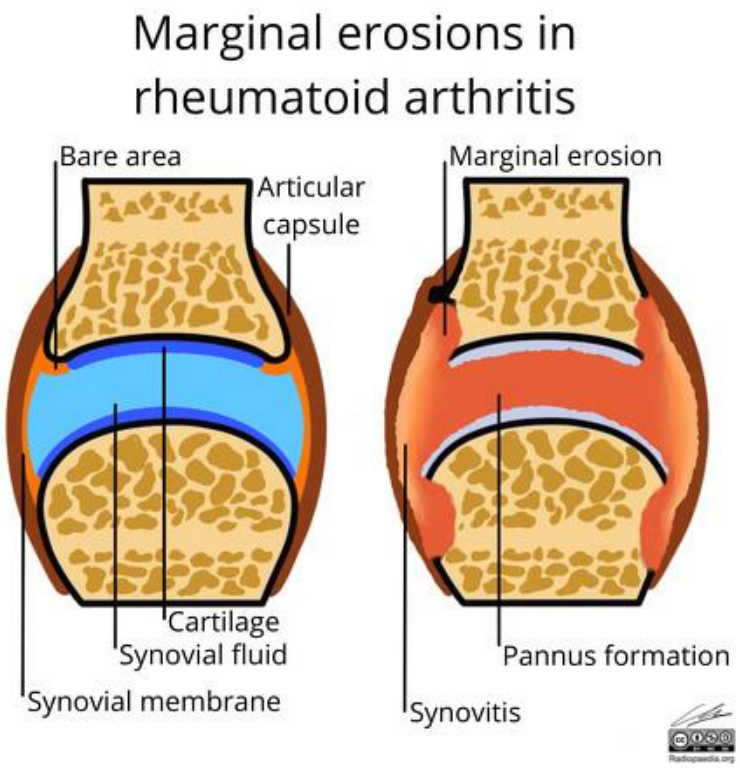

Fig. 35 "Marginal erosions in rheumatoid arthritis" by Gendy D. Licensed under CC BY-NC-SA 3.0 DEED

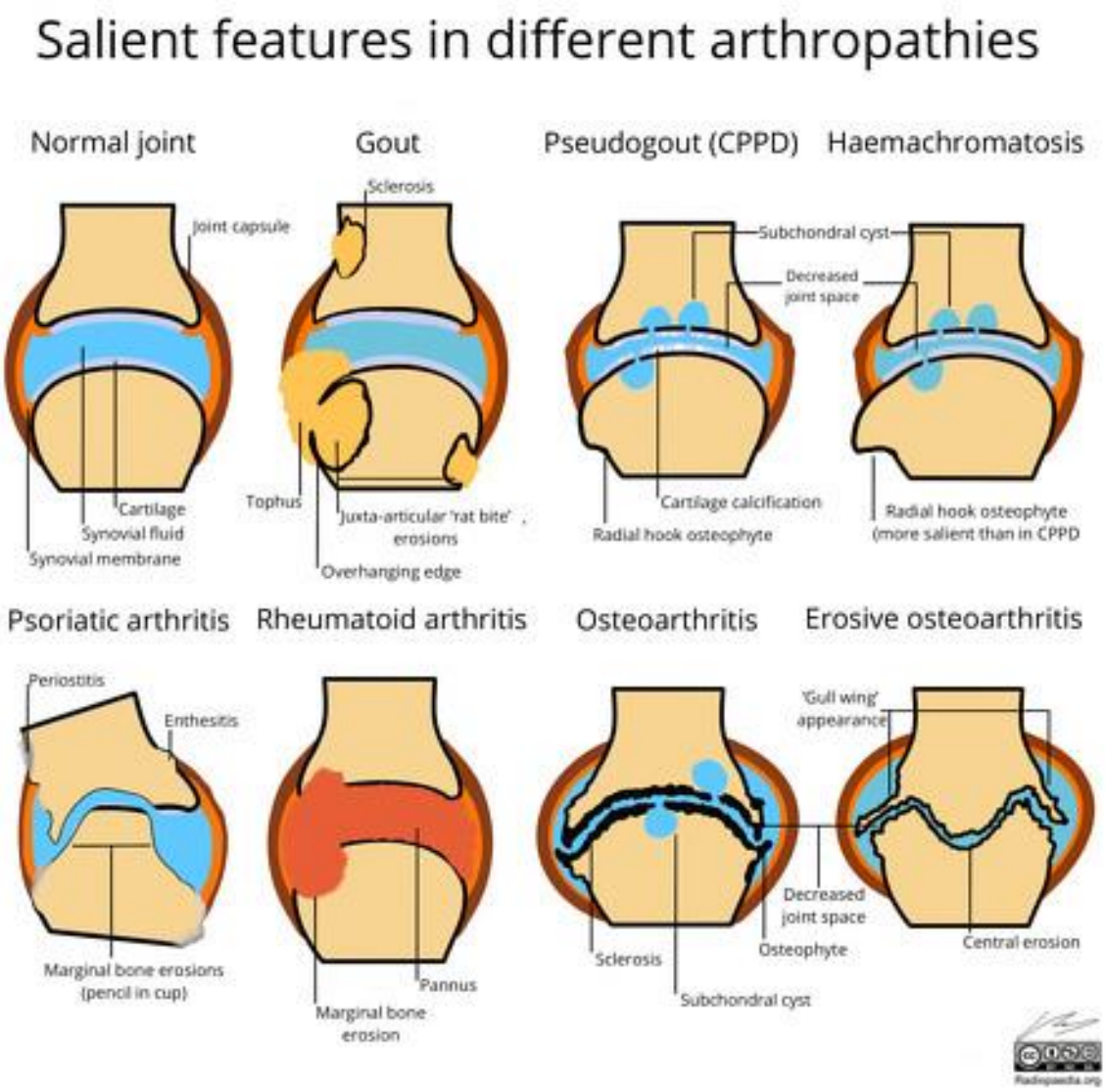

Fig. 36 Schematic examples of various arthropathies. "Salient features in different arthopathies" by Gendy D. Licensed under CC BY-NC-SA 3.0 DEED

Pathologies in the carpals and tarsals consist primarily of arthropathies, most of which are the beginnings of marginal lipping with some exostoses and osteolytic lesions present as well. One set of elements displaying all these arthropathies are the lunars of ETMNH 601 and ETMNH 33000 (Fig. 14 and 15). It cannot be ruled out that some of these defects, such as the depressions in the calcaneum dorsal ridges of ETMNH 609, are instead modification to accommodate soft tissue structures (nerves, blood vessels, ligaments, etc.). Given that caveat,

both ETMNH 609's calcaneum arthropathies and a similar arthropathy described on the left cuneiform ASUL of UTK 1.06/ETMNH 19280 (Fig. 17) bears resemblance to a purported cleft in the articular cartilage of a camelid's phalangeal joint (as seen in figure 6, page 113, Baker and Brothwell 1980). The prevalence of lipping arthropathy in the carpals and tarsals of the GFS *T. aepysoma*, noted to be a large member of the genus (Short 2013), is unsurprising given the complex and multidirectional articulations under regular stress from the forces of bearing weight and movement (Burt et al. 2013), especially in a large animal. The variation in overall shape of the carpals and tarsals, such as in the trapeziums (Fig. 19), from GFS sample *T. aepysoma* is easily attributable to bone modification (or remodeling) in accordance with Wolff's Law (Rowe et al. 2018).

Metapodials have a paucity of pathologies compared to the other distal limb bones, perhaps a result of the relative simplicity of their articulations compared to the carpals and tarsals, and robustness compared to the phalanges. Pathologies on the metapodials follow a similar pattern to that seen in the carpals and tarsals, consisting of arthropathies including a majority of lipping with some osteolysis. Though osteolysis is more prevalent in the metatarsals than the metacarpals, with ETMNH 601 exhibiting a prominent proximal and distal osteolysis (Fig. 29). Though marginal osteolysis may be attributable to RA (Fig. 35 and Fig. 36), the fact that the proximal arthropathy forms a continuous channel across the joint to the mesocuneiform casts doubt on such a diagnosis. Osteolysis as a result of immune mediated infection, perhaps stemming from an external injury is one alternative diagnosis for the left metatarsal pathologies of ETMNH 601. The proximity of the 2nd metatarsal pathologies and the digit II pathologies distal to it is provocative, suggesting an associated etiology, but without more extensive

comparative literature/material, further diagnosis regarding their association is beyond the scope of this study.

The phalanges carry a higher pathology occurrence than the metapodials, with marginal osteolysis being prevalent on the manual phalanges, especially on those of ETMNH 601 (as seen in Fig. 23 and Fig. 24), and the pedal phalanges carrying more pathologies toward the distal end (such as the ankylosed left digit II of ETMNH 601, Fig. 32). The heightened severity of osteolysis present on digit III (the main weight bearing digit) in type specimens (ETMNH 601 and ETMNH 609) suggests heightened stresses from locomotion, perhaps due to the increased size of *T. aepysoma* relative to other members of the genus (Short et al. 2019). Though it is tempting to attribute the marginal erosions as age related features, as the younger ETMNH 609 expresses less severe osteolysis than ETMNH 601, the older ETMNH 33000 has a similar reduced presence, comparable to ETMNH 609. This may suggest that the left foot injury caused ETMNH 601 to adopt a modified gait which caused additional stresses, or that ETMNH 601 was more active than the other two, incurring more stresses/microtrauma resulting in the increased expression of pathology on ETMNH 601. Marginal erosion, in combination with the absence of marginal lipping and exostoses diagnostic of other kinds of arthritic diseases (Stevanović et al., 2015), suggests RA as the most plausible diagnosis with the symmetrical presence of these pathologies, a diagnostic feature of RA (Tan et al. 2003; Walker and Colledge 2013), further bolstering such an interpretation.

In the pedal phalanges, the notable osteolysis and exostoses on digits II and III of the left pes of ETMNH 601 are dramatic indicators of pathology, especially the ankylosed medial and distal digit II phalanges (Fig. 32). Previous work on the material suggested that the injury could have resulted from a mating related traumatic injury, where the female stepped on the toe of

ETMNH 601 during mounting (L.G. Emmert pers. comm. 2023). Alternatively, the proliferation exostoses and ankylosis of digit II's interphalangeal joint compare well to osteoarthritis (Wilczak and Jones 2017, Figure 9.5, page 80). Similar osteoarthritic interphalangeal fusion seen in horses results from chronic overuse or repetitive trauma (Janeczek et al. 2017), a not unreasonable possibility in the karst, hilly terrain of the GFS. One peculiar factor of the left pes digit II's ankylosis that could refute osteoarthritis is how localized it is. Normally osteoarthritis has a broader effect as asymmetrical loading exacerbates it (Walker and Colledge 2013), but for only a single digit to be affected, and to such a degree, seems unusual. Perhaps the digit III pathology may be considered when investigating the etiology of digit II's ankylosis. The digit III distal phalanx from the left pes of ETMNH 601, the same foot as the ankylosed digit II, has a notable osteolytic lesion on the anterodistal end (Fig. 33). Perhaps the digit III pathology is pedal osteitis resulting from trauma accumulated from excessive stress (K. Volle pers. comm. 2023), though the digit III pathology could also result from an injury to the toe (by stepping on a sharp rock, getting bitten by a predator, etc). The totality of ankylosis on digit II's distal phalangeal joint suggests that it predates digit III's pathology, potentially causing pedal-osteitis to occur through a modified gait accommodating the fused digit. Other pathologies more proximally located on the left hind limb of ETMNH 601 (2^{nd} metatarsal, mesocuneiform, femur, and innominate), and even the right-side rib callus, may need to be accounted for when considering the etiology of ankylosis in digit II. Though, it is noted in the literature that osteoarthritis can occasionally arise spontaneously, without any external predisposing factors (Stevanović et al. 2015). Some suggested etiologies include repetitive trauma because of a favored stance during mating, which can take several hours in modern rhino species (Dinerstein 2003), resulting in the same toe being stepped on numerous times over the years; or RA, which is noted to cause ankylosis in the

interphalangeal joints in humans (Stecher 1958). Diagnosis as RA is consistent with other related features elsewhere in ETMNH 601 and the other GFS *T. aepysoma*. Diagnosis as RA is consistent with other related features elsewhere in ETMNH 601 and the other GFS *T. aepysoma*. Diagnosis as RA is consistent with other related features elsewhere in ETMNH 601 and the other GFS *T. aepysoma.* Given the complex interplays of pathologies across the body of ETMNH 601, and accumulation of multiple distinctive pathologies on the left pes, suggesting a common etiology or a cascading chain of causality. This should be investigated in-depth in the future.

Multiple sesamoids exhibit marginal osteolysis (Fig. 25), similar to that seen in the phalanges. A notable pathology on the medial surface on left lateral MC3 sesamoid of ETMNH 601 (Fig. 25) could be the result of numerous etiologies (pathological, traumatic, or even developmental) which cannot be differentiated prior to histologic or radiographic examination.

Population Patterns and Comparisons

Of the GFS *T. aepysoma* material recovered so far, the complete to near complete specimens represent adult males, with an older specimen (ETMNH 33000) and two younger middle-aged specimens (ETMNH 601 and ETMNH 609). Partial and fragmentary from juveniles and/or sub-adults has also been recovered (ETMNH 3721, ETMNH 5057, ETMNH ETMNH 32999). No definitively identified adult female material has been recovered thus far, though ETMNH 1901 has been suggested to be female by some workers and recent excavations have uncovered further juvenile material (ETMNH 32999, a nearly complete juvenile), further suggesting that females were present in the site area. Workers at other sites have suggested that male-biased deposits could represent bachelor herds (Mihlbachler 2003). Though, at GFS, the current male-bias could be a consequence of being a relatively recently developed site. Though, given GFS's status as an attritional site rather than a catastrophic site, which provide more

accurate snapshots of grouping behaviors (Voorhies 1969; Mihlbachler 2003), such hypotheses about population dynamics at GFS are tenuous at best. The GFS *T. aepysoma* sample carries primarily arthropathies with a handful of periodontal and traumatic pathologies. The majority of the arthropathies described here are in the early stage and likely didn't affect the animal significantly in life, with notable the exceptions of the ankylosed digit II of the left pes on ETMNH 601 and ETMNH 33000 proximal phalanx.

No traumatic pathologies similar to those of ETMNH 601 were observed among the AFB *T. major*, and what joints were able to be observed from the AFB sample were juvenile and young adult specimens, which lacked the periarticular arthroses noted among the mature GFS *T. aepysoma* in this study. Conversely, the GFS *T. aepysoma* sample compares favorably to a *T. hicksi* sample described in Stilson et al. (2016). All the *T. hicksi* material from Stilson et al. (2016) comes from the McKay Reservoir (MKR), 11 localities containing 3 geologic formations spanning from the Barstovian to the Hemphillian. This study considers the MKR *T. hicksi* material to be representative of a single sample, with the acknowledgement that the sample is not well constrained temporally. The MKR *T. hicksi* sample shows a similar distribution of periarticular arthropathies to the GFS *T. aepysoma*. Stilson et al. (2016) noted a lack of osteoarthritis and other arthropathies on the synovial joint surfaces in many fossil rhino taxa, and similarly so in other perissodactyls (Rothschild et al. 2001), with these studies finding periarticular erosion to be much more prevalent. This lack of articular surface pathology is not unexpected for open habitat taxa (Rothschild et al. 2001).

Cranial Texturing

Regarding the texturing of the nasals noted in the description, similar textures have been interpreted to indicate the presence of a small horn in other members of the genus (Thenius and

Hofer 1960; Prothero 2005), but comparable textures are also present on the dorsal orbital knobs of the frontals and the lateralmost extent of the intact right squamosal of ETMNH 601 (Fig. 3). If this texture were to be accepted to equate to the presence of a horn, then there would also be horns present above the orbits and on the zygomatic arch. In addition, this texture is much less pronounced than what is seen on rhinos known to have horns, such as *Coelodonta* or extant rhinos (Hieronymus 2009; Short et al. 2019). The rugose texturing present on the nasal of the GFS *T. aepysoma* is less consistent with that of known horned rhinos, which form distinct, ring-shaped (or annular) patterns of projecting rugosities (Hieronymus 2009; Hieronymus et al. 2009). The texture of the nasal rugosity in *T. aepysoma* (Fig. 3) is less distinct and more homogenous (an indicator of dermal armor according to Hieronymus 2009) than that of modern rhinos. Orbital knobs, and the squamosal portions of the zygomatic arches, also possess texturing similar to that of the nasals (Fig. 3), making it unlikely that the nasals bore a horn despite the robustness of the nasals (Wallace 2011; Short 2013; and Short et al. 2019). In fact, such rugosities on the squamosals in *Trigonias osbornii* and *Subhyracodon* are suggested to support dermal armor by Hieronymus (2009). Other ungulates with rugose cranial texturing not associated with horns include *Phacochoerus africanus* (warthog), entelodonts, and brontotheres. Therefore, the rugosities on the nasals, orbital knobs, and squamosals more likely bore dermal armor (as suggested in Wallace 2011) rather than horn. Earlier observation of *T. fossiger* by Matthew (1932) advocated for a similar interpretation in that species.

CHAPTER 5. CONCLUSION

- The GFS *T. aepysoma* do not appear to deviate from the broad patterns of pathology frequency or distribution observed in other fossil or modern rhinocerotids, with most pathologies found in the feet, as well as presence of dental/periodontal and rib pathologies.
- Rheumatoid arthritis appears to be present in most of the Gray Fossil Site *Teleoceras aepysoma*, given the abundance of periarticular defects and the comparative lack of defects on the articular facets.
- Pathologies on the mandibular tusks and ribs are likely the result of agonistic behavior that involved face-to-face confrontations using tusks and strikes to the flanks during chases, similar to what is seen in modern *Rhinoceros unicornis.*
- The presence of rugose texturing on the nasals alone should no longer be considered evidence enough to indicate that a rhinocerotid had a nasal horn. The type of rugosity, presence of rugosities elsewhere on the crania, and other aspects of morphology should be accounted for before asserting the presence of a horn. Especially as other lineages of ungulates with notable cranial rugosities, such as brontotheres, entelodonts, and even the modern warthog, are not reconstructed with horn associated with the rugosities.

Description of the pathologies present on GFS rhinos presented in this thesis is a step toward remedying the current paucity of published research on *Teleoceras* paleopathology.

Future Research

Better understanding of pathology and traumatic injury in modern taxa, especially wild samples, would help inform rhinocerotid paleopathology. The morphology of *Teleoceras* tarsals has been noted to be more similar to that of *Hippopotamus amphibias* than other rhinocerotids

(Schellhorn 2021). Therefore, investigation of tarsal, and potentially carpal, pathology in *Teleoceras* may benefit from comparisons to modern *Hippopotamus*, rather than rhinocerotids. Research on damage sustain by the tusks of male *R. unicornis*, as well as hippopotamid and suids, could provide useful comparisons to the marks noted on the tusks of ETMNH 33000 and their cause(s). Data on trauma instances in modern graviportal mammals inhabiting steep/mountainous terrain and/or areas of closed forests could provide relevant comparisons for interpretations of the hip and hind limb pathologies in ETMNH 601 and ETMNH 609, especially the presence or absence of traumas relating to the ligamentum teres. Research into the effects of herbivore diet and how it relates to periodontal pathology in modern mixed-feeders (switch-hitter browsers/grazers) could clarify whether the diet of the GFS *T. aepysoma* is the cause of the described periodontal lesions in ETMNH 601, ETMNH 21659, and ETMNH 33000. Further research into the effects of preferential chewing/mastication sidedness on the shape of the lambdoid crests in mammals, either due to behavioral preference or avoiding tooth/mouth sores, could be valuable for explaining the asymmetry of the *T. aepysoma* type specimens (ETMNH 601 and ETMNH 609).

Comparisons to *Teleoceras* from a broader range (geographic and temporal) of localities than in this study can help inform the observations made here. Special interest goes to *Teleoceras* at the FLMNH, as conversations with other researchers seem to indicate the FLMNH collections may have another population of *T. aepysoma* in the Palmetto Fauna (Short 2013). Current understanding suggests that Florida would have been a lowland savannah when the Palmetto Fauna was present. A much more typical habitat for *Teleoceras* than the karst highland closed forest environment suggested for GFS (Shunk et al. 2006; Ochoa et al. 2012; Short et al. 2019). Any differences in pathology distribution or frequency observed between the two localities

would lend further credence to the environment and topography of Early Pliocene Gray being responsible for some of the pathologies noted in the GFS *T. aepysoma*. Comparison to other species of *Teleoceras* may provide insight to whether the distinct morphology of *T. aepysoma* affects the distribution of pathology.

Additional material of *T. aepysoma* continues to be found every year at GFS. Future research on this new material will confirm or revise the interpretations/hypotheses in this study on the prevalence and nature of pathologies in the GFS *T. aepysoma* sample. Already, cursory inspection of preliminary prepared material not covered in this study from ETMNH 33000, the oldest individual recovered from the site thus far, shows promise for further research. Of note are similarities to tooth pathology seen in Pleistocene rhinos from Germany (Diedrich 2023), with dramatically worn anterior cheek teeth that have been reduced to indistinct pegs. Additionally, CT scans of larger elements at GFS, such as the mandible of ETMNH 21659, would provide more confidence for the interpretations made here.

REFERENCES

Arnett FC, Edworthy SM, Bloch DA, Mcshane DJ, Fries JF, Cooper NS, Healey LA, Kaplan SR, Liang MH, Luthra HS, et al. 1988. The American rheumatism association 1987 revised criteria for the classification of rheumatoid arthritis. Arthritis & Rheumatism. 31(3):315–324. doi:10.1002/art.1780310302.

Baker JR, Brothwell DR. 1980. Animal Diseases in Archaeology. London: Academic Press.

Bartosiewicz L. 2008. Description, diagnosis and the use of published data in animal palaeopathology: a case study using fractures. Veterinarija ir zootechnika. 41(63):12–24.

Böhmer C, Rössner GE. 2018. Dental paleopathology in fossil rhinoceroses: etiology and implications. Journal of Zoology. 304(1):3–12. doi:10.1111/jzo.12518.

Brooks RL. 1996. Standards for Data Collection from Human Skeletal Remains. Arkansas Archeological Survey Research Series No. 44. [accessed 2023 Oct 15]. https://www.jstor.org/stable/25669399?casa_token=V72dpudiBhoAAAAA:riMvQIawT5knZHUCfMYwA1Ssh1M6XLt-uS5nqDxLlP2MvoCnlOKMJcD10-TvZ0HUAj8o2_dYIeXwE3bfwm_X-XPaNF0eO3AErWHHRRaffFh_lknlINE.

Buikstra JE, Cook DC, Bolhofner KL. 2017. Introduction: Scientific rigor in paleopathology. International journal of paleopathology. 19:80–87.

Buikstra JE, Ubelaker DH. 1994. Standards for Data Collection from Human Skeletal Remains. Arkansas Archaeological Survey Press.:18.

Burt NM, Semple D, Waterhouse K, Lovell NC. 2013. Identification and interpretation of joint disease in paleopathology and forensic anthropology. Charles C Thomas Publisher. [accessed 2023 Oct 30]. https://books.google.com/books?hl=en&lr=&id=K-TCCAAAQBAJ&oi=fnd&pg=PR9&dq=Identification+and+interpretation+of+joint+dise

ase+in+paleopathology+and+forensic+anthropology&ots=nAY6Y17gH7&sig=wv5q2MNooVPO3H11XTWkJ-hSB98.

Byrd JW, Jones KS. 2004. Traumatic rupture of the ligamentum teres as a source of hip pain. Arthroscopy 2004;20(4):385–391.

Cerezal L, Kassarjian A, Canga A, Dobado MC, Montero JA, Llopis E, Rolón A, Pérez-Carro L. 2010. Anatomy, Biomechanics, Imaging, and Management of Ligamentum Teres Injuries. RadioGraphics. 30(6):1637–1651. doi:10.1148/rg.306105516.

Contreras PA, Paredes E, Wittwer F, Carrillo S. 2005. Clinical case: outbreak of white muscle disease or nutritional muscular dystrophy in calves. REVISTA CIENTIFICA-FACULTAD DE CIENCIAS VETERINARIAS. 15(5):401–405.

Cook DC. 2015. Paleopathology. In: Basics in human evolution. Elsevier. p. 427–437. [accessed 2023 Oct 23]. https://www.sciencedirect.com/science/article/pii/B9780128026526000311.

D'Amore DC, Blumensehine RJ. 2009. Komodo monitor (*Varanus komodoensis*) feeding behavior and dental function reflected through tooth marks on bone surfaces, and the application to ziphodont paleobiology. Paleobiology. 35(4):525–552.

DeSantis LR, Wallace SC. 2008. Neogene forests from the Appalachians of Tennessee, USA: geochemical evidence from fossil mammal teeth. Palaeogeography, Palaeoclimatology, Palaeoecology. 266(1–2):59–68.

Diedrich CG. 2008. A skeleton of an injured *Coelodonta antiquitatis* from the Late Pleistocene of north-western Germany. Cranium. 25(1):29–43.

Diedrich CG. 2023. Extinct Eurasian rhinoceros *Coelodonta* and *Stephanorhinus* dental pathologies and tooth change modus. Quaternary Science Reviews. 301:107922.

Dinerstein E. 2003. The Return of the Unicorns: The Natural History and Conservation of the Greater One-Horned Rhinoceros. In: The Return of the Unicorns. Columbia University Press. [accessed 2024 Feb 14]. https://www.degruyter.com/document/doi/10.7312/dine08450/html.

Drumheller-Horton SK. 2012. An actualistic and phylogenetic approach to identifying and interpreting crocodylian bite marks [dissertation]. University of Iowa. [accessed 2024 Mar 30]. https://iro.uiowa.edu/view/pdfCoverPage?instCode=01IOWA_INST&filePid=13730783730002771&download=true.

Drumheller SK, Brochu CA. 2014. A Diagnosis of *Alligator mississippiensis* Bite Marks with Comparisons to Existing Crocodylian Datasets. Ichnos. 21(2):131–146. doi:10.1080/10420940.2014.909353.

Drumheller SK, Wilberg EW, Sadleir RW. 2016. The utility of captive animals in actualistic research: A geometric morphometric exploration of the tooth row of *Alligator mississippiensis* suggesting ecophenotypic influences and functional constraints. Journal of Morphology. 277(7):866–878. doi:10.1002/jmor.20540.

Farlow JO, Sunderman JA, Havens JJ, Swinehart AL, Holman JA, Richards RL, Miller NG, Martin RA, Hunt RM, Storrs GW. 2001. The Pipe Creek Sinkhole biota, a diverse late Tertiary continental fossil assemblage from Grant County, Indiana. The American midland naturalist. 145(2):367–378.

Feger J, Yap J, Hacking C, Knipe H, Weerakkody Y. 2023. Bone erosion | Radiology Reference Article | Radiopaedia.org. Radiopaedia. doi:10.53347/rID-89819. [accessed 2023 Dec 7]. https://radiopaedia.org/articles/bone-erosion?lang=us.

Fitch HM, Fagan DA. 1982. Focal palatine erosion associated with dental malocclusion in captive cheetahs. Zoo Biology. 1(4):295–310. doi:10.1002/zoo.1430010403.

Fleming IA, Jonsson B, Gross MR, Lamberg A. 1996. An experimental study of the reproductive behaviour and success of farmed and wild Atlantic salmon (*Salmo salar*). Journal of Applied Ecology.:893–905.

Fowler ME, Mikota SK, editors. 2006. Biology, Medicine, and Surgery of Elephants. 1st ed. Wiley. [accessed 2023 May 2]. https://onlinelibrary.wiley.com/doi/book/10.1002/9780470344484.

Galateanu G, Hildebrandt TB, Maillot A, Etienne P, Potier R, Mulot B, Saragusty J, Hermes R. 2013. One small step for rhinos, one giant leap for wildlife management-imaging diagnosis of bone pathology in distal limb. PloS one. 8(7):e68493.

Garutt N. 1997. Traumatic skull damages in the woolly rhinoceros, *Coelodonta antiquitatis* Blumenbach, 1799. Cranium. 14(1):37–46.

Geiser F, Ferguson C. 2001. Intraspecific differences in behaviour and physiology: effects of captive breeding on patterns of torpor in feathertail gliders. Journal of Comparative Physiology B: Biochemical, Systemic, and Environmental Physiology. 171(7):569–576. doi:10.1007/s003600100207.

Gendy D, Marginal erosions in rheumatoid arthritis (illustration). Case study, Radiopaedia.org (Accessed on 06 Nov 2023) https://doi.org/10.53347/rID-75248

Gendy D, Salient features in different arthropathies (illustration). Case study, Radiopaedia.org (Accessed on 06 Nov 2023) https://doi.org/10.53347/rID-75325

Glover R. 1956. Weapons of the great Indian rhinoceros. Oryx. 3(4):197–197.

Griffin LR, Rawlinson JE, McDonald HG, Duncan C. 2016. Mandibular osteopathy in a Hagerman horse, *Equus simplicidens* (Equidae, Mammalia), from Hagerman Fossil Beds National Monument (Idaho, USA). International Journal of Paleopathology. 12:41–45.

Grogan EH, McDonnell SM. 2005. Injuries and blemishes in a semi-feral herd of ponies. Journal of Equine Veterinary Science. 25(1):26–30.

Groves CP. 1982. The skulls of Asian rhinoceroses: Wild and captive. Zoo Biol. 1(3):251–261. doi:10.1002/zoo.1430010309.

Guay P-J, Iwaniuk AN. 2008. Captive breeding reduces brain volume in waterfowl (Anseriformes). The Condor. 110(2):276–284.

Gustafson EP. 2012. New records of rhinoceroses from the Ringold Formation of central Washington and the Hemphillian-Blancan boundary. Journal of Vertebrate Paleontology. 32(3):727–731. doi:10.1080/02724634.2012.658481.

Hanna RR. 2002. Multiple injury and infection in a sub-adult theropod dinosaur *Allosaurus fragilis* with comparisons to allosaur pathology in the Cleveland-Lloyd Dinosaur Quarry Collection. Journal of Vertebrate Paleontology. 22(1):76–90. doi:10.1671/0272-4634(2002)022[0076:MIAIIA]2.0.CO;2.

Hard JJ, Berejikian BA, Tezak EP, Schroder SL, Knudsen CM, Parker LT. 2000. Evidence for Morphometric Differentiation of Wild and Captively Reared Adult Coho Salmon: A Geometric Analysis. Environmental Biology of Fishes. 58(1):61–73. doi:10.1023/A:1007646332666.

Harrison JA, Manning EM. 1983. Extreme carpal variability in *Teleoceras* (Rhinocerotidae, Mammalia). Journal of Vertebrate Paleontology. 3(1):58–64. doi:10.1080/02724634.1983.10011959.

Haugrud SJ, Compton BP. 2008. Reversible filler: a fresh look at Butvar-76. Journal of Vertebrate Paleontology. 28(suppl 3):89A.

Haynes G. 1983. A guide for differentiating mammalian carnivore taxa responsible for gnaw damage to herbivore limb bones. Paleobiology. 9(2):164–172.

Hazarika BC, Saikia PK. 2010. A study on the behaviour of Great Indian One-horned Rhino (*Rhinoceros unicornis* Linn.) in the Rajiv Gandhi Orang National Park, Assam, India. NeBIO. 1(2):62–74.

Hieronymus TL. 2009. Osteological correlates of cephalic skin structures in Amniota: documenting the evolution of display and feeding structures with fossil data. Ohio University. [accessed 2023 Oct 15]. https://search.proquest.com/openview/52e21ca717d87d8fe346aaeabf127529/1?pq-origsite=gscholar&cbl=18750&casa_token=gN8GIGBnxa8AAAAA:q7pObEMsPAG6n9e3W2TCwwXFqsrDtbmgmRAgEliuBjnkywnQYuep_UWDqhNzCzI2OYuni146bA.

Hieronymus TL, Witmer LM, Tanke DH, Currie PJ. 2009. The Facial Integument of Centrosaurine Ceratopsids: Morphological and Histological Correlates of Novel Skin Structures. The Anatomical Record. 292(9):1370–1396. doi:10.1002/ar.20985.

Hitchins PM. 1978. Age determination of the black rhinoceros (*Diceros bicornis* Linn.) in Zululand. South African Journal of Wildlife Research-24-month delayed open access. 8(2):71–80.

Hoefs M, Bunch TD. 2001. Lumpy jaw in wild sheep and its evolutionary implications. Journal of Wildlife Diseases. 37(1):39–48.

Holmes M, Thomas R, Hamerow H. 2021. Periodontal disease in sheep and cattle: Understanding dental health in past animal populations. International Journal of Paleopathology. 33:43–54.

Howell AB. 1925. Asymmetry in the skulls of mammals. Proceedings of the United States National Museum. [accessed 2023 Oct 15]. https://repository.si.edu/bitstream/handle/10088/15391/USNMP-67_2599_1925.pdf.

Hullot M, Antoine P-O. 2022. Enamel hypoplasia on rhinocerotoid teeth: Does CT-scan imaging detect the defects better than the naked eye? Palaeovertebrata. 45(1):e2.

Janeczek M, Chrószcz A, Onar V, Henklewski R, Skalec A. 2017. Proximal interphalangeal joint ankylosis in an early medieval horse from Wroc\law Cathedral Island, Poland. International journal of paleopathology. 17:18–25.

Kargopoulos N, Rabe C, Gilissen E, Coudyzer W, Chinsamy A. 2023 preprint. Multiple Cranial Pathologies in the Spotted Hyaenas, *Crocuta Crocuta*. [accessed 2024 Feb 29]. https://papers.ssrn.com/sol3/papers.cfm?abstract_id=4623780.

Kerley ER, Bass WM. 1967. Paleopathology: Meeting Ground for Many Disciplines. Science. 157(3789):638–644. doi:10.1126/science.157.3789.638.

Knubben JM, Fürst A, Gygax L, Stauffacher M. 2008. Bite and kick injuries in horses: Prevalence, risk factors and prevention. Equine Veterinary Journal. 40(3):219–223. doi:10.2746/042516408X253118.

Laurie, W. A. 1978. The ecology of the greater one-horned rhinoceros. Ph.D. diss., Cambridge University

Lawler DF. 2017. Differential diagnosis in paleopathology. International Journal of Paleopathology. 19(2017):119–123.

Leader-Williams N. 1980. Dental abnormalities and mandibular swellings in South Georgia reindeer. Journal of Comparative Pathology. 90(2):315–330.

LeMay M. 1977. Asymmetries of the skull and handedness: Phrenology revisited. Journal of the neurological sciences. 32(2):243–253.

Lovell NC. 1997. Trauma analysis in paleopathology. American J Phys Anthropol. 104(S25):139–170. doi:10.1002/(SICI)1096-8644(1997)25+<139::AID-AJPA6>3.0.CO;2-#.

Luikart KA, Stover SM. 2005. Chronic sole ulcerations associated with degenerative bone disease in two Asian elephants (*Elephas maximus*). Journal of Zoo and Wildlife Medicine. 36(4):684–688.

Madden CT, Dalquest WW. 1990. The last rhinoceros in North America. Journal of Vertebrate Paleontology. 10(2):266–267. doi:10.1080/02724634.1990.10011812.

Marean CW, Spencer LM. 1991. Impact of carnivore ravaging on zooarchaeological measures of element abundance. American Antiquity. 56(4):645–658.

Mariotti A. 2007. Dental Caries. In: Enna SJ, Bylund DB, editors. xPharm: The Comprehensive Pharmacology Reference. Elsevier. p. 1–4. https://doi.org/10.1016/B978-008055232-3.60698-1.

Martin RA. 2010. The North American *Promimomys* immigration event. Paludicola. 8(1):14–21.

Matthew WD. 1932. A review of the rhinoceroses with description of *Aphelops* material from the Pliocene of Texas. University of California Publications Bulletin of the Department of Geological Sciences. 20:435–437.

MacFadden BJ. 1998. Tale of two rhinos: isotopic ecology, paleodiet, and niche differentiation of *Aphelops* and *Teleoceras* from the Florida Neogene. Paleobiology. 24(2):274–286.

McPhee ME. 2004a. Generations in captivity increases behavioral variance: considerations for captive breeding and reintroduction programs. Biological conservation. 115(1):71–77.

McPhee ME. 2004b. Morphological change in wild and captive oldfield mice *Peromyscus polionotus subgriseus*. Journal of Mammalogy. 85(6):1130–1137.

Mead AJ. 1999. Enamel hypoplasia in Miocene rhinoceroses (*Teleoceras*) from Nebraska: evidence of severe physiological stress. Journal of Vertebrate Paleontology. 19(2):391–397. doi:10.1080/02724634.1999.10011150.

Mead AJ. 2000. Sexual dimorphism and paleoecology in *Teleoceras*, a North American Miocene rhinoceros. Paleobiology. 26(4):689–706.

Mihlbachler MC. 2001. Was *Teleoceras* a semi-aquatic hippo ecomorph? Journal of Vertebrate Paleontology. 22:80A.

Mihlbachler MC. 2003. Demography of late Miocene rhinoceroses (*Teleoceras proterum* and *Aphelops malacorhinus*) from Florida: linking mortality and sociality in fossil assemblages. Paleobiology. 29(3):412–428.

Mihlbachler MC. 2007. Sexual Dimorphism and Mortality Bias in a Small Miocene North American Rhino, *Menoceras arikarense*: Insights into the Coevolution of Sexual Dimorphism and Sociality in Rhinos. J Mammal Evol. 14(4):217–238. doi:10.1007/s10914-007-9048-4.

Moodie RL. 1922. Actinomycosis in a fossil rhinoceros. The Journal of Parasitology. 9(1):28–28.

Moodie RL. 1923. Paleopathology: an introduction to the study of ancient evidences of disease. University of Illinois Press. [accessed 2023 Oct 15]. https://books.google.com/books?hl=en&lr=&id=5Q_Vz9yV-

8EC&oi=fnd&pg=PA3&dq=Paleopathology-+an+Introduction+to+the+Study+of+Ancient+Evidences+of+Disease&ots=12ZyKqLx63&sig=rbL_icfFvtbRs8BMTdaxQsFd-es.

Munson L, Terio KA, Worley M, Jago M, Bagot-Smith A, Marker L. 2005. Extrinsic factors significantly affect patterns of disease in free-ranging and captive cheetah (Acinonyx jubatus) populations. Journal of wildlife diseases. 41(3):542–548.

Njau JK, Blumenschine RJ. 2006. A diagnosis of crocodile feeding traces on larger mammal bone, with fossil examples from the Plio-Pleistocene Olduvai Basin, Tanzania. Journal of Human Evolution. 50(2):142–162.

O'Regan HJ, Kitchener AC. 2005. The effects of captivity on the morphology of captive, domesticated and feral mammals. [accessed 2024 Mar 30]. https://www.cabidigitallibrary.org/doi/full/10.5555/20063002090.

Ochoa D, Whitelaw M, Liu Y-SC, Zavada M. 2012. Palynology of Neogene sediments at the Gray Fossil Site, Tennessee, USA: floristic implications. Review of Palaeobotany and Palynology. 184:36–48.

Osborn HF. 1898. A Complete Skeleton of *Teleoceras* the True Rhinoceros from the Upper Miocene of Kansas. Science. 7(173):554–557. doi:10.1126/science.7.173.554.

Panagiotopoulou O, Pataky TC, Hutchinson JR. 2019. Foot pressure distribution in White Rhinoceroses (*Ceratotherium simum*) during walking. PeerJ. 7:e6881.

Pickering TR, Wallis J. 1997. Bone modifications resulting from captive chimpanzee mastication: implications for the interpretation of Pliocene archaeological faunas. Journal of Archaeological Science. 24(12):1115–1127.

Pimiento C, Benton MJ. 2020. The impact of the Pull of the Recent on extant elasmobranchs. Cavin L, editor. Palaeontology. 63(3):369–374. doi:10.1111/pala.12478.

Prothero DR. 1998. Rhinocerotidae. In: Evolution of tertiary mammals of North America. p. 595. [accessed 2023 Oct 23]. https://doc.rero.ch/record/13709/files/PAL_E444.pdf.

Prothero DR. 2005. The evolution of North American rhinoceroses. Cambridge University Press. [accessed 2023 Oct 23]. https://books.google.com/books?hl=en&lr=&id=yXhHCt8Ml7YC&oi=fnd&pg=PA4&dq=The+Evolution+of+North+American+Rhinoceroses&ots=3k9pGyVVt4&sig=eiotVqCwlmgqkk3CYrFiQk6PRGs.

Prothero DR, Schoch RM. 1989. Origin and Evolution of the Perissodactyla: Summary and Synthesis. In: The Evolution of Perissodactyls. New York: Oxford University Press. p. 504–537.

Radeke-Auer K, Clauss M, Stagegaard J, Bruins-Van Sonsbeek LG, Lopez J. 2023. Retrospective pathology review of captive black rhinoceros Diceros bicornis in the EAZA Ex-situ Programme (1995-2022). Journal of Zoo and Aquarium Research. 11(2):298–310.

Redfern R, Roberts CA. 2019. Chapter 9 – Trauma. In: Buikstra JE, editor. Ortner's Identification of Pathological Conditions in Human Skeletal Remains. 3rd ed. Academic Press. p. 211–284. https://doi.org/10.1016/B978-0-12-809738-0.00009-0.

Regnault S, Hermes R, Hildebrandt T, Hutchinson J, Weller R. 2013. Osteopathology in the feet of rhinoceroses: lesion type and distribution. Journal of Zoo and Wildlife Medicine. 44(4):918–927.

Regnault S, Dixon JJ, Warren-Smith C, Hutchinson JR, Weller R. 2017. Skeletal pathology and variable anatomy in elephant feet assessed using computed tomography. PeerJ. 5:e2877.

Robinson PT. 1979. A literature review of dental pathology and aging by dental means in nondomestic animals: part II. The Journal of Zoo Animal Medicine. 10(3):81–91.

Rothschild BM. 2002. Contributions of paleorheumatology to understanding contemporary disease. Reumatismo. 54(3):272–284.

Rothschild B. 2016. Alar and transverse ligament calcification and crown dens. The Journal of Rheumatology. 43(6):1251–1251.

Rothschild BM, Martin LD. 2006. Skeletal impact of disease: bulletin 33. New Mexico Museum of Natural History and Science. [accessed 2023 Oct 23]. https://books.google.com/books?hl=en&lr=&id=AGfmCQAAQBAJ&oi=fnd&pg=PA1&dq=Skeletal+Impact+of+Disease&ots=8lDyflmbee&sig=GwiYtWcxPdBRugcGwosldrQLdh4.

Rothschild BM, Prothero DR., Rothschild C. 2001. Origins of spondyloarthropathy in Perissodactyla. In: Clinical and experimental rheumatology: an international journal of rheumatic and connective tissue diseases. Vol. 19. p. 628. [accessed 2023 Nov 15]. https://doc.rero.ch/record/13723/files/PAL_E461.pdf.

Rothschild BM, Tanke DH. 1992. Paleoscene 13. Paleopathology of vertebrates: insights to lifestyle and health in the geological record. Geoscience Canada. [accessed 2023 Oct 23]. https://journals.lib.unb.ca/index.php/GC/article/view/3763.

Rowe P, Koller A, Sharma S. 2018. Physiology, bone remodeling. [accessed 2023 Oct 23]. https://europepmc.org/books/nbk499863.

Sahney S, Benton MJ. 2017. The impact of the Pull of the Recent on the fossil record of tetrapods. Evolutionary Ecology Research. 18(1):7–23.

Samuels JX, Bredehoeft KE, Wallace SC. 2018. A new species of *Gulo* from the Early Pliocene Gray Fossil Site (Eastern United States); rethinking the evolution of wolverines. PeerJ. 6:e4648.

Samuels JX, Schap J. Early Pliocene Leporids from the Gray Fossil Site of Tennessee. [accessed 2024 Mar 29]. https://eaglehill.us/epal-pdfs-regular/EPAL-008-Samuels.pdf.

Sazelová S, Lawler D, Hladilová Š, Boriová S, Šáliová S, Janoušek T, Perri A, Hublin J-J, Svoboda J. 2020. A wolf from Gravettian site Pavlov I, Czech Republic: Approach to skull pathology. International Journal of Paleopathology. 31:7–13.

Schachner ER, Hutchinson JR, Farmer CG. 2013. Pulmonary anatomy in the Nile crocodile and the evolution of unidirectional airflow in Archosauria. PeerJ. 1:e60.

Schett G, Gravallese E. 2012. Bone osteolysis in rheumatoid arthritis: mechanisms, diagnosis and treatment. Nature Reviews Rheumatology. 8(11):656–664.

Schellhorn R. 2021. Stiffening in the carpus of Prosantorhinus germanicus (Perissodactyla, Rhinocerotidae) from Sandelzhausen (Germany). PalZ. 95(3):531–536. doi:10.1007/s12542-021-00574-7.

Short RA. 2013. A new species of *Teleoceras* from the Late Miocene Gray Fossil Site, with comparisons to other North American Hemphillian species [Masters Thesis]. East Tennessee State University. [accessed 2023 Oct 23]. https://search.proquest.com/openview/616f2d23af98b3c7e56cce68ab5dbbee/1?pq-origsite=gscholar&cbl=18750.

Short RA, Wallace SC, Emmert LG. 2019. A New Species of *Teleoceras* (Mammalia, Rhinocerotidae) from the Late Hemphillian of Tennessee. Bulletin of the Florida Museum of Natural History. 56(5):183–260.

Shunk AJ, Driese SG, Clark GM. 2006. Latest Miocene to earliest Pliocene sedimentation and climate record derived from paleosinkhole fill deposits, Gray Fossil Site, northeastern Tennessee, USA. Palaeogeography, Palaeoclimatology, Palaeoecology. 231(3–4):265–278.

Silberman MS, Fulton RB. 1979. Medical problems of captive and wild rhinoceros: A review of the literature and personal experiences. The Journal of Zoo Animal Medicine. 10(1):6–16.

Stecher RM. 1958. Ankylosis of the finger joints in rheumatoid arthritis. Annals of the Rheumatic Diseases. 17(4):365.

Stecher RM, Schultz CB, Tanner LG. 1962. A Middle Miocene Rhinoceros Quarry in Morrill County, Nebraska (with Notes on Hip Disease in Diceratherium). [accessed 2024 Mar 26]. https://digitalcommons.unl.edu/museumbulletin/11/.

Stefaniak K, Kotowski A, Badura J, Sobczyk A, Borówka RK, Stachowicz-Rybka R, Moskal-del Hoyo M, Hrynowiecka A, Tomkowiak J, Sławińska J. 2023. A skeleton of peat-trapped forest rhinoceros Stephanorhinus kirchbergensis (Jäger, 1839) from Gorzów Wielkopolski, Northwestern Poland: a record of life and death of the Eemian large mammals. [accessed 2024 Mar 26]. https://digital.csic.es/handle/10261/310727.

Stevanović O, Janeczek M, Chrószcz A, Marković N. 2015. Joint Diseases in Animal Paleopathology: Veterinary Approach. Macedonian Veterinary Review. 38(1):5–12. doi:10.14432/j.macvetrev.2014.10.024.

Stilson KT, Hopkins SSB, Davis EB. 2016. Osteopathology in Rhinocerotidae from 50 Million Years to the Present. PLoS ONE. 11(2):e0146221.

Tan AL, Tanner SF, Conaghan PG, Radjenovic A, O'Connor P, Brown AK, Emery P, McGonagle D. 2003. Role of metacarpophalangeal joint anatomic factors in the distribution of synovitis and bone erosion in early rheumatoid arthritis. Arthritis & Rheumatism. 48(5):1214–1222. doi:10.1002/art.10963.

Teleoceras aepysoma, Gray Fossil Site, TN. https://sketchfab.com/3d-models/teleoceras-aepysoma-gray-fossil-site-tn-f3f73d673abf4680a6ca21e339bba95a.

Thompson KG. 2015. Bones and joints. In: Craig LE, Dittmer KE, editors. Jubb, Kennedy & Palmer's pathology of domestic animals. Vol. 1. Elsevier Inc. St Louis, MO, USA. p. 16–163. [accessed 2023 Oct 30]. https://books.google.com/books?hl=en&lr=&id=X7RgCgAAQBAJ&oi=fnd&pg=PA16&dq=bones+and+joints+keith+thompson&ots=7UZh8VQtCX&sig=GkTKoP--lZDeyDtI_wA3C5-1TnU.

Tucker ST, Otto RE, Joeckel RM, Voorhies MR. 2014. The geology and paleontology of Ashfall Fossil Beds, a late Miocene (Clarendonian) mass-death assemblage, Antelope County and adjacent Knox County, Nebraska, USA. [accessed 2023 Oct 23]. https://pubs.geoscienceworld.org/gsa/books/book/889/chapter/4643607/The-geology-and-paleontology-of-Ashfall-Fossil.

Van Kolfschoten T, Parfitt SA, Serangeli J, Bello SM. 2015. Lower Paleolithic bone tools from the 'spear horizon'at Schöningen (Germany). Journal of Human Evolution. 89:226–263.

Von Houwald F. 2016. Causes and prevention of foot problems in Greater one-horned rhinoceros *Rhinoceros unicornis* in zoological institutions. International Zoo Yearbook. 50(1):215–224. doi:10.1111/izy.12116.

Voorhies MR. 1969. Taphonomy and population dynamics of an early Pliocene vertebrate fauna, Knox County, Nebraska. University of Wyoming. [accessed 2024 Jan 23]. https://pubs.geoscienceworld.org/uwyo/books/book/957/Taphonomy-and-Population-Dynamics-of-an-Early.

Voorhies MR, Thomasson JR. 1979. Fossil Grass Anthoecia Within Miocene Rhinoceros Skeletons: Diet in an Extinct Species. Science. 206(4416):331–333. doi:10.1126/science.206.4416.331.

Waldron T. 2020. Palaeopathology. Cambridge University Press. [accessed 2023 Oct 23]. https://books.google.com/books?hl=en&lr=&id=5BEMEAAAQBAJ&oi=fnd&pg=PR11&dq=Waldron+T.+2009.+Paleopathology&ots=ZOmCO1KEj1&sig=MBPSYyA2UKmDMexcSGc71-WX5VE.

Walker BR, Colledge NR. 2013. Davidson's principles and practice of medicine e-book. Elsevier Health Sciences. [accessed 2023 Nov 8]. https://books.google.com/books?hl=en&lr=&id=W-5kAgAAQBAJ&oi=fnd&pg=PP1&dq=Davidson%27s+principles+and+practice+of+medicine+&ots=dO1mzwtTZR&sig=MnBLwswHWOMuVZXSQekqYVeeJYk.

Wallace SC. 2011. The short-legged rhinoceros, *Teleoceras*. In: Schubert BW, Mead JI, editors. Gray Fossil Site: 10 Years of Research. Johnson City, TN: Don Sundquist Center of Excellence in Paleontology, East Tennessee State University. p. 75–77.

Wang B, Secord R. 2020. Paleoecology of *Aphelops* and *Teleoceras* (Rhinocerotidae) through an interval of changing climate and vegetation in the Neogene of the Great Plains, central United States. Palaeogeography, Palaeoclimatology, Palaeoecology. 542:109411.

Webb SD. 1969. The Burge and Minnechaduza Clarendonian Mammalian Faunas of North-central Nebraska. University of California Publications in the Geological Sciences. 78:1-191.

Weiss RJ, Wretenberg P, Stark A, Palmblad K, Larsson P, Gröndal L, Broström E. 2008. Gait pattern in rheumatoid arthritis. Gait & posture. 28(2):229–234.

West G. 2006. Musculoskeletal System. In: Fowler ME, Mikota SK, editors. Biology, Medicine, and Surgery of Elephants. 1st ed. Blackwell Publishing. p. 263–270.

Wilczak CA, Jones EB. 2011. Osteoware^{TM} Software Manual: Volume II Pathology Module. Washington, D.C.: Smithsonian Institution.

Willey P, Snyder LM. 1989. Canid modification of human remains: implications for time-since-death estimations. Journal of Forensic Sciences. 34(4):894–901.

Womack TM, Crampton JS, Hannah MJ. 2020. The Pull of the Recent revisited: negligible species-level effect in a regional marine fossil record. Paleobiology. 46(4):470–477.

Yu SM, Yu JS. 2015. Calcaneal avulsion fractures: an often forgotten diagnosis. American Journal of Roentgenology. 205(5):1061–1067.

Zuccarelli MD. 2004. Comparative morphometric analysis of captive vs. wild African lion (Panthera leo) skulls. Bios.:131–138.

APPENDIX: List of Specimens

Table 1 List of specimens

Specimen No.	Species	Locality	Material	Comments
ETMNH 502	*T. aepysoma*	GFS	Partial right ulna	
ETMNH 559	*T. aepysoma*	GFS	Isolated caudal vertebra	
ETMNH 564	*T. aepysoma*	GFS	Isolated partial manual medial phalanx	
ETMNH 573	*T. aepysoma*	GFS	Isolated caudal vertebra	
ETMNH 601	*T. aepysoma*	GFS	Complete skeleton	Paratype, male
ETMNH 609	*T. aepysoma*	GFS	Complete skeleton	Holotype, male
ETMNH 743	*T. aepysoma*	GFS	Isolated partial manual distal phalanx	
ETMNH 769	*T. aepysoma*	GFS	Isolated partial manual proximal phalanx	
ETMNH 1901	*T. aepysoma*	GFS	Isolated left astragalus	Female?
ETMNH 1902	*T. aepysoma*	GFS	Complete left tibia with fibula fragments	
ETMNH 3721	*T. aepysoma*	GFS	Partial left femur	Sub-adult
ETMNH 3747	*T. aepysoma*	GFS	Rib and bone fragments	
ETMNH 3749	*T. aepysoma*	GFS	Isolated right mesocuneiform	
ETMNH 3752	*T. aepysoma*	GFS	Partial thoracic vertebra, proximal rib fragment, and pedal sesamoid	
ETMNH 3754	*T. aepysoma*	GFS	5 partial ribs with additional fragments	
ETMNH 3755	*T. aepysoma*	GFS	Isolated left manual digit IV proximal phalanx	
ETMNH 4286	*T. aepysoma*	GFS	Rib fragments	
ETMNH 4381	*T. aepysoma*	GFS	Manual digit III phalangeal sesamoid	
ETMNH 5057	*T. aepysoma*	GFS	Left humerus proximal epiphysis	Sub-adult
ETMNH 5233	*T. aepysoma*	GFS	Isolate partial manual distal phalanx	

ETMNH 6037	*T. aepysoma*	GFS	Proximal rib fragments	
ETMNH 6648	*T. aepysoma*	GFS	Partial right humerus	
ETMNH 6649	*T. aepysoma*	GFS	Rib fragment	
ETMNH 7291	*T. aepysoma*	GFS	Proximal rib fragment	
ETMNH 7294	*T. aepysoma*	GFS	Rib fragment	
ETMNH 8271	*T. aepysoma*	GFS	Fragmentary dentary, vertebra spine fragments, rib fragments, sternebra, partial right wrist and manus, distal right tibia and fibula fragments	
ETMNH 8516	*T. aepysoma*	GFS	Isolated left magnum	
ETMNH 8762	*T. aepysoma*	GFS	Isolate left ulna fragment	
ETMNH 10959	*T. aepysoma*	GFS	Rib fragment	
ETMNH 12175	*T. aepysoma*	GFS	Partial nasal and partial thoracic vertebra	
ETMNH 12242	*T. aepysoma*	GFS	Rib fragment	
ETMNH 12450	*T. aepysoma*	GFS	Isolated proximal pedal phalanx	
ETMNH 12776	*T. aepysoma*	GFS	Isolated manual digit III phalangeal sesamoid	
ETMNH 12777	*T. aepysoma*	GFS	Isolated manual digit III phalangeal sesamoid	
ETMNH 13236	*T. aepysoma*	GFS	Isolated trapezium	
ETMNH 13914	*T. aepysoma*	GFS	Isolate right maxilla fragment	
ETMNH 13968	*T. aepysoma*	GFS	Manual phalangeal sesamoid	
ETMNH 14174	*T. aepysoma*	GFS	Isolated rib fragment	
ETMNH 14175	*T. aepysoma*	GFS	Isolated right astragalus	
ETMNH 14710	*T. aepysoma*	GFS	Isolated rib	
ETMNH 14894	*T. aepysoma*	GFS	Isolated rib fragment	
ETMNH 17351	*T. aepysoma*	GFS	Isolate mandible fragment	
ETMNH 17352	*T. aepysoma*	GFS	Isolate mandible fragment	
ETMNH 17353	*T. aepysoma*	GFS	Isolate coronoid process	

ETMNH 17355	*T. aepysoma*	GFS	Isolated proximal rib fragment	
ETMNH 17356	*T. aepysoma*	GFS	Isolated proximal rib fragment	
ETMNH 17357	*T. aepysoma*	GFS	Isolated manual digit IV proximal phalanx	
ETMNH 19280	*T. aepysoma*	GFS	Partial mandible, partial manubrium, rib fragments, distal manual phalanx, proximal tibia and fibula fragment, and left mesocuneiform	Associated with former UTK material: partial humerus (UTK 1.01, 1.02, & 1.03), partial left cuneiform (UTK 1.06)
ETMNH 20412	*T. aepysoma*	GFS	Partial isolated left 4th metacarpal	
ETMNH 20419	*T. aepysoma*	GFS	Isolated rib fragment	
ETMNH 20424	*T. aepysoma*	GFS	Isolated partial left rib	
ETMNH 20825	*T. aepysoma*	GFS	Isolated manual phalangeal sesamoid	
ETMNH 21073	*T. aepysoma*	GFS	Isolated left astragalus	
ETMNH 21296	*T. aepysoma*	GFS	Isolated left unciform	
ETMNH 21297	*T. aepysoma*	GFS	Isolated rib fragment	
ETMNH 21299	*T. aepysoma*	GFS	Isolated rib fragments	
ETMNH 21302	*T. aepysoma*	GFS	Isolated manual sesamoid	
ETMNH 21659	*T. aepysoma*	GFS	Partial mandible and partial proximal rib	
ETMNH 27500	*T. aepysoma*	GFS	Isolated rib fragment	
ETMNH 27777	*T. aepysoma*	GFS	Isolated rib fragment	
ETMNH 28178	*T. aepysoma*	GFS	Rib fragments and left magnum	
ETMNH 28800	*T. aepysoma*	GFS	Isolated proximal left tibia fragment	
ETMNH 29000	*T. aepysoma*	GFS	Ventral scapula fragment	
ETMNH 31001	*T. aepysoma*	GFS	Isolated manual sesamoid	
ETMNH 32999	*T. aepysoma*	GFS	Left scaphoid, both 2nd and 3rd metacarpals, left	Juvenile female, with additional

ETMNH 32999 cont.			digit II proximal phalanx, left digit III medial phalanx, partial right distal phalanges (digit II, III, & IV), and both right 3rd metacarpal sesamoids	material being prepped
ETMNH 33000	*T. aepysoma*	GFS	Complete crania, partial mandible, and partial postcranial skeleton	Older male (heavily worn cheek teeth), with some material still being prepped
ETMNH 37998	*T. aepysoma*	GFS	Left 2nd and 4th metatarsals	
ETMNH 38065	*T. aepysoma*	GFS	Isolated pedal digit III distal phalanx	Juvenile
ETMNH-Z 7216	*R. unicornis*	BZ	Complete skeleton	Captive adult male, with damages from necropsy
UNSM 27801	*T. major*	AFB	Complete skeleton	Juvenile
UNSM 27802	*T. major*	AFB	Complete skeleton	Adult female
UNSM 27803	*T. major*	AFB	Complete skeleton	Adult male
UNSM 27805	*T. major*	AFB		Adult male
UNSM 27806	*T. major*	AFB		Female
UNSM 27807	*T. major*	AFB		
UNSM 27808	*T. major*	AFB		Adult female
UNSM 27817	*T. major*	AFB		Juvenile
UNSM 51101	*T. major*	AFB		Juvenile
UNSM 52218	*T. major*	AFB		Adult female
UNSM 52222	*T. major*	AFB	Complete skeleton	Sub-adult
UNSM 52223	*T. major*	AFB	Complete skeleton	Adult female
UNSM 52227	*T. major*	AFB	Complete skeleton	Juvenile
UNSM 52228	*T. major*	AFB	Nearly complete skeleton (missing pelvis)	Adult female
UNSM 52229	*T. major*	AFB		Juvenile
UNSM 52230	*T. major*	AFB		Juvenile
UNSM 52232	*T. major*	AFB	Complete skeleton	Juvenile/sub-adult female

UNSM 52233	*T. major*	AFB		Juvenile
UNSM 52234	*T. major*	AFB	Complete skeleton	Adult female
UNSM 52235	*T. major*	AFB		Adult
UNSM 52236	*T. major*	AFB	Complete skeleton	Adult male
UNSM 52237	*T. major*	AFB	Complete skeleton	Adult female
UNSM 52238	*T. major*	AFB	Complete skeleton	Adult female
UNSM 52239	*T. major*	AFB		Adult male
UNSM 52242	*T. major*	AFB	Complete skeleton	Sub-adult female
UNSM 52246	*T. major*	AFB	Complete skeleton	Adult female
UNSM 52269	*T. major*	AFB	Complete skeleton	Adult female
UNSM 52271	*T. major*	AFB		Adult female
UNSM 52272	*T. major*	AFB	Complete skeleton	Adult male
UNSM 52273	*T. major*	AFB		Adult
USNM 52274	*T. major*	AFB		
UNSM 52275	*T. major*	AFB		Sub-adult
UNSM 52282	*T. major*	AFB	Complete skeleton	Adult female
UNSM 52283	*T. major*	AFB	Complete skeleton	Adult female
UNSM 52284	*T. major*	AFB		Sub-adult
UNSM 52286	*T. major*	AFB		Adult female
UNSM 52287	*T. major*	AFB	Complete skeleton	Sub-adult female
USNM 52288	*T. major*	AFB		Adult male
UNSM 52294	*T. major*	AFB	Anterior half of skeleton	Adult male
UNSM 52373	*T. major*	AFB		Adult female
UTK 1.01	*T. aepysoma*	GFS	Proximal humerus epiphysis	Associated with ETMNH 19280
UTK 1.02	*T. aepysoma*	GFS	Proximal humerus diaphysis	Associated with ETMNH 19280
UTK 1.03	*T. aepysoma*	GFS	Distal humerus epiphysis	Associated with ETMNH 19280
UTK 1.06	*T. aepysoma*	GFS	Partial left cuneiform	Associated with ETMNH 19280
UTK 2.02	*T. aepysoma*	GFS	Proximal manual phalanx	

UTK 2.03	*T. aepysoma*	GFS	Pedal digit III distal phalanx	
UTK 4	*T. aepysoma*	GFS	Unciform	
UTK 4.01	*T. aepysoma*	GFS	Right magnum	
UTK 5	*T. aepysoma*	GFS	Left cuneiform	
UTK 6	*T. aepysoma*	GFS	Left lunar	
UTK 8.01	*T. aepysoma*	GFS	Partial radius	
UTK 8.02	*T. aepysoma*	GFS	Left proximal ulna fragment	
UTK 10	*T. aepysoma*	GFS	Left magnum	
UTK 14.xx	*T. aepysoma*	GFS	Proximal manual phalanx	
UTK 15.xx	*T. aepysoma*	GFS	Left manual digit III proximal phalanx	

Abbreviations: ETMNH = East Tennessee State University Museum of Natural History, GFS = Gray Fossil Site, ETMNH-Z = East Tennessee State University Museum of Natural History Zoological collection, BZ = Buffalo Zoo, UTK = University of Tennessee Knoxville

VITA

THOMAS W. SCAIFE

Education:	M.S. Geoscience, East Tennessee State University, Johnson City, Tennessee, 2024
	B.S. Geology, University of Tennessee at Chattanooga, Chattanooga, Tennessee, 2021
	Clarksville High School, Clarksville, Tennessee
Professional Experience:	Graduate Assistant, East Tennessee State University, College of Arts and Sciences, 2022-2023
Publications:	Timothy Gaudin, Thomas Scaife, Nestor Toledo and Gerardo De Iuliis (2023): Cranial osteology of the basal megatherioid sloth *Schismotherium* (Mammalia, Xenarthra) and its taxonomic implications, Historical Biology, DOI: 10.1080/08912963.2022.2162399
	Timothy J. Gaudin, and Thomas Scaife (2022). Cranial osteology of a juvenile specimen of *Acratocnus ye* (Mammalia, Xenarthra) and its ontogenetic and phylogenetic implications, The Anatomical Record, DOI: 10.1002/ar.25062
Honors and Awards:	Outstanding Research within the Department of Biology, Geology, and Environmental Science, University of Tennessee at Chattanooga, 2020